Title	Study on Discrete Current Fluctuation in Carbon Nanotube/Redox Active Molecule Hybrid Device
Author(s)	Setiadi, Agung
Citation	大阪大学, 2017, 博士論文
Version Type	VoR
URL	https://doi.org/10.18910/67136
rights	
Note	

Doctoral Dissertation

Study on Discrete Current Fluctuation in Carbon Nanotube/Redox Active Molecule Hybrid Device

分子·カーボンナノチューブ複合素子に発現する離散的電流変動に関する研究

Agung Setiadi

July 2017
Division of Precision Science and Technology and Applied Physics
Graduate School of Engineering
Osaka University

Abstract

Carbon nanotube (CNT) has attracted many attentions due to its excellent electronic properties. Due to its one-dimensionality, it is well known that the CNT is very sensitive to the environment around its surface. A simple deformation, like bending, and the presence of adsorbed molecules could alter the electronic properties of the CNT itself. Functionalizing the CNT with another molecule is one of the interesting subject to fabricate novel electronic devices.

Electronic transport of CNT field-effect-transistor (FET) is mainly governed by the Schottky barrier at the interface between CNT and metal electrodes. In the case of bottom contact CNT-FET device, the CNT will be bent at the contact point with metal electrodes. It was found that the bending causes the shift of the Fermi level of the CNT towards the valence band as indicated by the down-shift of the G band peak in Raman spectra of CNT. The shift of the Fermi level also resulting in the change of the FET transfer characteristic from ambipolar to p-type characteristic. It was also found that embedding the metal electrodes inside the substrate could maintain the original shape of the CNT at the contact point with metal electrodes.

Molecular functionalization of the CNT open a wide range of potential application in electronic and sensing devices. It was found that the addition of a molecule with high redox activity to a CNT-FET provides tunable current fluctuation noise. A unique charge-trap state in the vicinity of the CNT surface due to the presence of the single molecule generates a prominent and unique noise in the form of random telegraph signal (RTS) and Lorentzian-shaped power spectral density (PSD) in time- and frequency-domain signal, respectively. Distinctive RTS and Lorentzian-shaped PSD in CNT device were observed due to adsorption of protoporphyrin, Zn-protoporphyrin, and phosphomolybdic acid molecules. It is considered that those fluctuation is caused by the single charge trapping-detrapping event which change molecular charge state from neutral to positively or negatively charged.

The fluctuation which were caused by molecular adsorption were utilized to fabricate CNT-based stochastic resonance (SR) devices with self-noise source. SR is an intrinsic noise usage system for small-signal sensing found in various living creatures. The noise-enhanced signal transmission and detection system, which is probabilistic but low-power-consumption, has not been used in modern electronics. Summing network SR device based on multiple-CNT junctions aligned parallel to each other that detects small sub-threshold signals with very low current flow was demonstrated. The nonlinear current-voltage characteristics of this CNT device, which incorporated Cr electrodes, were used as the threshold level of signal detection. The adsorption of redox-active polyoxometalate molecules on CNTs generated additional noise, which was utilized as a self-noise source. The functional capabilities of the present small-size summing network SR device, which rely on dense nanomaterials and exploit intrinsic spontaneous noise at room temperature, offer a glimpse of future bio-inspired electronic devices.

Contents

List of Tables

iv

List of Figures

viii

Chapter 1

General Introduction

1.1 Overview

Rapid advances in information technology, such as artificial intelligence, internet of things, big data analysis, and cryptography, need a powerful computer, processing and storage units, to solve complex computational problems. High performance computer can be obtained using very large scale integration of Si-based transistor to achieve high processing speed. However, high speed processing dramatically increase the power consumption and thermal dissipation which limit device's performance. Moreover, scaling limitation of Si-based electronics also limit further integration. Therefore, many researches were done beyond Si-based electronics technology to develop future electronic devices. Some of area of investigation are carbon-based electronic, molecular electronic, spintronic, and neuromorphic devices.

Carbon-based electronics are considered to be one of the most promising material to replace Si-based electronics. Semiconducting carbon nanotubes (CNT)[1] which exhibit extraordinary electronic properties have a great potential in replacing Si-based electronics. However, the difficulties to fabricate CNT with single chirality is

one of a major obstacles to realize large scale integration of CNT-based electronics.[2] Organic molecules which were mainly made from carbon elements also show great potential owing to the possibility in developing electronic devices at molecular scale. Molecular diode[3] and transistor[4,5] have been constructed only from a single molecule, although such devices are still far from practical application.

Molecular functionalization of CNT can lead to the development of novel electronic devices. Various kind of electronic devices have been developed based-on molecule-functionalized CNT, such as sensing device,[6] molecular movement prober,[7] and noble-metal-free oxygen-reduction-reaction catalyst for fuel cell.[8] On the other hand, molecular functionalization of CNT also induces additional low-frequency noise which might hamper device performance, especially in sensing devices.[9] However, current fluctuation/noise can also be utilized to identify the adsorbed molecules,[10] probe the chemical bonding,[11] to develop Johnson noise thermometer,[12] and to assist signal transmission.[13] Therefore, it is interesting to understand current fluctuation in molecule-functionalized CNT device, in which new kind of devices can also be developed by utilizing newly-generated current fluctuation in CNT device.

1.2   Research objectives

The main objective of this dissertation is to elucidate and utilize the current fluctuation of CNT device due to molecular adsorption. Due to its quasi 1-D structure, CNT is very sensitive to the perturbation on its surface, such as molecular adsorption or deformation. Thus, the basic properties of pristine CNT in CNT device, especially when there is CNT deformation at the interface with metal electrodes, is investigated by comparing the field-effect-transistor (FET) characteristic and Raman spectra of pristine CNT with and without bending. It is considered that adsorption of a single molecule on a CNT might provide prominent current noise which depends on

the electronic properties of the adsorbed molecule. In this research, the physical mechanism of the current fluctuation in CNT device with adsorbed molecules will be clarified. The current fluctuation that caused by the molecular adsorption will also be utilized to develop stochastic resonance (SR) devices with self-noise source. SR is a phenomenon where the noise of the signal can enhance the transmission of the signal itself. The newly fabricated SR device consists of multiple-CNT junctions having non-linear current-voltage characteristic to form summing network SR units and organic molecules which were adsorbed on CNT as noise source.

1.3 Outline of dissertation

This dissertation is divided into two main parts: evaluation of bending effect of the CNT in the bottom contact electrode devices, and elucidation and utilization of current fluctuation in CNT devices that caused by the adsorbed molecules. Chapter 2 briefly explains the background related to this research, such as structural and electronic properties of CNT, Raman spectroscopy of CNT, CNT electronic devices, current noise in CNT devices, and stochastic resonance device.

In chapter 3, the basic characteristic of pristine CNT as electronic device, mainly in bottom contact electrodes device, were investigated by evaluating the transport properties.[14] Commonly, there is a height difference between the substrate and bottom contact electrode leading to a deformation of CNT at the interface. The bending effect of CNT can be eliminated using flattened electrodes which greatly reduce the height difference between the substrate and metal electrodes. In chapter 4, bending effect of the CNT is also investigated using Raman spectroscopy technique by comparing the Raman spectra of the CNT at the interface with metal electrodes in flattened and non-flattened electrodes.[15]

In chapter 5, the discrete current fluctuation of CNT device due to the presence

of adsorbed molecule were elucidated.[16] It is concluded that the current fluctuation of CNT devices depends on the electronic properties of the adsorbed molecule. In chapter 6, the current fluctuation caused by the adsorbed molecules were utilized to develop stochastic resonance devices with self-noise source.[17] Finally, all findings in this dissertation are summarized in chapter 7. The future outlook on the application of molecular current fluctuation in CNT device is also discussed.

References

1. Iijima, S. Helical microtubules of graphitic carbon. *Nature* **354,** 56–58 (1991).

2. Yang, F. *et al.* Chirality-specific growth of single-walled carbon nanotubes on solid alloy catalysts. *Nature* **510,** 522–524 (2014).

3. Capozzi, B. *et al.* Single-molecule diodes with high rectification ratios through environmental control. *Nat. Nanotech.* **10,** 522–527 (2015).

4. Song, H. *et al.* Observation of molecular orbital gating. *Nature* **462,** 1039–1043 (2009).

5. Martínez-Blanco, J. *et al.* Gating a single-molecule transistor with individual atoms. *Nat. Phys.* **11,** 640–644 (2015).

6. Besteman, K., Lee, J.-O., Wiertz, F., Heering, H. & Dekker, C. Enzyme-coated carbon nanotubes as single-molecule biosensors. *Nano Lett.* **3,** 727–730 (2003).

7. Choi, Y. *et al.* Single-molecule lysozyme dynamics monitored by an electronic circuit. *Science* **335,** 319–324 (2012).

8. Hijazi, I. *et al.* Carbon nanotube-templated synthesis of covalent porphyrin network for oxygen reduction reaction. *J. Am. Chem. Soc.* **136,** 6348–6354 (2014).

9. Sharf, T., Kevek, J. W., Deborde, T., Wardini, J. L. & Minot, E. D. Origins of charge noise in carbon nanotube field-effect transistor biosensors. *Nano lett.* **12,** 6380–6384 (2012).

10. Vasudevan, S & Ghosh, A. Using room temperature current noise to characterize single molecular spectra. *ACS Nano* **8,** 2111–2117 (2014).

11. Adak, O. *et al.* Flicker noise as a probe of electronic interaction at metal-single molecule interfaces. *Nano Lett.* **15,** 4143–4149 (2015).

12. Crossno, J, Liu, X, Ohki, T., Kim, P & Fong, K. C. Development of high frequency and wide bandwidth Johnson noise thermometry. *Appl. Phys. Lett.* **106,** 023121 (2015).

13. Russell, D. F., Wilkens, L. A. & Moss, F. Use of behavioural stochastic resonance by paddle fish for feeding. *Nature* **402,** 291–294 (1999).

14. Setiadi, A., Akai-Kasaya, M., Saito, A. & Kuwahara, Y. Advantages of flattened electrode in bottom contact single-walled carbon nanotube field-effect transistor. *Appl. Phys. Lett.* **105,** 093506 (2014).

15. Setiadi, A., Akai-Kasaya, M. & Kuwahara, Y. Raman mapping investigation of single-walled carbon nanotube bending in bottom-contact field-effect-transistor devices. *J. Appl. Phys.* **120,** 094302 (2016).

16. Setiadi, A. *et al.* Room-temperature discrete-charge-fluctuation dynamics of a single molecule adsorbed on a carbon nanotube. *Nanoscale* **9,** 10674–10683 (2017).

17. Fujii, H., Setiadi, A., Kuwahara, Y. & Akai-Kasaya, M. *Single walled carbon nanotube-based stochastic resonance device with molecular self-noise source* submitted to Appl. Phys. Lett.

Chapter 2

Related Background

2.1 Structural and electronic properties of carbon nanotube

Carbon nanotubes (CNT)[1] is one of the carbon allotrope having sp^2 hybridization on each carbon atom. Other carbon allotropes which have the same hybridization are fullerene[2], graphene[3], and graphite. These structures can be seen in Fig. 2.1. Strong chemical bonding of CNT owing to sp^2 hybridization of carbon atoms leads to a superior stability of its structure.[4] The length-to-diameter ratio of the CNT usually exceeds 1000, and thus CNT is regarded as quasi one-dimensional structure.

CNT is also regarded as a rolled version of graphene and the way it rolled is represented by chiral indices (n,m). These indices denote the number of unit vectors of the graphene lattice as illustrated in Fig. 2.2. Based on its electronic properties, there are two types of CNT, metallic and semiconducting CNTs, which depends on the chiral vector[5]. The expression of chiral vector in real space is

$$\mathbf{C}_H = n\mathbf{a}_1 + m\mathbf{a}_2 \tag{2.1}$$
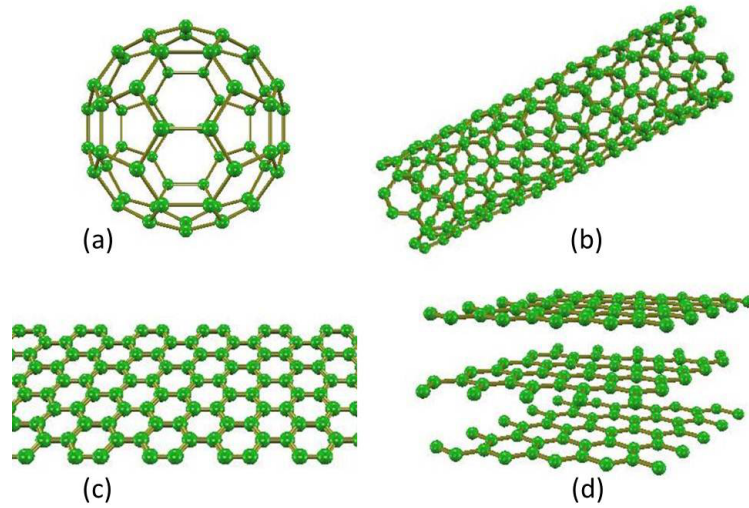
Figure 2.1: Carbon materials, (a) fullerene, (b) carbon nanotubes, (c) graphene, (d) graphite.

where n and m are the integers. If $(n - m) \bmod 3 = 0$, the CNT becomes metallic, otherwise it becomes semiconductor. If $n = m$ the CNT has armchair edge, and if $m = 0$ the CNT has zigzag edge, otherwise the CNT has chiral edge. Electronic structure of the CNT can be depicted with density of states (DOS), which describes the number of states at each energy level. Fig. 2.3 shows the theoretical calculation of DOS of the CNT on different chiral vector. Since this chiral vector defines the circumference structure of the tube, the diameter of the CNT can be estimated by using the following relation:

$$d_t = \frac{a}{\pi}\sqrt{n^2 + nm + m^2} \tag{2.2}$$

where a is the lattice constant of the honeycomb structure. Chiral angle, θ, is obtained from the chiral vector as follow:

$$cos\theta = \frac{2n + m}{2\sqrt{n^2 + nm + m^2}} \tag{2.3}$$

The electronic properties of the CNT induced by their chirality have been studied by using scanning tunnelling microscopy (STM).[7,8] Atomically resolve STM images
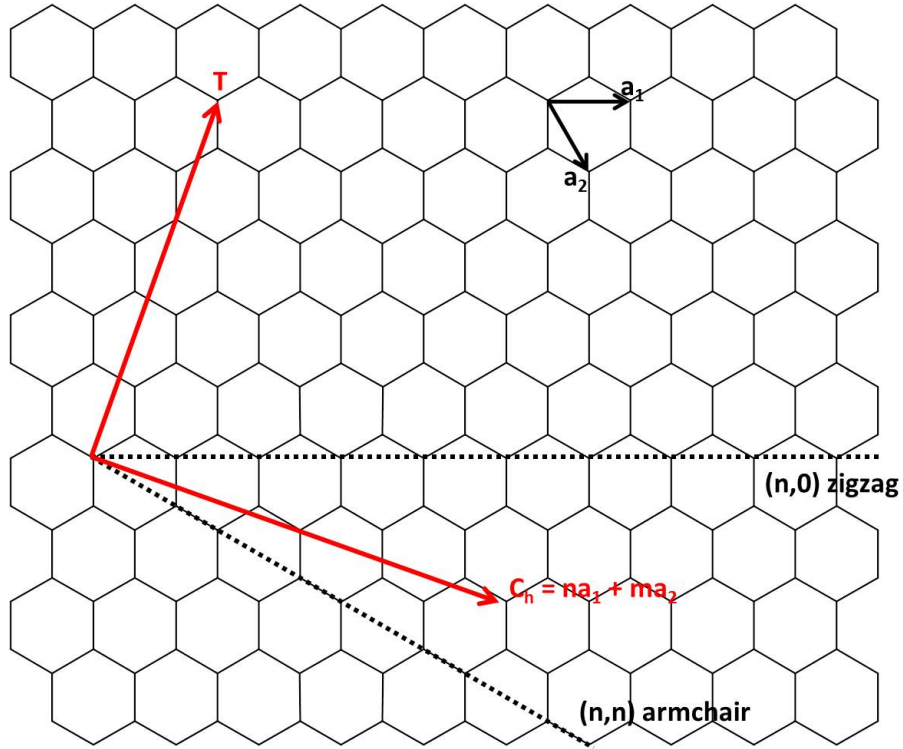
Figure 2.2: Chiral vector of CNT. $\mathbf{C}_h$ is the chiral vector, a_1 and a_2 are the unit vector of graphene lattice, and $\mathbf{T}$ is the tube direction.

allow chiral angle assignment which is shown in Fig. 2.4. Combining chiral angle with the tube diameter allows the assignment of chiral vector, in which theoretical prediction of DOS of CNT can be compared to the experimental observation of local DOS of CNT via scanning tunnelling spectroscopy (STS). In this case, STM and STS observation confirmed the theoretical prediction of the electronic properties of the CNT.[8]

2.2 Raman spectroscopy of carbon nanotube

Raman spectroscopy is a measurement technique which observes the vibrational state of a system due to inelastic scattering of incident photon. Raman spectroscopy usually uses laser from near infrared to near ultraviolet range. It should be noted that not all vibrational states will appear in Raman spectrum due to spectroscopy
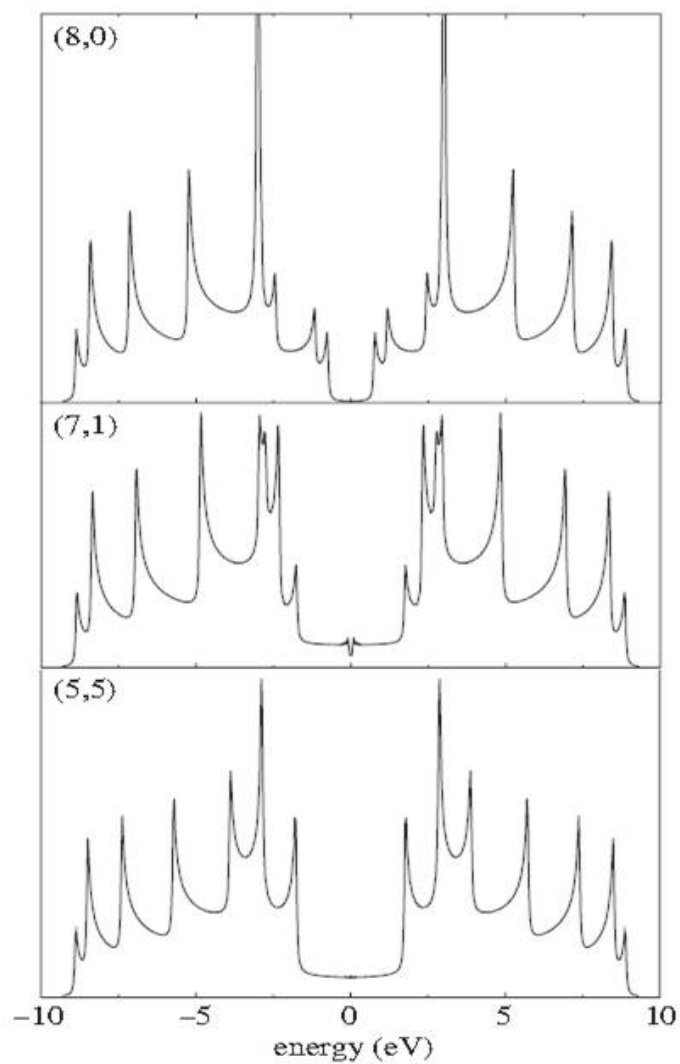
Figure 2.3: Theoretical calculation of the density of states of CNT on different chiral vector. This image was taken from Ref. [6].
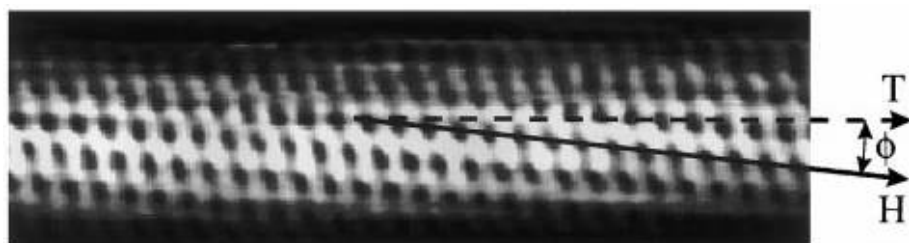
Figure 2.4: Atomically resolve STM image of individual CNT. This image was taken from Ref. [8].
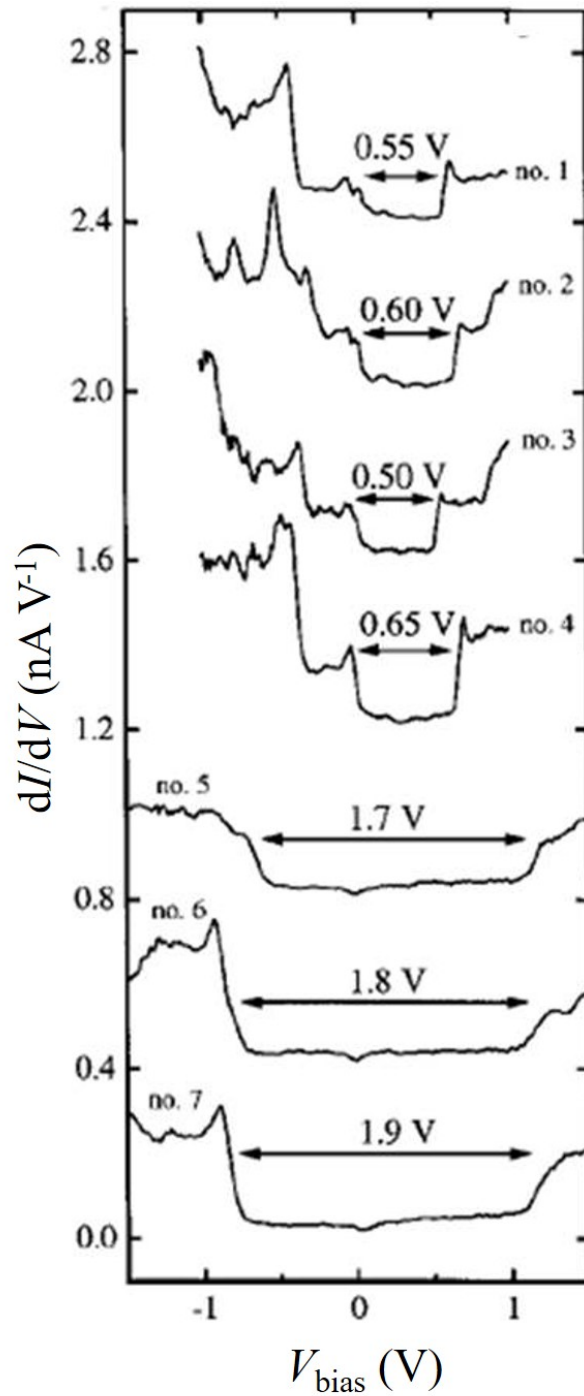
Figure 2.5: Electronic properties of the CNT which was measured by STS. Tubes no 1-6 are chiral CNTs, while tube no 7 is zigzag CNT. This image was taken from Ref. [8].
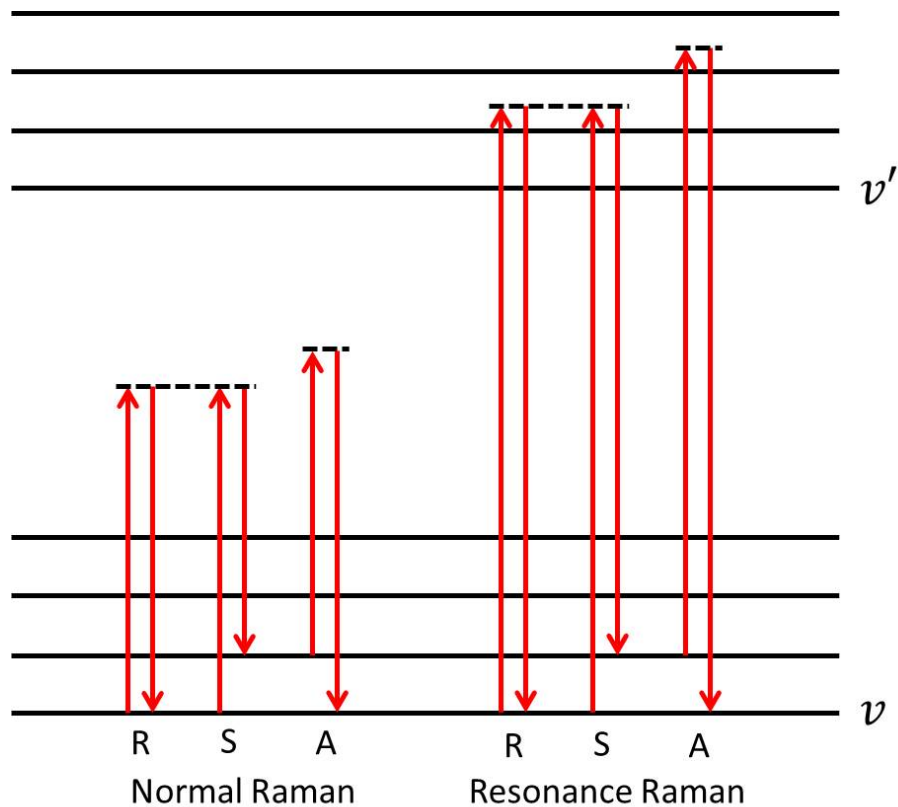
Figure 2.6: Energy level diagram of Raman spectroscopy. R, S, and A are Rayleigh, Stokes, and anti-Stokes scattering, respectively. The dashed lines denote virtual energy states.

selection rule. In addition, a vibrational state is Raman active if the molecule polarization changed upon exposure to the incident photon.[9]

Figure 2.6 shows the energy level diagram of Raman spectroscopy.[9] For normal Raman, an incident photon excites the molecule to a virtual energy state. During relaxation, the molecule returns to a different state than that of before excitation while emitting photon. If the emitted photon has lower energy than the incident photon, it is called Stokes Raman scattering. Otherwise, it is called anti-Stokes Raman scattering. Energy difference between incident and emitted photon is called Raman shift. In resonance Raman spectroscopy, the energy of incident photon coincides with the excited electronic state of the molecule as illustrated in Fig. 2.6, which excites the molecule not to a virtual energy state but to a state near the excited electronic state. When the incident photon energy is tuned near the excited
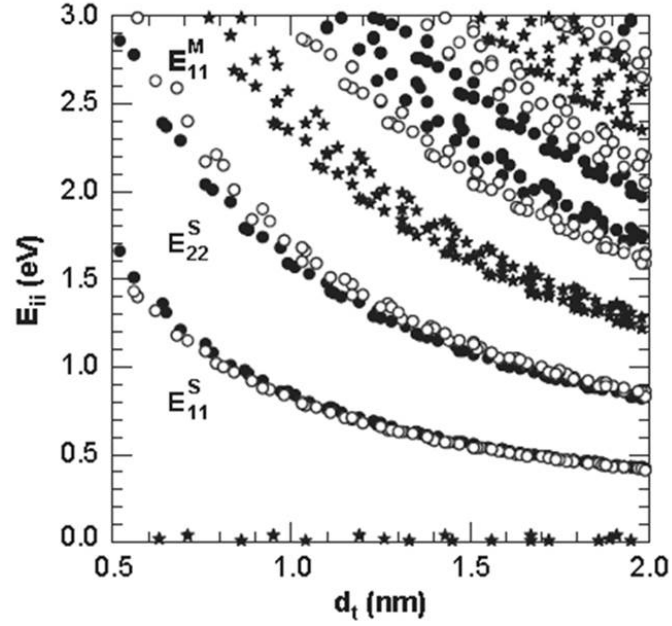
Figure 2.7: Kataura plot of CNT showing the position of the Van Hove singularities for a broad type of CNT. Star and circle denote the metallic and semiconducting CNT, respectively. This image was taken from Ref. [10].

electronic state, that particular vibrational state shows great enhancement of the Raman signal intensity. Raman intensity is increase for approximately 10^3 times due to resonance Raman process.[10]

In the case of CNT, the presence of singularity in the joint density of states (JDOS) also enhances Raman intensity. M.S. Dresselhaus et al. define that "JDOS is density of electronic states that can absorb/emit photons as a function of photon energy".[10] Figure 2.7 shows the position of Van Hove singularities (vHS) of CNT. Raman intensity for CNT is extremely strong when the energy of the incident- or scattered-photon meet the energy of the vHS energy in JDOS curve of that corresponding CNT. Therefore, Raman signal from an individual CNT is measurable as long as the photon energy matches the resonance condition of the corresponding CNT.

Resonance Raman spectra of the CNT can be observed by using laser power as high as 40×10^9 Wm^{-2} due to excellent thermal stability of the CNT.[11] Generally, there are two dominant feature of Raman spectrum of the CNT, a radial breathing mode

(RBM) and a tangential mode. The tangential mode is also called G band. Another feature which describes the amount of defect state in CNT is the disorder band (D band).

The unique feature of the Raman spectra of CNT is an appearance of the RBM. RBM corresponds to the radial vibration of carbon atoms at the same phase which expand and shrink the diameter of the CNT. The RBM peak emerges at frequency between 120 - 350 cm^{-1} depends on the CNT diameter, and thus the position of RBM peak is used to determine diameter of the CNT. The relation between RBM mode and diameter is expressed by the following relation:

$$\omega_{RBM} = \frac{A}{d_t} + B \qquad (2.4)$$

where ω_{RBM} and d_t are the RBM frequency in cm^{-1} and diameter of the CNT, respectively. A and B are the constant parameters which are obtained from the experimental results. For CNT on oxidized silicon substrate, the value of A and B are 248 and 0, respectively.[12]

In order to observe RBM mode of the CNT, the laser energy should be matched with the resonance condition as shown in Fig. 2.7. For example, by using incident laser with wavelength of 523 nm, the RBM mode of semiconducting CNTs having diameter $\approx$ 1.5 nm is observed while no Raman signal for metallic CNTs having the same diameter. Full width at half maximum (FWHM) value of RBM peak also indicates the condition of the CNT whether in bundled or individual state. FWHM of the RBM peak of individual CNT on SiO$_2$ substrate is found to be 3 cm^{-1}.

There are two G band modes in CNT, G^- and G^+, that come from the curvature effect of the CNT. G^- band peak has lower frequency than that of G^+ band peak. In the case of graphite or graphene, there is only one G band peak at $\approx$ 1580 cm^{-1}. Figure 2.8 shows the Raman spectrum of the graphite, semiconducting, and metallic
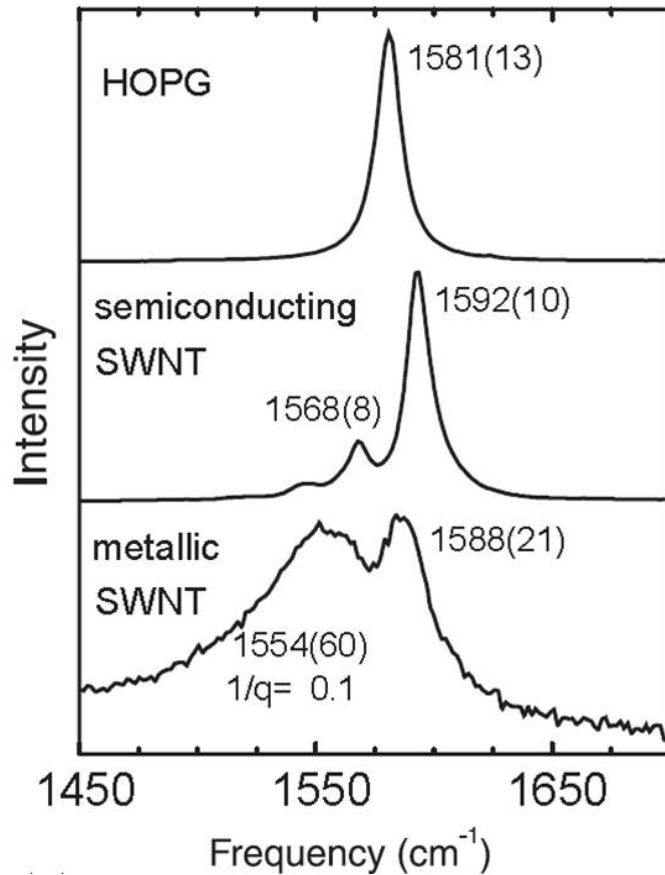
Figure 2.8: Raman spectrum of the graphite, semiconducting, and metallic CNT. This image was taken from Ref. [10].

CNT around G band mode. G band peaks of the CNT can be used to determine the diameter of the CNT and to distinguish metallic and semiconducting CNT.

An interesting feature of the G band of the CNT is that it can be used to distinguish metallic and semiconducting CNT. G^+ band peak corresponds to the vibration of carbon atoms on the direction of nanotube axis. The frequency of the G^+ can be shifted, up or down, due to the presence of dopant on CNT. On the other hand, G^- band corresponds to the vibration of carbon atoms on the direction of CNT circumference. Semiconducting CNTs have Lorentzian shape of the G^- band, while Breit-Wigner-Fano (BWF) lineshape is owned by metallic CNTs as can be seen in

14

Fig. 2.8. The BWF lineshape is represented by the following relation:

$$I(\omega) = I_0 \frac{[1 + (\omega - \omega_{BWF})/q\Gamma]^2}{1 + [(\omega - \omega_{BWF})/\Gamma]^2} \tag{2.5}$$

where $1/q$ is the asymmetry parameter of the shape. If the value of q is very large, the peak becomes a normal Lorentzian lineshape. While ω_{BWF}, I_0, and Γ are fitting parameter at the central frequency, peak intensity, and broadening factor, respectively.[10] Since G^+ and G^- bands are independent on the chirality, diameter of the CNT can be estimated by the following relation:

$$\omega_G^- = \omega_G^+ - \frac{\zeta}{d_t^2} \tag{2.6}$$

where $\zeta = 47.7$ [$cm^{-1}nm^2$] for semiconducting CNT and $\zeta = 79.5$ $cm^{-1}nm^2$ for metallic CNT.[13]

Previous study shows that the G band position also depend on the position of the Fermi level. Both theoretical[14] and experimental[15] studies show that by applying gate voltage, the G band of the CNT were shifted than that of zero gate voltage. In the case of metallic CNT, G band peak shifts to a higher frequency for both holes and electrons doping. During the electron doping, G band peak is down-shifted until $E_F = 0.1$ eV then it starts to shift to a higher frequency [see Fig. 2.9]. Similar case also appears for the semiconducting CNT [see Fig. 2.10]. It is shown that the G band shift to a lower frequency then at some points it starts to increase as the gate voltage increases [Fig. 2.11].

Another important band in Raman spectrum of the CNT is the disorder band (D band) which is located around 1350 cm^{-1}. This band is related to the structural defect of the CNT and its intensity corresponds to the degree of disorder. G/D ratio is used to describe the perfectness of CNT in term of structural defect.[16–18] For as-grown-CVD-type CNT, the G/D ratio is found to be ≈ 45. However, the G/D
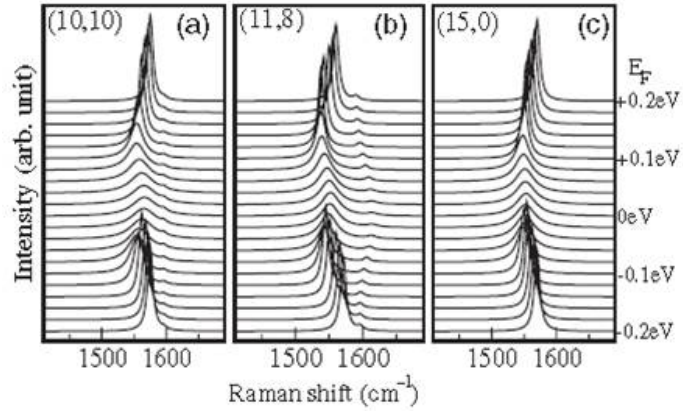
Figure 2.9: Theoretical Raman spectrum of the metallic CNT at different gate voltage. (a), (b), and (c) images are on the different chirality. This image was taken from Ref. [14].
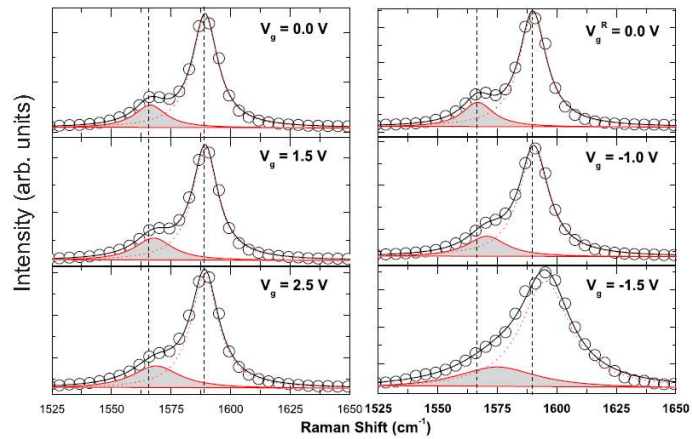
Figure 2.10: Experimental Raman spectrum of the semiconducting CNT at different gate voltage. Circle and lines are experimental and fitting data, respectively. This image was taken from Ref. [15].
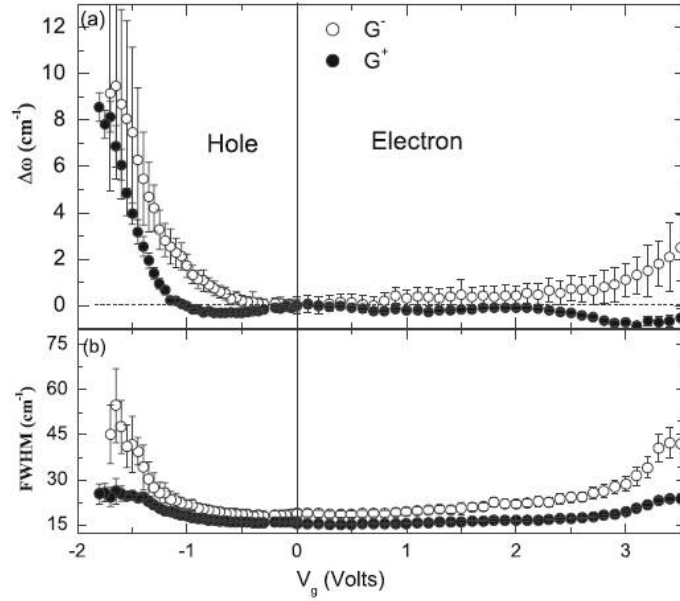
Figure 2.11: Position shifting (a) and FWHM (b) of G^+ and G^- peak as a function of applied gate voltage. Close and open circle denote G^+ and G^- peak, respectively. This image was taken from Ref. [15].

ratio of purified commercial CNT sample is lower than that of as-grown CNT due to purification method which include heat and acid treatments.[19]

2.3 Carbon nanotube electronic devices

CNTs have a wide range of potential application from nanoscale to macroscale. Most of them are in the development of CNT-based electronic device as the CNT has a potential to replace Si based electronic devices.[20–35] Development of CNT electronic devices is based on field-effect-transistor (FET) characteristic. Compared to the graphene, CNT is more suitable for the development of carbon-based FET due to intrinsic band gap owned by semiconducting CNT. Due to one-dimensionality of the CNT, the electrons are confined to move only in two direction and provide longer mean free path than that of higher dimensional structure leading to a high carrier mobility. The highest field-effect-mobility of CNT-FET device exceeds > 79000 cm^2/Vs at room temperature for extremely long CNT with the length of $\approx$ 200
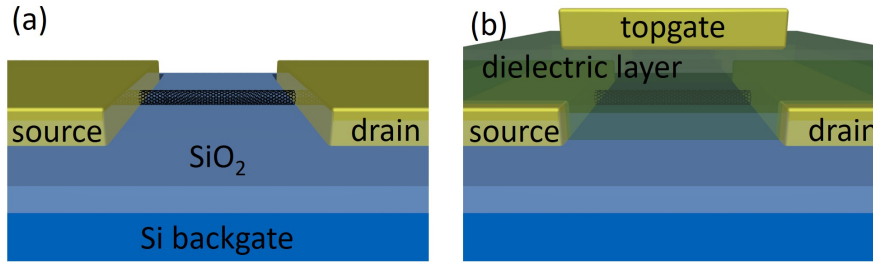
Figure 2.12: CNT-FET devices structure with (a) backgate and (b) topgate electrodes.

μm.[20]

Similar to Si-FET, CNT-FET devices consist of source, drain, and gate electrodes. The gate electrodes are originated either from backgate or topgate electrodes and are separated from the CNT channel using dielectric layer as shown in Fig. 2.12. Basic operation of CNT-FET devices is also similar to the Si-FET though the Schottky barrier (SB) in CNT plays an important role in determining the FET characteristic of the CNT. In CNT-FET device, the gate electrodes modulate the conductance of the CNT by tuning the number of charge carriers and the SB at the interface between CNT and source-drain electrodes. The FET characteristic of CNT device is p-type, n-type, or ambipolar, which depend on the electrodes material and the surrounding environment. High work-function of metal electrodes can lead to the p-type CNT-FET devices, while n-type for the low work function one. If the work function of the metal is located at the center of the band gap of the CNT, it will provide ambipolar characteristic. Under ambient condition, the CNT usually shows p-type characteristic due to natural doping from oxygen gas, while ambipolar or n-type under vacuum condition for a certain material of metal electrodes. Introducing the dopant to the CNT using organic molecules[36] or K atoms[37] can change the characteristic of the CNT to n-type. Tuning the characteristic of the CNT is very important for the development of the integrated logic devices using individual CNT.[37]

Charge carrier mobility of CNT devices in linear region is evaluated using the following equation[23]:

$$\mu = \frac{L^2}{C_g V_D} \left(\frac{dI_D}{dV_G} \right) \tag{2.7}$$

where L, C_g, V_D, and $\frac{dI_D}{dV_G}$ are channel length, gate capacitance, drain voltage, and transconductance, respectively. In the case of CNT-FET consisting thin film CNTs, the C_g is evaluated using parallel plate capacitor model of $C_g = \epsilon\epsilon_0 WL/t_{ox}$, where ϵ, W, t_{ox} are dielectric factor, channel width, and the thickness of the dielectric layer, respectively. In the case of individual CNTs, the C_g is provided by $C_g = 2\pi\epsilon\epsilon_0/\ln(4t_{ox}/d)$, where d is the diameter of the CNT.

2.4   Noise in carbon nanotube electronic device

It is known that electronic devices based-on low-dimensional material suffer from low frequency noise. Low frequency noise at room temperature consists of three main components; thermal noise, generation-recombination (GR) noise, and flicker noise.[38] Thermal noise is originated from random motion of the charge carriers at a certain temperature and does not have dependency on frequency, f. The spectral density of thermal noise is defined as $S_T = 4k_B TR$, where k_B, T, and R are Boltzmann constant, temperature, and resistance, respectively. The GR noise is originated from the trapping-detrapping events of charge carriers from/to the charge traps. In electronics, such as FET devices, the charge traps are originated from the structural defect of channel material, defects on/in the dielectric layer, or adsorbed gas molecules from the environment. The spectral density of GR noise is described as $S_{GR} \propto \tau/\left[1 + (2\pi\tau)^2\right]$, where τ is the time constant of charge trapping-detrapping event. Single event of GR noise consists of a step-like fluctuation in time domain signal called random telegraph signal (RTS), and has Lorentzian-shaped spectral density as shown in Fig. 2.13. The flicker noise is a frequency-dependent-noise and

19
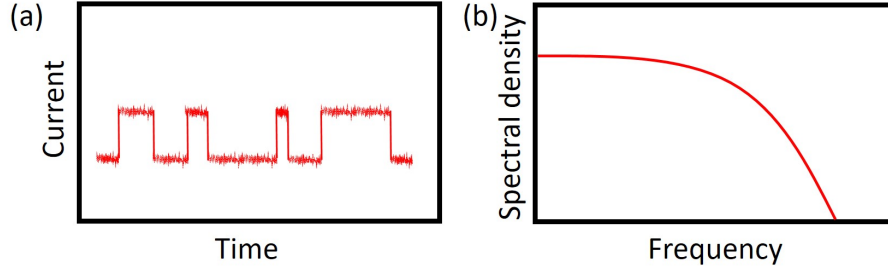
Figure 2.13: Single GR event in (a) time and (b) frequency domain signal.

described as $S_F \propto 1/f^\gamma$. In most of the electronic devices, γ nearly equal to 1. The flicker noise can also be understood as superposition of multiple GR noise events with a wide distribution of time constant τ. Hence, the spectral density of current noise is described in a general form as follows[38]:

$$S(f) = \frac{A}{f^\gamma} + \sum_i \frac{B_i}{1 + (2\pi f \tau_i)^2} + 4k_B TR \qquad (2.8)$$

The origin of flicker noise in electronic devices is originated from the fluctuation in the channel and at the interface with metal electrodes. There are two possible origins of current fluctuation in the channel; fluctuation of charge mobility and total number of charge carrier.[39] Empirical formula of flicker noise is in the form $S_F = \alpha_H I^2/fN$, where α_H and N are Hooge parameter and number of carriers, respectively.[40] In the case of mobility fluctuation, α_H is independent of gate voltage, V_g, while V_g dependent in fluctuation of number of carrier of $\alpha_H \propto 1/|V_g - V_{th}|$.[39]

Previous studies showed that in CNT-FET devices, the amplitude of flicker noise, A, depend on the V_g.[41–44] The "A" decrease monotonically when the current increase due to applied V_g. An increase in the current at constant bias means that the total resistance of the device is decreased. Hence, it can be deduced that the "A" is proportional to the resistance of the device which comes from both channel and contact, coming from SB, resistance related to the number and transmission probability of charge carrier, respectively. In the case of diffusive CNT-FET device,

20

the flicker noise depends on R_c and R_{SB}, while only on R_{SB} in the case of ballistic CNT-FET device. It has also been shown that the "A" is independent to the carrier type.[42]

Appearance of single-event GR noise, which is referred to as RTS in time domain signal, is very interesting since it might come from a single trap and thus include the information of the charge trap. The RTS has been observed in Si-MOSFET,[45,46] Si-nanowire FET,[47,48] and also CNT-FETs.[49–52] The origin of RTS is charge trapping-detrapping event of a charge trap in/on dielectric layer. When a single charge enters a shallow trap site, at a distance around 2-3 nm, it provides significant change of the conductance which is not proportional to dI/dV_g. By extracting the characteristic of the RTS, the location and energy level of the charge trap inside dielectric layer can be estimated.[48,50,51] In CNTs, the RTS is also originated from adsorbed-quantum-dot,[53] chemical reaction on CNT surface,[54–56] adsorption-desorption of ionized gas molecule,[57] and step-motion of protein molecule on CNT surface[58].

2.5   Stochastic resonance device

Generally, noise is regarded as harmful properties of electronic device. Hence, many attempts were done to eliminate the noise for improving the device performance. However, the noise can be used to assist the signal transmission, called stochastic resonance (SR) effect.[59,60] Many biological[61–66] and physical[67–69] systems exploit SR effect to enhance the detection of the signal below threshold level. In the nature, paddlefish and crayfish utilize SR effect exploiting electrical and mechanical background noise to detect their distant prey or predator, respectively.[61–64] SR effect has also been utilized to increase the visual processing ability of human brain by adding external noise.[70,71]

The basic mechanism of SR effect is shown in Fig. 2.14. If there is an input signal
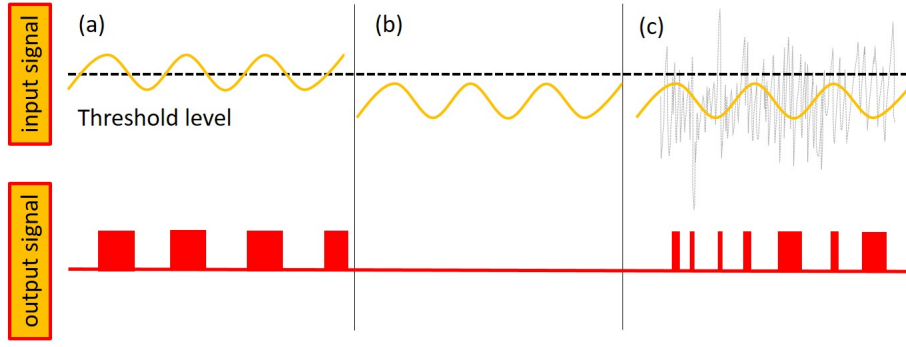
Figure 2.14: Relation between input - output signal at three condition: (a) input signal above threshold level, (b) input signal below threshold level, and (c) input signal below threshold level with additional noise. Horizontal dashed-line represent the threshold level.

which is lower than threshold level, no output signal is observed by the detector. When an external noise is added to the input signal, one can detect output signal correlated to the input signal through the resonance with the inserted noise. The optimization of the noise intensity is very important to obtain significant enhancement of signal transmission of below threshold signal as shown in Fig. 2.15.[59,60] The correlation coefficient between input-output signal is evaluated using the following equation:

$$CC = \frac{\langle S_{in} S_{out} \rangle - \langle S_{in} \rangle \langle S_{out} \rangle}{\sqrt{\left(\langle S_{in}^2 \rangle \langle -S_{in} \rangle^2\right)\left(\langle S_{out}^2 \rangle \langle -S_{out} \rangle^2\right)}} \qquad (2.9)$$

where S_{in} and S_{out} are input and output signal, respectively.

Collins, et al. proposed a new SR system utilizing summing network without optimization of the noise intensity.[72] Their model is shown in Fig. 2.16(a). In their summing network, each junction has independent noise. Then, significant enhancement of signal transmission without tuning the noise intensity is obtained by summing the output signal from each junction as shown in Fig. 2.16(b). In this model, the correlation coefficient has a weaker dependence upon noise intensity when the number of junctions is large enough (1000 junctions) as shown in Fig. 2.16(c). It has also been shown that the correlation coefficient does not significantly decrease at deeper sub-threshold level comparing to that without any external noise (Fig.
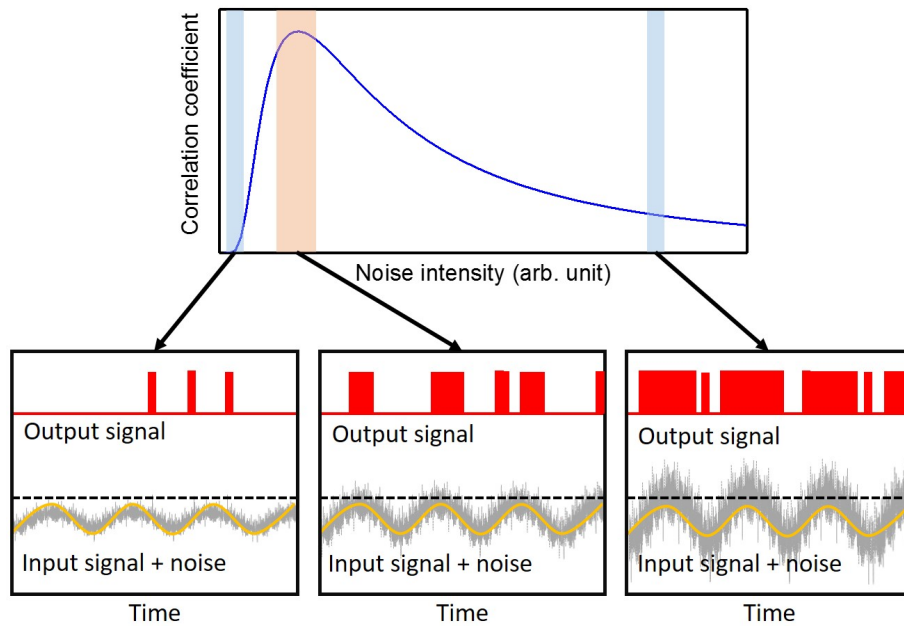
Figure 2.15: Correlation coefficient of an SR system as a function of noise intensity which clearly shows that optimized noise intensity is necessary to obtain significant enhancement of signal transmission. Horizontal dashed-line is the threshold level.

2.16(d)).

According to the study by Collins, et al., there are three main requirements to develop SR device without the tuning of noise intensity; signal detection threshold, additional noise, and multiple junctions. The potential of SR system such as detecting small input signal below threshold level leads to many research in the development of electronic device utilizing SR effect.[73–82] The multiple junctions SR system have been demonstrated in Si-nanowire FETs,[73] GaAs nanowire FETs,[74–76] CNT-FETs,[77–79], DNA networks with a molecular redox circuit,[80,81], and VO_2 thin films having phase transition threshold[82].

References

1. Iijima, S. Helical microtubules of graphitic carbon. *Nature* **354,** 56–58 (1991).

2. Kroto, H. W., Heath, J. R., O'Brien, S. C., Curl, R. F. & Smalley, R. E. C60: Buckminsterfullerene. *Nature* **318,** 162–163 (1985).
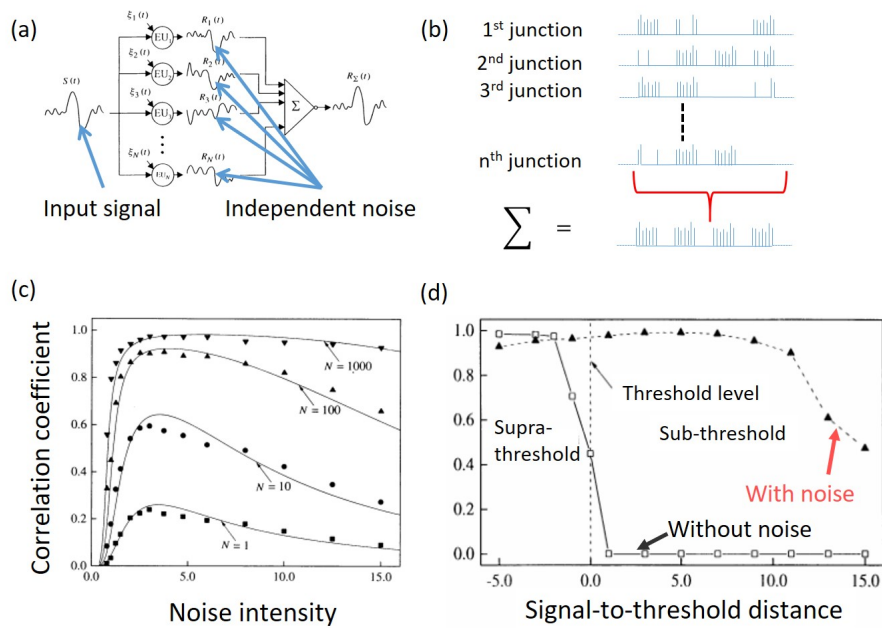
Figure 2.16: (a) SR system based on summing network. Independent noise were applied to each junction. (b) Output signal were obtained by summing the output from each junction. The images were taken from Ref. [72].

3. Novoselov, K. S. *et al.* Electric field effect in atomically thin carbon films. *Science* **306,** 666–669 (2004).

4. Avouris, P. Molecular electronics with carbon nanotubes. *Acc. Chem. Res.* **35,** 1026–1034 (2002).

5. Charlier, J.-C. Defects in Carbon Nanotubes. *Acc. Chem. Res.* **35,** 1063–1069 (2002).

6. Dresselhaus, M. S., Dresselhaus, G., Charlier, J. C. & Hernández, E. Electronic, thermal and mechanical properties of carbon nanotubes. *Phil. Trans. R. Soc. Lond. A* **362,** 2065–2098 (2004).

7. Odom, T. W., Huang, J. L., Kim, P. & Lieber, C. M. Atomic structure and electronic properties of single-walled carbon nanotubes. *Nature* **391,** 62–64 (1998).

8. Wildöer, J. W., Venema, L. C., Rinzler, A. G., Smalley, R. E. & Dekker, C. Electronic structure of atomically resolved carbon nanotubes. *Nature* **391,** 59–62 (1998).

9. Ferraro, J. R., Nakamoto, K & Brown, C. W. *Introductory Raman Spectroscopy* Second edition (Academic Press, 2003).

10. Dresselhaus, M., Dresselhaus, G., Saito, R. & Jorio, A. Raman spectroscopy of carbon nanotubes. *Physics Reports* **409** (2005).

11. Berber, S., Kwon, Y.-K. & Tománek, D. Unusually high thermal conductivity of carbon nanotubes. *Phys. Rev. Lett.* **84,** 4613–4616 (2000).

12. Jorio, A. *et al.* Structural (n, m) determination of isolated single-wall carbon nanotubes by resonant Raman scattering. *Phys. Rev. Lett.* **86,** 1118–1121 (2001).

13. Dresselhaus, M., Dresselhaus, G., Jorio, A., Filho, A. & Saito, R. Raman spectroscopy on isolated single wall carbon nanotubes. *Carbon* **40,** 2043–2061 (2002).

14. Park, J. *et al.* Fermi energy dependence of the G-band resonance Raman spectra of single-wall carbon nanotubes. *Phys. Rev. B* **80,** 081402(R) (2009).

15. Das, A. & Sood, A. Renormalization of the phonon spectrum in semiconducting single-walled carbon nanotubes studied by Raman spectroscopy. *Phys. Rev. B* **79,** 235429 (2009).

16. Itkis, M. E., Perea, D. E., Jung, R., Niyogi, S. & Haddon, R. C. Comparison of analytical techniques for purity evaluation of single-walled carbon nanotubes. *J. Am. Chem. Soc.* **127,** 3439–3448 (2005).

17. Pimenta, M. A. *et al.* Studying disorder in graphite-based systems by Raman spectroscopy. *Phys. Chem. Chem. Phys.* **9,** 1276–1290 (2007).

18. Chen, G. *et al.* Absence of an ideal single-walled carbon nanotube forest structure for thermal and electrical conductivities. *ACS Nano* **7,** 10218–10224 (2013).

19. Cao, Q., Han, S.-J. J., Tulevski, G. S., Franklin, A. D. & Haensch, W. Evaluation of field-effect mobility and contact resistance of transistors that use solution-processed single-walled carbon nanotubes. *ACS Nano* **6,** 6471–6477 (2012).

20. Dürkop, T., Getty, S. A., Cobas, E. & Fuhrer, M. S. Extraordinary mobility in semiconducting carbon nanotubes. *Nano Lett.* **4,** 35–39 (2004).

21. Javey, A., Guo, J., Wang, Q., Lundstrom, M. & Dai, H. Ballistic carbon nanotube field-effect transistors. *Nature* **424,** 654–657 (2003).

22. Zhang, D. *et al.* Transparent, conductive, and flexible carbon nanotube films and their application in organic light-emitting diodes. *Nano Lett.* **6,** 1880–1886 (2006).

23. Yang, M. H. *et al.* Advantages of top-gate, high-k dielectric carbon nanotube field-effect transistors. *Appl. Phys. Lett.* **88,** 113507 (2006).

24. Borghetti *et al.* Optoelectronic switch and memory devices based on polymer-functionalized carbon nanotube transistors. *Adv. Mater.* **18,** 2535–2540 (2006).

25. Yu, W. *et al.* Adaptive logic circuits with doping-free ambipolar carbon nanotube transistors. *Nano Lett.* **9,** 1401–1405 (2009).

26. Wang, S. *et al.* High-performance carbon nanotube light-emitting diodes with asymmetric contacts. *Nano lett.* **11,** 23–29 (2010).

27. Rinkiö, M., Johansson, A., Paraoanu & Torma, P. High-speed memory from carbon nanotube field-effect transistors with high-κ gate dielectric. *Nano Lett.* **9,** 643–647 (2009).

28. Franklin, A. *et al.* Sub-10 nm carbon nanotube transistor. *Nano Lett.* **12,** 758–762 (2012).

29. Franklin, A. *et al.* Carbon nanotube complementary wrap-gate transistors. *Nano Lett.* **13,** 2490–2495 (2013).

30. Tsai, C.-L., Xiong, F., Pop, E. & Shim, M. Resistive random access memory enabled by carbon nanotube crossbar electrodes. *ACS Nano* **7,** 5360–5366 (2013).

31. Cao, Xia, M., Shim & Rogers, J. Bilayer organic–inorganic gate dielectrics for high-performance, low-voltage, single-walled carbon nanotube thin-film transistors, complementary logic gates, and p–n diodes on plastic substrates. *Adv. Funct. Mater.* **16,** 2355–2362 (2006).

32. Lee, C., Sharma, R., Radadia, A., Masel, R. & Strano, M. On-chip micro gas chromatograph enabled by a noncovalently functionalized single-walled carbon nanotube sensor array. *Angew. Chem. Int. ed.* **47,** 5018–5021 (2008).

33. Kauffman, D. & Star, A. Electronically monitoring biological interactions with carbon nanotube field-effect transistors. *Chem. Soc. Rev.* **37,** 1197–1206 (2008).

34. Esser, B., Schnorr, J. & Swager, T. Selective detection of ethylene gas using carbon nanotube-based devices: utility in determination of fruit ripeness. *Angew. Chem. Int. ed.* **51,** 5752–5756 (2012).

35. LeMieux, M. C. *et al.* Self-sorted, aligned nanotube networks for thin-film transistors. *Science* **321,** 101–104 (2008).

36. Dai, H. Carbon nanotubes: Synthesis, integration, and properties. *Acc. Chem. Res.* **35,** 1035–1044 (2002).

37. Derycke, V., Martel, R., Appenzeller, J. & Avouris, P. Carbon nanotube inter- and intramolecular logic gates. *Nano Lett.* **1,** 453–456 (2001).

38. Vitusevich, S. & Gasparyan, F. in *Carbon nanotubes applications on electron devices* (ed Arulanda, J. M.) chap. 11 (InTech, 2011).

39. Vandamme, L. K. J., Li, X. & Rigaud, D. 1/f noise in MOS devices, mobility or number fluctuations? *IEEE Trans. Electron Devices* **41,** 1936–1945 (1994).

40. Hooge, F. N., Kleinpenning, T. G. M. & Vandamme, L. K. J. Experimental studies on 1/f noise. *Rep. Prog. Phys.* **44,** 479–532 (1981).

41. Snow, E. S., Novak, J. P., Lay, M. D. & Perkins, F. K. 1f noise in single-walled carbon nanotube devices. *Appl. Phys. Lett.* **85,** 4172–4174 (2004).

42. Lin, Y.-M., Appenzeller, J., Knoch, J., Chen, Z. & Avouris, P. Low-frequency current fluctuations in individual semiconducting single-wall carbon nanotubes. *Nano Lett.* **6,** 930–936 (2006).

43. Tersoff, J. Low-frequency noise in nanoscale ballistic transistors. *Nano Lett.* **7,** 194–198 (2007).

44. Tobias, D. *et al.* Origins of 1f noise in individual semiconducting carbon nanotube field-effect transistors. *Phys. Rev. B* **77,** 033407 (2008).

45. Ralls, K. *et al.* Discrete resistance switching in submicrometer silicon inversion layers: Individual Interface Traps and Low-Frequency (1/f) Noise. *Phys. Rev. Lett.* **52,** 228 (1984).

46. Uren, M., Kirton, M. & Collins, S. Anomalous telegraph noise in small-area silicon metal-oxide-semiconductor field-effect transistors. *Phys. Rev. B* **7,** 8346 (1988).

47. Zhuge, J, Zhang, L, Wang, R & Huang, R. Random telegraph signal noise in gate-all-around silicon nanowire transistors featuring Coulomb-blockade characteristics. *Appl. Phys. Lett.* **94,** 083503 (2009).

48. Clément, N, Nishiguchi, K, Fujiwara, A & Vuillaume, D. One-by-one trap activation in silicon nanowire transistors. *Nat. Commun.* **1,** 92 (2010).

49. Peng, Hughes & Golovchenko. Room-temperature single charge sensitivity in carbon nanotube field-effect transistors. *Appl. Phys. Lett.* **104,** 243502 (2006).

50. Liu, F. & Wang, K. L. Correlated random telegraph signal and low-frequency noise in carbon nanotube transistors. *Nano Lett.* **8,** 147–151 (2008).

51. Chan, J. *et al.* Reversal of current blockade in nanotube-based field effect transistors through multiple trap correlations. *Phys. Rev. B* **80,** 033402 (2009).

52. Sharf, T. *et al.* Single electron charge sensitivity of liquid-gated carbon nanotube transistors. *Nano Lett.* **14,** 4925–4930 (2014).

53. Zbydniewska, E. *et al.* Charge blinking statistics of semiconductor nanocrystals revealed by carbon nanotube single charge sensors. *Nano Lett.* **15,** 6349–6356 (2015).

54. Goldsmith, B., Coroneus, J., Kane, A., Weiss, G. & Collins, P. Monitoring single-molecule reactivity on a carbon nanotube. *Nano Lett.* **8,** 189–194 (2008).

55. Sorgenfrei, S. *et al.* Label-free single-molecule detection of DNA-hybridization kinetics with a carbon nanotube field-effect transistor. *Nat. Nanotech.* **6,** 126–132 (2011).

56. Bouilly, D. *et al.* Single-molecule reaction chemistry in patterned nanowells. *Nano Lett.* **16,** 4679–4685 (2016).

57. Bushmaker, A. *et al.* Single-ion adsorption and switching in carbon nanotubes. *Nat. Commun.* **7,** 10475 (2016).

58. Choi, Y. *et al.* Single-molecule lysozyme dynamics monitored by an electronic circuit. *Science* **335,** 319–324 (2012).

59. McNamara, B. & Wiesenfeld, K. Theory of stochastic resonance. *Phys. Rev. A* **39,** 4854–4869 (1989).

60. Gammaitoni, L., Hänggi, P., Jung, P. & Marchesoni, F. Stochastic resonance. *Rev. Mod. Phys.* **70,** 223–287 (1998).

61. Douglass, J., Wilkens, L., Pantazelou, E. & Moss, F. Noise enhancement of information transfer in crayfish mechanoreceptors by stochastic resonance. *Nature* **365,** 337–340 (1993).

62. Russell, D. F., Wilkens, L. A. & Moss, F. Use of behavioural stochastic resonance by paddle fish for feeding. *Nature* **402,** 291–294 (1999).

63. Greenwood, P., Ward, L., Russell, D., Neiman, A. & Moss, F. Stochastic resonance enhances the electrosensory information available to paddlefish for prey capture. *Phys. Rev. Lett.* **84,** 4773–4776 (2000).

64. Bahar, S. & Moss, F. Stochastic resonance and synchronization in the crayfish caudal photoreceptor. *Math. Biosci.* **188,** 81–97 (2004).

65. Spezia, S. *et al.* Evidence of stochastic resonance in the mating behavior of Nezara viridula (L.) *Eur. Phys. J. B* **65,** 453–458 (2008).

66. Manjarrez, E. *et al.* Internal stochastic resonance in the coherence between spinal and cortical neuronal ensembles in the cat. *Neuroscience Letters* **326,** 93–96 (2002).

67. Mantegna, R. N. & Spagnolo, B. Stochastic resonance in a tunnel diode in the presence of white or coloured noise. *Il Nuovo Cimento D* **17,** 873–881 (1995).

68. Mantegna, R. N., Spagnolo, B., Testa, L. & Trapanese, M. Stochastic resonance in magnetic systems described by Preisach hysteresis model. *J. Appl. Phys.* **97,** 10E519 (2005).

69. La Cognata, A., Valenti, D., Dubkov, A. A. & Spagnolo, B. Dynamics of two competing species in the presence of Lévy noise sources. *Phys. Rev. E* **82,** 011121 (2010).

70. Mori, T. & Kai, S. Noise-induced entrainment and stochastic resonance in human brain waves. *Phys. Rev. Lett.* **88,** 218101 (2002).

71. Kitajo, K., Nozaki, D., Ward, L. M. & Yamamoto, Y. Behavioral stochastic resonance within the human brain. *Phys. Rev. lett.* **90,** 218103 (2003).

72. Collins, J, Chow, C & Imhoff, T. Stochastic resonance without tuning. *Nature* **376,** 236–238 (1995).

73. Nishiguchi, K. & Fujiwara, A. Detecting signals buried in noise via nanowire transistors using stochastic resonance. *Appl. Phys. Lett.* **101,** 193108 (2012).

74. Samardak, A. *et al.* Noise-controlled signal transmission in a multithread semiconductor neuron. *Phys. Rev. Lett.* **102,** 226802 (2009).

75. Kasai, S. & Asai, T. Stochastic Resonance in Schottky Wrap Gate-controlled GaAs Nanowire Field-Effect Transistors and Their Networks. *Appl. Phys. Express* **1,** 083001 (2008).

76. Kasai, S., Miura, K. & Shiratori, Y. Threshold-variation-enhanced adaptability of response in a nanowire field-effect transistor network. *Appl. Phys. Lett.* **96,** 194102 (2010).

77. Lee, I., Liu, X., Kosko, B. & Zhou, C. Nanosignal processing: Stochastic resonance in carbon nanotubes that detect subthreshold signals. *Nano Lett.* **3,** 1683–1686 (2003).

78. Hakamata, Y. *et al.* Enhancement of weak-signal response based on stochastic resonance in carbon nanotube field-effect transistors. *J. Appl. Phys.* **108,** 104313 (2010).

79. Hakamata, Y., Ohno, Y., Maehashi, K., Inoue, K. & Matsumoto, K. Robust noise characteristics in carbon nanotube transistors based on stochastic resonance and their summing networks. *Jpn. J. Appl. Phys.* **50,** 06GE03 (2011).

80. Hirano, Y., Segawa, Y., Kawai, T. & Matsumoto, T. Stochastic resonance in a molecular redox circuit. *J. Phys. Chem. C* **117,** 140–145 (2013).

81. Hirano, Y., Segawa, Y., Kuroda-Sowa, T., Kawai, T. & Matsumoto, T. Conductance with stochastic resonance in Mn_{12} redox network without tuning. *Appl. Phys. Lett.* **104,** 233104 (2014).

82. Kanki, T., Hotta, Y., Asakawa, N., Kawai, T. & Tanaka, H. Noise-driven signal transmission using nonlinearity of VO2 thin films. *Appl. Phys. Lett.* **96,** 242108 (2010).

Chapter 3

Advantage of Flattened Electrodes in Carbon Nanotube Field-Effect-Transistor

3.1 Introduction

Since the discovery of carbon nanotubes (CNTs)[1], high performance CNT field effect transistor (FET) devices, especially those using single-walled carbon nanotubes (SWNTs), were fabricated by the chemical vapor deposition (CVD) method[2–4]. There are several methods to deposit CNTs via a solution process, such as drop casting[5,6], spin coating[7], AC-dielectrophoresis[8], inkjet printing[9], and slip stick evaporation[10], all of which have lower carrier mobility compared to that of CVD-based devices, but higher carrier mobility than organic FET devices[11]. Compared to the CVD-based SWNT devices, SWNT devices that are fabricated via solution casting have an advantage to separate metallic and semiconducting SWNTs on a large scale, since the purification method can be conducted in a SWNT solution, i.e., density gradient ultracentrifugation[12].

There are three advantages in constructing short-channel SWNT devices using bottom contact technique. First, the SWNTs will not be damaged by electron irradiation[13] during electron beam lithography (EBL) process because the SWNTs will be deposited after electrodes fabrication. Furthermore, there are subsequent lift off and cleaning procedure following EBL process which may degrade the quality of the SWNTs. Second, the SWNTs have direct contact with the desired metal electrodes. When using silicon wafer as a substrate, a metal buffer layer must be deposited prior to the designated metal deposition, i.e., Cr/Au or Ti/Au. In top contact devices, the SWNTs will then make contact with that of the buffer layer. Every metal has its own work function that can provide different electrical characteristics in the metal junctions of semiconducting SWNTs[14]. Third, the SWNTs can be functionalized before or after deposition. Functionalization of the SWNTs enhance the selectivity and sensitivity of SWNT-based sensing devices.[15–17] In addition, ambiguous response of the SWNT-based sensing devices produce by SWNTs random network can be eliminated by the use of short channel devices which provide SWNTs direct junctions[7].

SWNT-metal contact point is important for the transport properties considering the carrier type of the SWNT-FET devices.[2] However, the SWNT shall be bent at that contact point in bottom contact electrodes leading to a different characteristic of the devices. Hence, fabrication of flattened electrodes, which provide no height difference between metal electrodes and the substrate to prevent the bending of the SWNT, are highly expected.

In this chapter, flattened electrodes with small height difference between electrodes and insulating substrate were fabricated and compared to non-flattened electrodes in bottom contact SWNT-FET devices that consist multiple junctions of individual SWNTs. It is shown that the number of SWNT direct junctions increases as the channel length decreases when using flattened electrodes devices, which will be

useful to improve the performance of SWNT-based sensing devices[15–17] and to develop stochastic resonance devices[18,19]. The FET characteristics of these devices show an ambipolar FET behavior, and the flattened-electrode devices have better ambipolarity.

3.2 Experimental method[20]

Flattened-electrode devices were fabricated on a 300 nm SiO_2 surface grown on a heavily n-doped silicon substrate, which was treated as gate electrodes. S/D electrodes were patterned via EBL. Subsequently, reactive ion etching was performed to reduce the SiO_2 thickness of the patterned area of the substrate so that the S/D electrodes can be embedded into the substrates. Then, 8 nm Cr and 42 nm Au were deposited via electron beam deposition onto the substrates. After lift-off and a cleaning process, the metal electrodes were flattened by using a method that was described in a previous report[21]. For a comparison with the flattened-electrode SWNT FET devices, non-flattened electrode devices were also fabricated by using the same fabrication method, but excluding the reactive ion etching and flattening process.

Semiconducting SWNTs were deposited using the spin coating method[7]. 99%-semiconducting arc-discharge SWNTs (NanoIntegris, Inc.) having an average diameter of 1.4 nm were dispersed in dimethylformamide (DMF). The concentration of the SWNTs was about 10 μg/ml. The substrates were cleaned by using piranha solution and modified by using 1% 3-aminopropyltriethoxysilane (APTES, Sigma-Aldrich) in toluene for 1 hour under a N_2 atmosphere prior to the SWNT deposition. Then, 100 μl of the SWNT dispersion was dropped onto the spinning substrates. In this way, the alignment of the SWNT on the electrodes can be controlled by adjusting the position of the electrodes relative to the rotational center of the spinning

substrate. After SWNT deposition, the substrates were heated at 150 °C inside a vacuum oven for 1 hour to remove the residual solvent. The FET characteristics of all devices were measured by using the Keithley 4200 semiconductor characterization system at room temperature under vacuum conditions.

3.3 Results and discussion

Fig. 3.1 shows atomic force microscope (AFM) (SPA 400, SII Inc.) images of the SWNT junctions between the S/D electrodes at different channel lengths (0.2, 0.5, 1, and 10 μm). The average height of the flattened and non-flattened electrodes from the SiO_2 are approximately 4 and 42 nm, respectively. SWNTs can form networks or junctions between S/D electrodes due to a strong attractive interaction between the APTES-modified SiO_2 surface and the SWNTs. In addition, drop casting of the SWNTs solution onto the spinning APTES-modified SiO_2 substrates can separate semiconducting and metallic SWNTs, which is a favorable process in this research[7]. For the short channel-length devices (0.2, 0.5, and 1 μm), the SWNTs tended to create direct junctions between the S/D electrodes, which are shown in Figs. 3.1(a)–3.1(g). For the long channel-length devices (10 μm), the SWNTs formed a percolation network and there is no significant difference of the SWNT network between the flattened (Fig. 3.1(d)) and non-flattened (Fig. 3.1(h)) electrode devices.

Qualitatively, by observing the AFM images in Fig. 3.1, a larger number of SWNT direct junctions are found in the flattened-electrode devices. In order to make a quantitative comparison between the flattened and non-flattened electrode devices, the number of SWNT direct junctions between the S/D electrodes was counted by using the AFM images, which were taken prior to the electrical characterization. Five AFM images, each with a 2×2 μm area and consisted of S/D electrodes, were
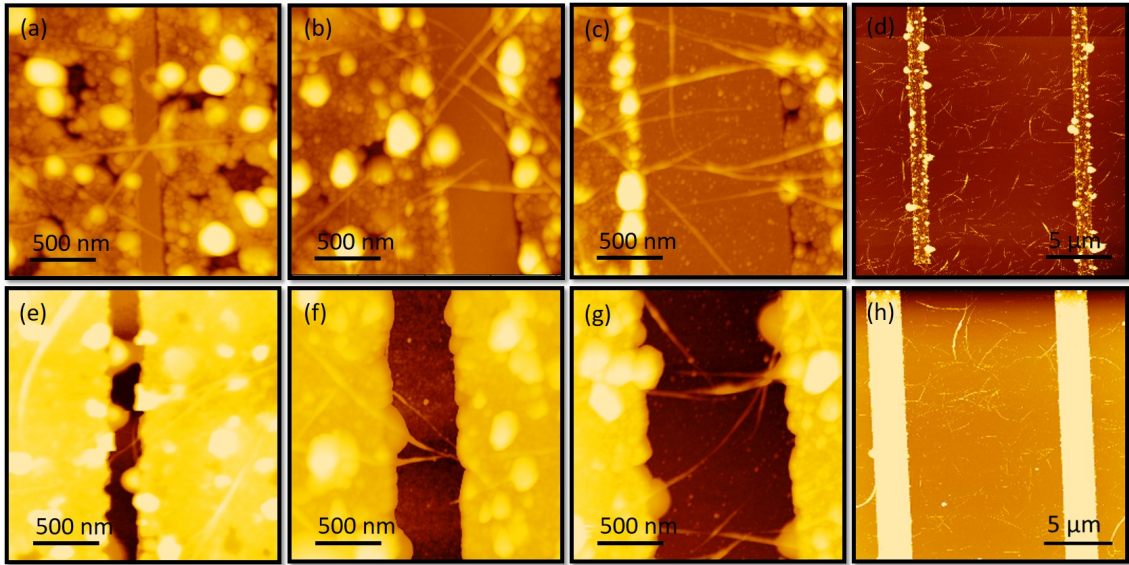
Figure 3.1: AFM images of the individual SWNT junctions between the electrodes at different channel lengths: (a) and (e) are 0.2 μm, (b) and (f) are 0.5 μm, (c) and (g) are 1 μm, and (d) and (h) are 10 μm. The channel width is 20 μm. Left and right images are flattened and non-flattened electrodes, respectively. This image was taken from Ref. [20].

randomly taken at different locations on the same sample. Table 3.1 lists the average number of SWNT direct junctions per 2-μm channel width.

The number of SWNT direct junctions in the flattened-electrode device is higher than that of the non-flattened electrode device for every channel length. As mentioned earlier, the SWNTs can be deposited by using a spin coating method due to the strong attractive interaction between the semiconducting SWNTs and APTES-modified SiO_2 surface. Thus, the number of SWNT direct junctions strongly depends on the interaction area between the SWNTs and SiO_2 surface. The results agree well with this condition. Nevertheless, the flattened-electrode devices with a channel length of 1 μm have the smallest number of SWNT direct junctions (3.4 $\pm$ 1.5 junctions per 2 μm). One possible reason for this is the average length of the SWNT sample, which was only 1 μm. Therefore, the number of SWNT direct junctions with the 0.5 μm channel length is 1.35 times larger than that of the devices with a 1 μm channel length. Thus, the decreased number of SWNT direct junctions

35

Table 3.1: Average number of SWNT direct junctions in the short channel-length SWNT FET devices per 2-μm channel width. This data was taken from Ref. [20].

Channel length	Flattened electrode	Non-flattened electrode
0.2 μm	3.8±1	1.8±1.5
0.5 μm	4.6±2	2.8±1
1 μm	3.4±1.5	3±1

with the channel length of 0.2 μm might be attributed to a decreasing channel area to catch the SWNTs.

For the non-flattened electrode SWNT-FET devices, the number of SWNT direct junctions decreased as the channel length decreased. Since the height of the electrodes was approximately 42 nm, the SWNTs may have been blocked by the wall of electrodes before reaching the area between the S/D electrodes. Furthermore, the lower interaction area between the SWNTs, which was suspended between the S/D electrodes, and the APTES-modified SiO_2 surface reduces the probability of a SWNT junction formation between the S/D electrodes.

The FET characteristics of the flattened and non-flattened electrode SWNT-FET devices were measured for the short and long channel-length devices. For the short channel-length devices (0.2, 0.5, and 1 μm), the channel mobility of the devices were calculated using the following formula:

$$\mu = (L_c/C_g V_d))(dI_d/dV_g) \tag{3.1}$$

where L_c, C_g, V_d, I_d, and V_g are the channel length, capacitance per unit length, drain voltage, drain current, and gate voltage, respectively. Instead of using the parallel plate model, C_g is provided by $C_g = 2\pi\epsilon\epsilon_0/ln(4t_{ox}/d)$, where ϵ, t_{ox}, and d are the dielectric factor and thickness of the SiO_2, and diameter of the SWNT, respectively.[22] Since those devices have multiple SWNTs junctions, the mobility value were divided by the number of SWNTs junctions (n_{SWNT}).
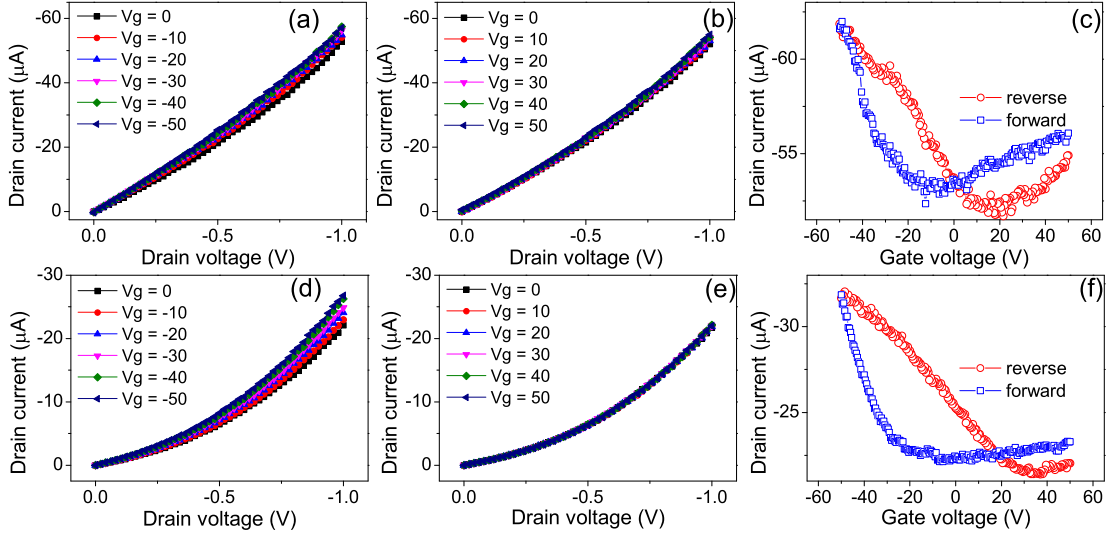
Figure 3.2: FET output and transfer characteristics of the SWNT-FET devices with a channel length of 0.2 μm. (a) and (b) are the p-channel and n-channel FET output characteristics of the SWNTs deposited on the flattened electrodes, respectively. (d) and (e) are the p-channel and n-channel FET output characteristics of the SWNTs deposited on the non-flattened electrodes, respectively. (c) and (f) are the FET transfer characteristics of the SWNTs deposited on the flattened and non-flattened electrodes at a V_D of 1 V, respectively. This image was taken from Ref. [20].

Figs. 3.2, 3.3, 3.4, and 3.5 shows the FET output and transfer characteristics of the SWNT devices with a channel length of 0.2 μm, 0.5 μm, 1 μm, and 10 μm, respectively, while under the vacuum condition. The top and bottom images show the FET characteristics of the flattened and non-flattened electrode SWNT-FET devices, respectively. FET characteristic measurements show that both devices have an ambipolar FET behavior. Using $L_c = 1$ μm, $d = 1.4$ nm, and n_{SWNT} as shown in Table 3.1, the hole and electron FET mobility of the non-flattened electrode SWNT-FET device with channel length of 1 μm are 2.13 and 0.59 cm^2/Vs, respectively. The ratio of the hole to electron mobility is 3.6. The on/off ratios for the hole and electron mobility are 25 and 8, respectively. For the flattened electrode device one, the hole and electron mobility are 0.56 and 0.27 cm^2/Vs, respectively. The ratio of the hole to electron mobility is 2.1. The on/off ratios for the hole and electron mobility are 6×10^3 and 10^3, respectively. Weak electrostatic coupling in these bottom contact devices is responsible for the low carrier mobility.

37
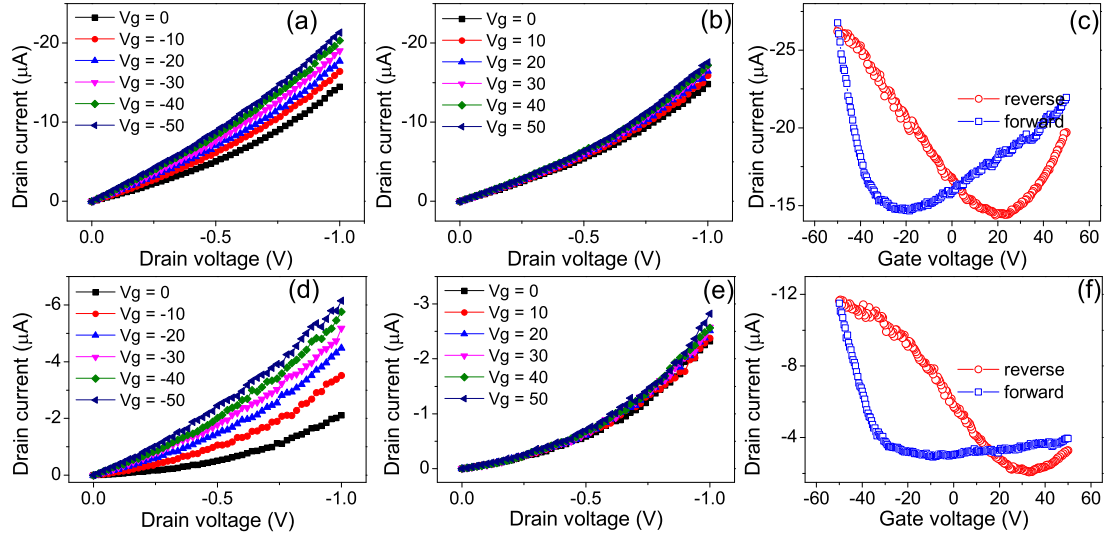
Figure 3.3: FET output and transfer characteristics of the SWNT-FET devices with a channel length of 0.5 μm. (a) and (b) are the p-channel and n-channel FET output characteristics of the SWNTs deposited on the flattened electrodes, respectively. (d) and (e) are the p-channel and n-channel FET output characteristics of the SWNTs deposited on the non-flattened electrodes, respectively. (c) and (f) are the FET transfer characteristics of the SWNTs deposited on the flattened and non-flattened electrodes at a V_D of 1 V, respectively. This image was taken from Ref. [20].
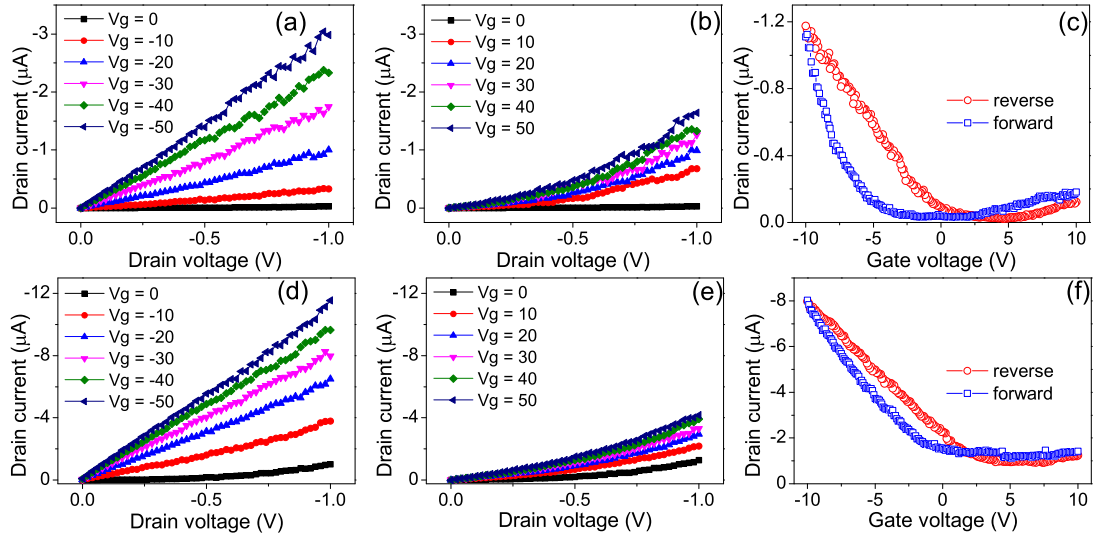
Figure 3.4: FET output and transfer characteristics of the SWNT-FET devices with a channel length of 1 μm. (a) and (b) are the p-channel and n-channel FET output characteristics of the SWNTs deposited on the flattened electrodes, respectively. (d) and (e) are the p-channel and n-channel FET output characteristics of the SWNTs deposited on the non-flattened electrodes, respectively. (c) and (f) are the FET transfer characteristics of the SWNTs deposited on the flattened and non-flattened electrodes at a V_D of 1 V, respectively. This image was taken from Ref. [20].
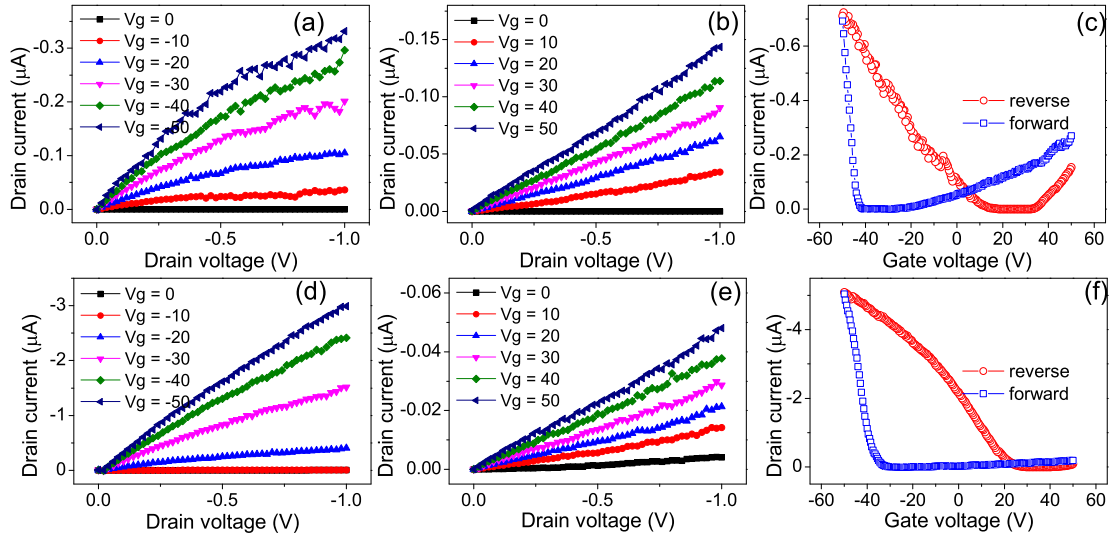
Figure 3.5: FET output and transfer characteristics of the SWNT-FET devices with a channel length of 10 μm. (a) and (b) are the p-channel and n-channel FET output characteristics of the SWNTs deposited on the flattened electrodes, respectively. (d) and (e) are the p-channel and n-channel FET output characteristics of the SWNTs deposited on the non-flattened electrodes, respectively. (c) and (f) are the FET transfer characteristics of the SWNTs deposited on the flattened and non-flattened electrodes at a V_D of 1 V, respectively. This image was taken from Ref. [20].

Next, the FET characteristics of the flattened and non-flattened electrode SWNT-FET devices in the long channel length devices were compared to each other, in which the channel length and width were 10 and 20 μm, respectively. The deposited SWNTs in the channel form an electrical network between the S/D electrodes, as shown in Figs. 3.1(d) and 3.1(h). Both devices show an ambipolar FET characteristic while under the vacuum condition. The hole and electron mobility were calculated using the following formula:

$$\mu = (L_c/(W_c C_g V_d))(dI_d/dV_g) \tag{3.2}$$

where W_c is the channel width. The capacitance (C_g) for the parallel plate model is defined by $C_g = \epsilon\epsilon_0/t_{ox}$. For the non-flattened electrode device, the hole and electron mobility are 2.95 and 0.04 cm^2/Vs, respectively. The ratio of the hole o electron mobility is 73.8. The on/off ratios of the hole and electron mobility of this

Table 3.2: Hole (μ_h) and electron (μ_e) mobility of the individual SWNT FET devices (cm^2/Vs) and their ratios (μ_h/μ_e). This data was taken from Ref. [20].

Channel length	Flattened electrode			Non-flattened electrode		
	μ_h	μ_e	ratio	μ_h	μ_e	ratio
0.2 μm	0.16±0.02	0.08±0.02	2.0	0.30±0.07	0.04±0.02	7.5
0.5 μm	0.47±0.16	0.19±0.07	2.4	0.74±0.27	0.06±0.01	12.3
1.0 μm	0.77±0.19	0.32±0.05	2.4	2.38±0.70	0.50±0.12	4.8
10 μm	0.63	0.24	2.8	2.95	0.04	73.8

device are 10^5 and 2×10^3, respectively. For the flattened-electrode device, the hole and electron mobility are 0.63 and 0.24 cm^2/Vs, respectively. The ratio of the hole to electron mobility is 73.8. The on/off ratios of the hole and electron mobility of this device are 6×10^4 and 3×10^3, respectively. A recent ambipolar SWNT-FET that was fabricated by using a SWNT random network is n-type dominant;[6] however, these ambipolar SWNT-FET devices are p-type dominant and have a better balance between their hole and electron mobility.

FET carrier mobilities on every channel length were compared to one another by averaging the hole and electron mobility from at least three working devices. The results are listed in Table 3.2. Generally, carrier mobilities tend to decrease as the channel length decreases. The FET carrier mobilities in the flattened-electrode devices are lower than those in the non-flattened electrode devices. For the 0.2- and 0.5-μm channel length devices, there is only a small difference in hole mobility between the flattened and non-flattened electrode devices. However, the electron mobility in the flattened electrodes is higher than that of the non-flattened electrodes. For the 1-μm channel length devices, the hole and electron mobility of the flattened electrode devices are lower than those of the non-flattened electrode devices (see Table 3.2).

The ratios of the hole and electron mobility of the flattened and non-flattened electrodes devices were also compared. The results are listed in Table 3.2. Ambipolarity of the SWNT-FET under vacuum condition is related to the chemical doping, metal

work function, and position of the Fermi level of the SWNT.[23] In all of the devices in this experiment, the position of the Fermi level of SWNT is the main factor of the ambipolarity, since they were measured under vacuum condition and used the same metal as electrodes. Structural deformation of the SWNT, i.e, bending, may shift the Fermi level of the SWNT. A local Raman investigation showed the changing of electronic properties of SWNT at the bending point.[24] In the case of flattened electrodes devices, Fermi level of the SWNT is located around the mid gap point of the valence and conduction band leading to a symmetric Schottky barrier (SB) for holes and electrons. While in the case of non-flattened electrodes devices, the Fermi level shift closer to the valence band due to the bending caused by a height difference between the metal electrodes and SiO_2 surfaces, in which increase SB for the electrons and decrease SB for holes. Therefore, the newly-fabricated flattened electrodes devices show better ambipolar behavior even when compared to those of previous reports[5,6].

3.4   Conclusion

In conclusion, SWNT-FET devices were fabricated using bottom contact electrodes. The results showed that the use of a flattened-electrode device increases the number of SWNT direct junctions between S/D electrodes. The balance between the hole and electron mobility in the ambipolar FET devices was increased by using the flattened electrode devices. However, the hole mobility in the flattened electrode devices was relatively lower than that of the non-flattened electrode devices. In future, improvement of the condition at the interface between the SWNTs and metal electrodes are expected, especially for an ambipolar FET devices.

References

1. Iijima, S. Helical microtubules of graphitic carbon. *Nature* **354,** 56–58 (1991).

2. Martel, R. *et al.* Ambipolar electrical transport in semiconducting single-wall carbon nanotubes. *Phys. Rev. Lett.* **87,** 256805 (2001).

3. Dürkop, T., Getty, S. A., Cobas, E. & Fuhrer, M. S. Extraordinary mobility in semiconducting carbon nanotubes. *Nano Lett.* **4,** 35–39 (2004).

4. Xu, G. *et al.* Low-frequency noise in top-gated ambipolar carbon nanotube field effect transistors. *Appl. Phys. Lett.* **92,** 223114 (2008).

5. Shiraishi, M. *et al.* Single-walled carbon nanotube aggregates for solution-processed field effect transistors. *Chem. Phys. Lett.* **394,** 110 –113 (2004).

6. Bisri, S. *et al.* High performance ambipolar field-effect transistor of random network carbon nanotubes. *Adv. Mater.* **24,** 6147–6152 (2012).

7. LeMieux, M. *et al.* Solution assembly of organized carbon nanotube networks for thin-film transistors. *ACS Nano* **3,** 4089–4097 (2009).

8. Stokes, P. & Khondaker, S. Local-gated single-walled carbon nanotube field effect transistors assembled by AC dielectrophoresis. *Nanotechnology* **19,** 175202 (2008).

9. Beecher, P. *et al.* Ink-jet printing of carbon nanotube thin film transistors. *J. Appl. Phys.* **102,** 043710 (2007).

10. Engel, M. *et al.* Thin film nanotube transistors based on self-assembled, aligned, semiconducting carbon nanotube arrays. *ACS Nano* **2,** 2445–2452 (2008).

11. Kawanishi, T. *et al.* High-mobility organic single crystal transistors with sub-micrometer channels. *Appl. Phys. Lett.* **93,** 023303 (2008).

12. Arnold, M., Green, A., Hulvat, J., Stupp, S. & Hersam, M. Sorting carbon nanotubes by electronic structure using density differentiation. *Nat. Nano.* **1,** 60–5 (2006).

13. Suzuki, S., Kanzaki, K., Homma, Y. & Fukuba, S.-y. Low-acceleration-voltage electron irradiation damage in single-walled carbon nanotubes. *Jpn. J. Appl. Phys.* **43,** L1118–L1120 (2004).

14. Avouris, P., Freitag, M. & Perebeinos, V. Carbon-nanotube photonics and optoelectronics. *Nat. Photon.* **2,** 341–350 (2008).

15. Lee, C., Sharma, R., Radadia, A., Masel, R. & Strano, M. On-chip micro gas chromatograph enabled by a noncovalently functionalized single-walled carbon nanotube sensor array. *Angew. Chem. Int. ed.* **47,** 5018–5021 (2008).

16. Kauffman, D. & Star, A. Electronically monitoring biological interactions with carbon nanotube field-effect transistors. *Chem. Soc. Rev.* **37,** 1197–1206 (2008).

17. Esser, B., Schnorr, J. & Swager, T. Selective detection of ethylene gas using carbon nanotube-based devices: utility in determination of fruit ripeness. *Angew. Chem. Int. ed.* **51,** 5752–5756 (2012).

18. Collins, J, Chow, C & Imhoff, T. Stochastic resonance without tuning. *Nature* **376,** 236–238 (1995).

19. Hakamata, Y. *et al.* Enhancement of weak-signal response based on stochastic resonance in carbon nanotube field-effect transistors. *J. Appl. Phys.* **108** (2010).

20. Setiadi, A., Akai-Kasaya, M., Saito, A. & Kuwahara, Y. Advantages of flattened electrode in bottom contact single-walled carbon nanotube field-effect transistor. *Appl. Phys. Lett.* **105,** 093506 (2014).

21. Higuchi, Y. *et al.* Application of simple mechanical polishing to fabrication of nanogap flat electrodes. *Jpn. J. Appl. Phys.* **45,** L145–L147 (2006).

22. Yang, M. H. *et al.* Advantages of top-gate, high-k dielectric carbon nanotube field-effect transistors. *Appl. Phys. Lett.* **88,** 113507 (2006).

23. Chen, Y.-F. & Fuhrer, M. S. Tuning from thermionic emission to ohmic tunnel contacts via doping in Schottky-barrier nanotube transistors. *Nano Letters* **6,** 2158–2162 (2006).

24. Okuno, Y., Saito, Y., Kawata, S. & Verma, P. Tip-enhanced Raman investigation of extremely localized semiconductor-to-metal transition of a carbon nanotube. *Phys. Rev. Lett.* **111,** 216101 (2013).

Chapter 4

Raman Spectroscopy Study on The Bending of Carbon Nanotube

4.1 Introduction

Single-walled carbon nanotubes (SWNTs)[1] have attracted considerable scientific interest owing to their unique structural and electronic properties[2]. The high mobility of semiconducting SWNTs has led to the development of SWNT-based electronic devices. For example, SWNT-based field effect transistor (FET) devices are candidate replacements for silicon-based FET devices.[3–5] SWNT devices are fabricated with either top- or bottom-contact electrodes. The advantage of bottom-contact SWNT-FET devices is that they overcome device quality problems associated with electron irradiation and residual resist during e-beam lithography and the subsequent lift-off process, respectively. It has been reported that electron irradiation at an energy of 0.525 keV can damage SWNTs.[6] In addition, residual resist can increase the noise of SWNT-FET devices.[7]

It is well known that the electronic transport of an SWNT-FET is strongly affected

by the Schottky barrier (SB) at the interfaces between the SWNT and the metal electrodes; the conductance of SWNT-FETs can be increased by narrowing the SB by adjusting the gate voltage.[8,9] In the case of top-contact SWNT devices, the SB height of the SWNT-metal contact mainly depends on the work function of the metals and other materials used as the source and drain (S/D) electrodes.[10] However, in the case of bottom-contact SWNT devices, previous report shows that the SB is also affected by the shape of the SWNT at the points of contact with the S/D electrodes.[9] Therefore, it is important to understand the effect of the interface conditions on the electronic transport of an SWNT, especially when the SWNT is deformed at the interface.

Raman spectroscopy is a powerful tool for the characterization of SWNTs.[11–15] The most distinctive Raman feature of SWNTs is a (strongly diameter-dependent) radial breathing mode (RBM) that arises due to their circular structure. Another interesting Raman mode of SWNTs is the tangential mode; the G^+ and G^- bands of this mode are assigned to longitudinal-optic (axial) and transverse-optic (circumferential) modes, respectively, in semiconducting SWNTs. For metallic SWNTs, the G^+ and G^- bands are assigned to transverse-optic (circumferential) and longitudinal-optic (axial) modes, respectively. Conduction electrons in metallic SWNTs are bound to longitudinal-optic phonons, resulting in an asymmetric lineshape of the G^- band, which can be fitted to a Breit-Wigner-Fano (BWF) lineshape. On the other hand, the G^- band of semiconducting SWNTs will have a symmetric Lorentzian lineshape, and not fit the BWF, so that semiconducting SWNTs can be distinguished by observing the G^- band.[11,15] It has also been reported that the position of the G^+ and G^- bands is related to the position of the Fermi level of the SWNT.[12,13] Changing the Fermi level of the SWNT by applying a gate voltage will cause the positions of the G^+ and G^- bands of the corresponding SWNT to shift.[12,13] Furthermore, carbon bond disorder can induce double resonance features in the Raman spectra, such as a D band, which can be used to evaluate the quality of SWNTs
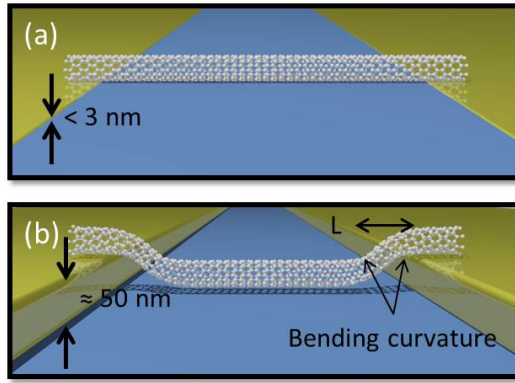
Figure 4.1: Illustrations of SWNTs deposited on (a) flattened and (b) non-flattened electrodes. L in (b) indicates the length covering two bending curvatures of SWNT. This image was taken from Ref. [19].

through calculation of the G/D ratio.[16–18]

In this chapter, the effect of SWNT deformation due to bending at the positions of contact with S/D electrodes on bottom-contact SWNT devices were investigated using Raman mapping measurements in which a laser beam spot was scanned over the sample surfaces. Figure 4.1 illustrates SWNTs deposited on (a) flattened and (b) non-flattened electrodes. The Raman spectra and FET characteristics of the SWNTs deposited on flattened and non-flattened electrode devices were compared. The results indicate that the G^+ and G^- bands positions of SWNTs are down-shifted at their bending points, indicating that the Fermi level is shifted towards the valence band. Owing to this Fermi level shift at the bending point, SWNTs on flattened and non-flattened electrodes have different FET characteristics: ambipolar and p-type, respectively.

4.2 Experimental method[19]

Flattened and non-flattened electrode devices were fabricated on heavily doped n-type silicon substrates with a 300-nm-thick SiO_2 layer. The detailed fabrication method has been described elsewhere.[9,20] In the case of flattened electrodes, the

height difference between the metal electrodes and the SiO_2 was less than 3 nm, compared to approximately 50 nm in the case of non-flattened electrodes. SWNTs were deposited on these electrodes using AC-dielectrophoresis[21,22] without any modification to the substrate surface. 20 μl of a 99% semiconducting-SWNT (NanoIntegris, Inc.) dispersion in N,N-dimethylformamide (Sigma Aldrich) with a concentration of 500 ng/ml was dropped between the S/D electrodes. To align the SWNTs between the S/D electrodes, an AC voltage of 8 Vpp at 1 MHz was applied for 3-4 s. Subsequently, the devices were blown dry, rinsed with isopropyl alcohol (Sigma Aldrich), and then blown dry again. Finally, the devices were annealed at 150°C under vacuum to remove residual solvent. It is confirmed that the SWNTs were aligned between the S/D electrodes.

Atomic force microscope (AFM) (SPA 400, SII Inc.) images were taken to verify the presence of SWNTs between the S/D electrodes prior to the Raman mapping measurements. Raman mapping experiments were performed using RAMANtouch (Nanophoton Corp.) with a 100x objective lens (numerical aperture: 0.9) and a 1200 line/mm grating. The incident laser wavelength and power were 523 nm and 5 mW, respectively, and the pixel size and spectral resolution in this configuration were 205x205 nm^2 and 0.87 cm^{-1}, respectively. Each pixel was exposed for 1 s to obtain a Raman spectrum from 1200-2000 cm^{-1}. Concerned with the spatial resolution of Raman mapping method, a few SWNT junctions were intentionally deposited between the S/D electrodes to allow correlation of the Raman spectra with individual SWNTs.

4.3   Results and discussion

Figures 4.2(a)–4.2(c) show AFM images of SWNTs deposited on flattened and non-flattened electrodes. Based on the line profile of the AFM images which were shown
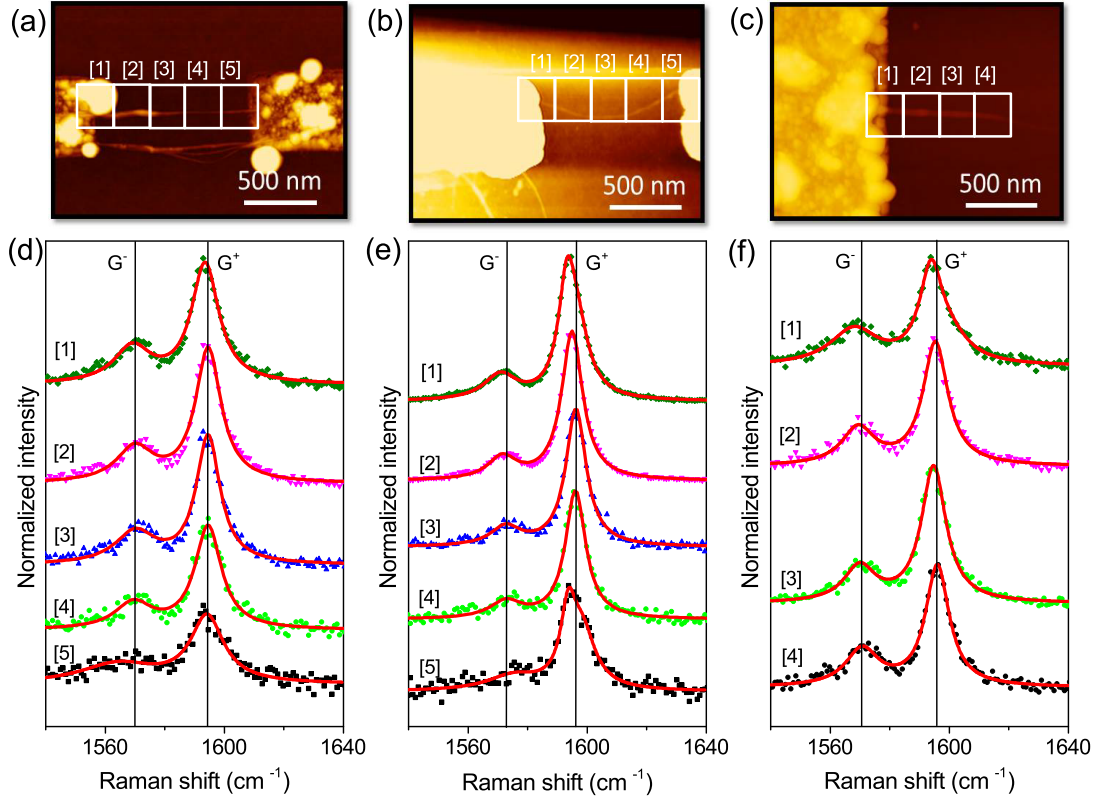
Figure 4.2: AFM images of SWNTs on flattened (a) and non-flattened (b and c) electrodes and their respective Raman spectra around G band peaks. (a) and (b) show isolated single SWNTs, while (c) shows bundled SWNTs. The height difference between the SiO_2 surface and the metal electrodes in (a) was less than 3 nm, compared to approximately 50 nm in (b) and (c). Raman spectra in (d), (e), and (f) corresponds to the SWNTs in (a), (b), and (c), respectively. Position 1 and 5 in (d), (e), and (f) are the positions at which the SWNTs contact the electrodes, while 2, 3, and 4 are the positions of the SWNT on SiO_2 surface. Vertical solid lines are visual guide to see the shift of the G^+ and G^- band peaks. This image was taken from Ref. [19].

in Fig. 4.3, the SWNTs in Figs. 4.2(a) and 4.2(b) are individual one, while bundled one in Fig. 4.2(c). The Raman spectra of the corresponding SWNTs are shown in Figs. 4.2(d)–4.2(f) for the SWNTs in Figs. 4.2(a)–4.2(c), respectively. The position dependence of Raman spectra of the corresponding SWNTs around G band peaks are shown in Figs. 4.2(d)–4.2(f) for the SWNT in Figs. 4.2(a)–4.2(c), respectively. Hereafter, the SWNTs shown in Figs. 4.2(a)–4.2(c) were denoted as SWNT-1, SWNT-2, and SWNT-3, respectively.

Because there were only a few SWNTs inside the laser beam spot, it was difficult

48
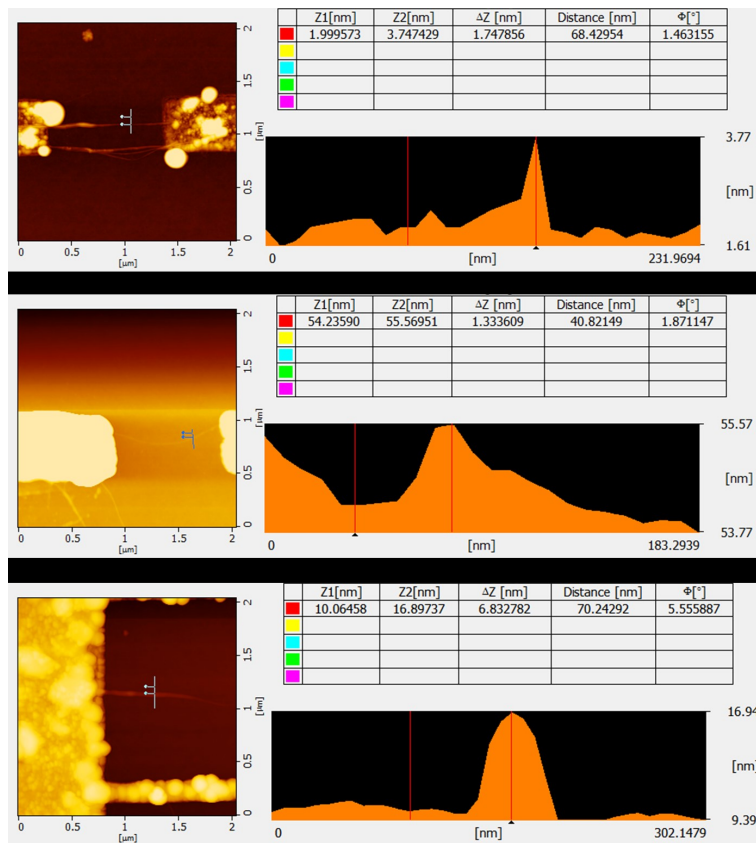
Figure 4.3: Top, middle, and bottom images show the line profile of the AFM images of Fig. 4.2(a), 4.2(b), and 4.2(c), respectively. This image was taken from Ref. [19].

49

to observe the RBM modes ($\sim$100–300 cm^{-1}) in the Raman spectra, but the D and G bands of the SWNTs were successfully observed. However, the D band peak intensity was extremely low. Here, the research is focused on the elucidation of the G band of the SWNTs. Both the G$^+$ and G$^-$ bands of the SWNTs in all of the devices were fitted by a Lorentzian function. None of the G$^-$ bands exhibit a BWF lineshape that would have indicated the presence of metallic SWNTs.[11,15] Therefore, all of the SWNTs in Figs. 4.2(a)–4.2(c) were semiconducting.

From the fitting of the Raman spectra, the peak positions of the G$^+$ and G$^-$ band of the SWNTs were extracted, and are listed in Table 4.1. ω_1^+ (ω_1^-) and ω_5^+ (ω_5^-) are the G$^+$ (G$^-$) band peak of the SWNTs at the contact points with the electrodes, while ω_2^+ (ω_2^-), ω_3^+ (ω_3^-), and ω_4^+ (ω_4^-) are the G$^+$ (G$^-$) band peak of the SWNTs on SiO$_2$ surface as shown in Figs. 4.2. The G$^-$ band peak of SWNT-1 and SWNT-2 at position [5] in Figs. 4.2(d) and 4.2(e) were omitted because the peak intensity are very low and thus difficult to be fitted accurately. The difference in the G$^+$ (G$^-$) band peak position between the SWNTs on SiO$_2$ surface and at contact points with the electrodes is denoted as $\Delta\omega^+$ ($\Delta\omega^-$). The $\Delta\omega^+$ ($\Delta\omega^-$) in SWNT-1 of 0.33$\pm$0.05 (0.43$\pm$0.31) cm^{-1} is smaller than the spectral resolution of 0.87 cm^{-1}. On the other hand, the $\Delta\omega^+$ ($\Delta\omega^-$) of SWNT-2 and SWNT-3 are 2.33$\pm$0.26 (1.80$\pm$0.70) and 1.43$\pm$0.29 (2.00$\pm$0.66) cm^{-1}, respectively, which are both larger than the spectral resolution of 0.87 cm^{-1}. Thus, a meaningful down-shift of the G$^+$ and G$^-$ band frequency in SWNT-2 and SWNT-3 were clearly observed. In addition, the bending length, shown in Fig. 4.1 (b) as L, was estimated to be 110 nm. Hence, 54% of the SWNT length was covered by the laser beam spot, ensuring a strong contribution to the Raman spectra.

It has been reported that the positions of the G band modes of SWNTs are related to their doping, as electrochemical doping using a gate voltage could change the Fermi level, and the variation of the G band as a function of gate voltage was also

Table 4.1: Frequency (ω^+ (ω^-))(cm^{-1}) of the position dependence G$^+$ (G$^-$) band of the SWNTs shown in Figs. 4.2(a)–4.2(c). $\Delta\omega^+$ ($\Delta\omega^-$) is frequency difference of G$^+$ (G$^-$) band peak of the SWNTs on SiO$_2$ surface (ω_2^+ (ω_2^-), ω_3^+ (ω_3^-), and ω_4^+ (ω_4^-)) and SWNTs at the contact points with the electrodes (ω_1^+ (ω_1^-) and ω_5^+ (ω_5^-)). This data was taken from Ref. [19].

Sample	ω_1^+ (ω_1^-)	ω_2^+ (ω_2^-)	ω_3^+ (ω_3^-)	ω_4^+ (ω_4^-)	ω_5^+ (ω_5^-)	$\Delta\omega^+$ ($\Delta\omega^-$)
SWNT-1	1594.2	1594.6	1594.5	1594.5	1594.2	0.33±0.05
	(1569.4)	(1569.9)	(1570.1)	(1569.5)	(-)	(0.43±0.31)
SWNT-2	1594.1	1596.2	1596.4	1596.1	1592.7	2.33±0.26
	(1570.5)	(1571.5)	(1572.6)	(1572.8)	(-)	(1.80±0.70)
SWNT-3	1593.7	1595.5	1594.8	1595.3	-	1.43±0.29
	(1568.0)	(1569.4)	(1569.9)	(1570.7)	(-)	(2.00±0.66)

shown.[12,13] Furthermore, theoretical calculations indicated that charge doping could change the bond length of graphene.[23] Therefore, it is assumed that changes in the C-C bond lengths, without C-C bond breaking or sp^2-sp^3 transition of the C-C bond, due to deformation could have led to a doping-like effect in SWNT-2 and SWNT-3. In addition, it has been predicted theoretically that strain-induced changes in C-C bond length will result in marked changes in the electronic properties of SWNTs.[24] Since there is no significant change in the D band intensity in any of this experiments, there is presumably no structural defect at the SWNT bending point, only a change in C-C bond length. Moreover, the bending curvature of SWNT was estimated to be 1.17×10^{-2} rad/nm which is lower than the critical curvature to form kinked SWNT.[25] It is also noted that there was no applied gate or drain voltage during the Raman mapping measurements. Therefore, the shifts of the G band position in SWNT-2 and SWNT-3 can be ascribed to a doping-like effect arising from changes in the lattice parameters within the bent areas of the SWNTs.

Another effect of the SWNT bending was the appearance of an additional peak near the G$^+$ band. Figs. 4.4(a), 4.4(b), and 4.4(c) show the fitting of Raman spectra of SWNT-1, SWNT-2, and SWNT-3, respectively, at position [1] and [3]. It is clear that there is additional peak near the G$^+$ band at the bending point of SWNT-2 and SWNT-3 (position [1]), while no additional peak can be fitted for SWNT-1 at
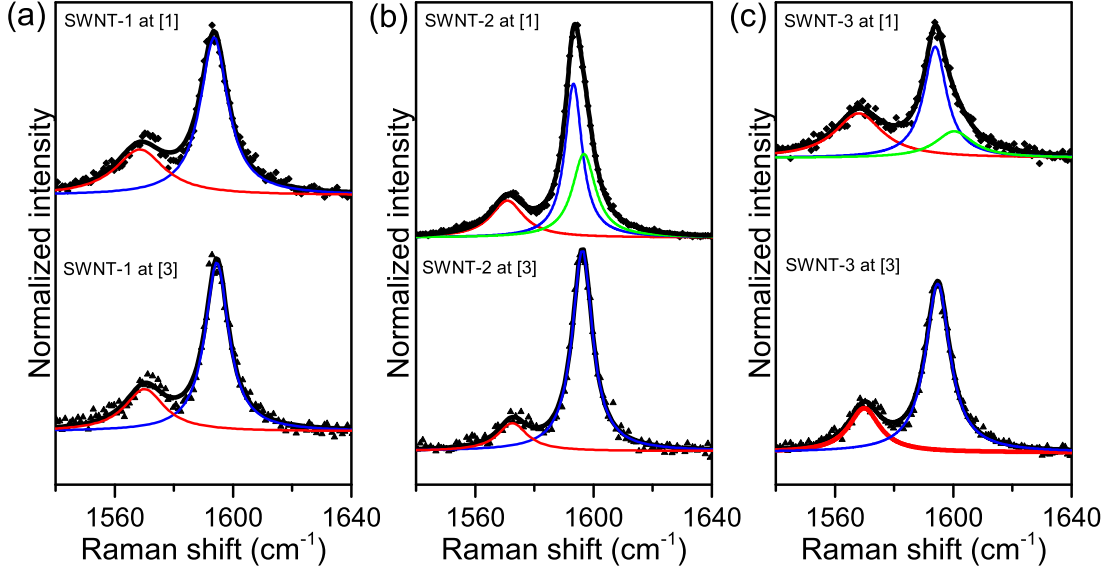
Figure 4.4: Fitting of Raman spectra of (a) SWNT-1 at position [1] and [3], (b) SWNT-2 at position [1] and [3], and (c) SWNT-3 at position [1] and [3]. The additional peak near the G$^+$ band appears at the bending point of the SWNT (SWNT-2 and SWNT-3 at position [1]).

position [1]. This peak is attributed to a curving effect along the tube direction. The appearance of the additional peak is in good agreement with previous Raman spectral observations of ring-shaped carbon nanotubes[14].

In order to confirm the Fermi-level shifting of SWNTs, the SWNT-FET devices were fabricated with the increased of channel width to 20 μm, and the channel length was varied from 0.5–1.0 μm to obtain sufficient S/D current. AFM images confirmed that there were more than ten SWNT junctions per SWNT-FET device. The FET characteristics of flattened- and non-flattened-electrode SWNT-FET devices were then measured under vacuum and evaluated the hole and electron mobilities using following formula:

$$\mu = (L_c/C_g V_d)(dI_d/dV_g) \tag{4.1}$$

where L_c, C_g, and V_d are the channel length, capacitance per unit length, and drain voltage, respectively. C_g was provided by $C_g = 2\pi\epsilon\epsilon_0/ln(4t_{ox}/d)$, where ϵ, ϵ_0, t_{ox}, and d are the relative permittivity, vacuum permittivity, thickness of the SiO$_2$, and the

SWNT diameter, respectively.[26] Because multiple SWNT junctions were observed, the mobility value was divided by the number of SWNT junctions n_{SWNT}, which was estimated by counting the SWNT junctions in the AFM images.

FET output and transfer characteristic of SWNT-FET devices fabricated on flattened and non-flattened electrodes with channel lengths of 0.5 and 1.0 μm are shown in Fig. 4.5, from which the hole and electron mobilities were evaluated. The flattened electrode SWNT devices clearly showed ambipolar characteristics, whereas p-type characteristics were observed for the non-flattened electrode devices. The hole and electron mobilities of a flattened electrode device with a 0.5 μm channel length were 1.18 and 0.46 cm^2/Vs, respectively, while those of a flattened electrode device with a 1.0 μm channel length were 2.56 and 1.69 cm^2/Vs, respectively. On the other hand, the hole mobilities of non-flattened electrode devices with channel lengths of 0.5 and 1.0 μm were 2.27 and 1.36 cm^2/Vs, respectively. The ratio between hole and electron mobilities of the SWNT-FET devices which were fabricated on flattened electrodes with channel length of 0.5 and 1.0 μm are 2.6 and 1.5, respectively, which are better than previous reports[27,28]. It is considered that the water molecules on SiO$_2$ surface responsible for the hysteresis of CNT-FET devices. Since there are similar hysteresis of the FET transfer-characteristic in both flattened and non-flattened electrodes devices, it is concluded that the origin of the FET-characteristic is the shape of the SWNT at the contact point to the metal electrodes.

The FET measurements clearly reveal that the FET characteristics of SWNT-FET devices depend strongly on the deformation of the SWNTs at the interface. This is consistent to the previous work[9] with SWNT-FET devices prepared by spin coating, in which SWNT-FET devices fabricated on flattened electrodes showed improved ambipolarity. It is known that deforming an SWNT will change its electronic properties.[9,29,30] Moreover, the FET transfer characteristics of an SWNT-FET device
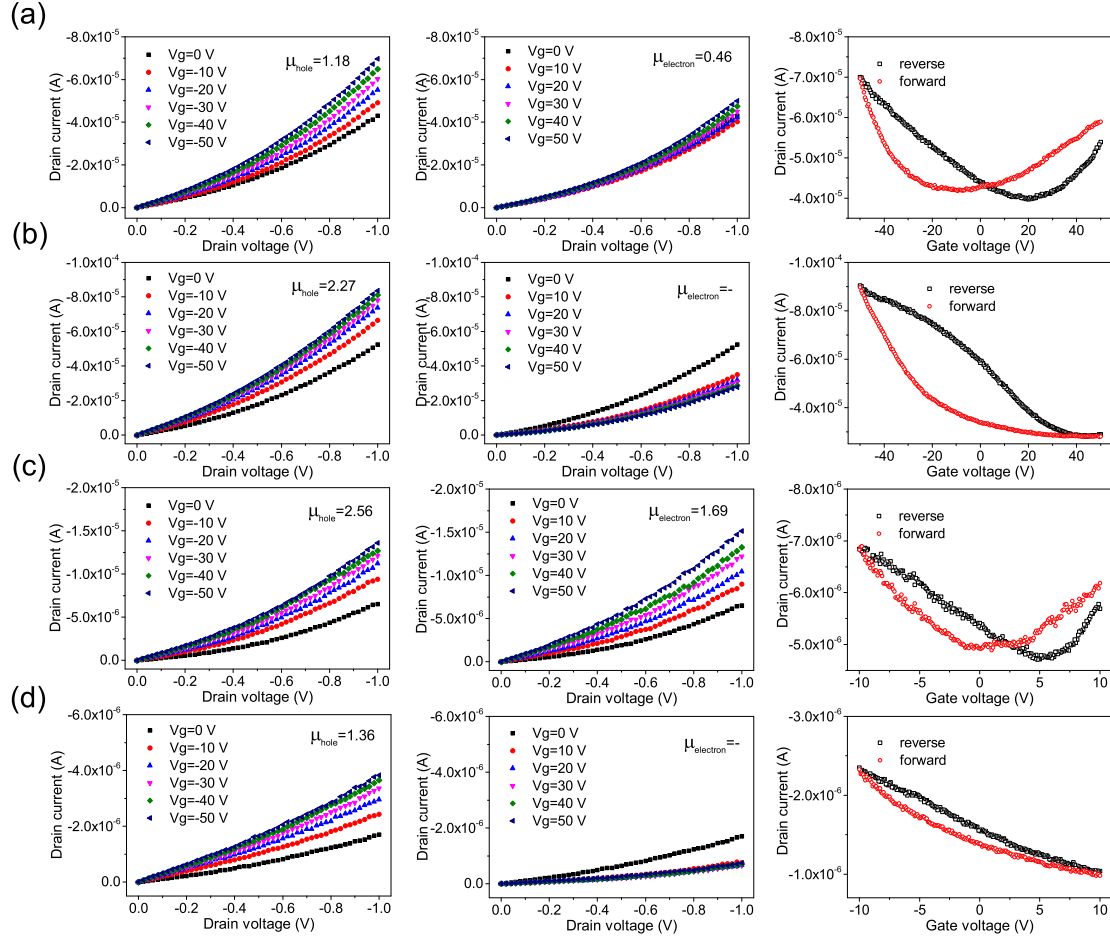
Figure 4.5: FET output and transfer characteristics of the SWNT-FET devices fabricated on flattened (a) and (c) and non-flattened (b) and (d) electrodes with a channel length of 0.5 and 1.0 m, respectively. The left, center, and right images are p-channel output characteristic, n-channel output characteristic, and FET transfer characteristic at VD of 1 V, respectively. Hole (μ_{hole}) and electron ($\mu_{electron}$) mobility values are written in the corresponding figure. The unit of mobility is cm^2/Vs. This image was taken from Ref. [19]. This image was taken from Ref. [19].
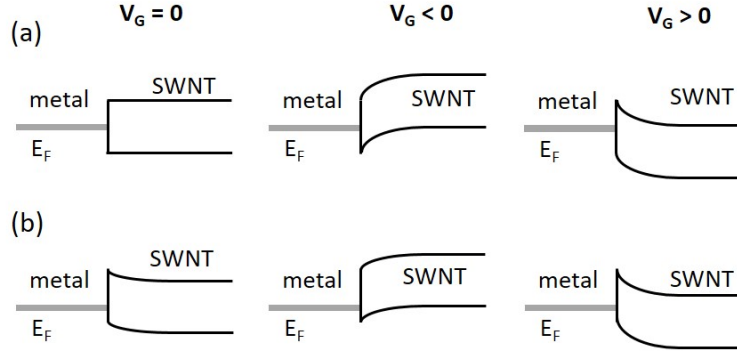
Figure 4.6: (a) and (b) are band diagrams of SWNT-FET devices fabricated on flattened and non-flattened electrodes, respectively. The left, center, and right images in (a) and (b) are the band diagrams at zero, negative, and positive gate voltages, respectively. This image was taken from Ref. [19].

depend on the chemical doping, the metal work function at the interface, and the Fermi level of the SWNT.[8] The ambipolarity of SWNT devices without chemical doping strongly depends on the Fermi level of the SWNTs.[8,9] A shift in the Fermi level changes the SB at the interface between the SWNT and the metal electrodes, which in turn changes the electronic transport properties of the SWNT. Figs. 4.6(a) and 4.6(b) show the band diagram of SWNT-FET devices fabricated on flattened and non-flattened electrodes, respectively. In the case of flattened-electrode devices, it is assumed that the SWNT has the same SB for holes and electrons, leading to ambipolar FET characteristics. On the other hand, the Fermi level of the SWNT approaches the valence band, which is caused by bending of the SWNT in the case of non-flattened-electrode devices. In this case, the SB for holes (electrons) decreased (increased), in which holes can be injected into the SWNT at a negative gate voltage, while electrons cannot be injected at a positive gate voltage, owing to the large SB at the metal-SWNT interface. Therefore, the bending of SWNTs in samples SWNT-2 and SWNT-3 decreased the Fermi level of the SWNTs at their bending points towards the valence band, resulting in p-type characteristics.

4.4 Conclusion

In conclusion, this research demonstrated the bending of SWNTs due to the height difference between metal electrodes and an underlying SiO_2 surface. For non-flattened-electrode devices, the bending of the SWNTs lowered their G^+ and G^- bands frequency and decreased their Fermi level. The flattened electrode, on the contrary, maintained the original shape of the SWNTs, and no shifting of the G^+ and G^- bands was observed. Ambipolar FET characteristics has been observed in the flattened-electrode devices, but only p-type characteristics were obtained in the non-flattened-electrode devices. The bending of the SWNTs decreased their Fermi level at the bending point, resulting in a down-shift of the G^+ and G^- bands and a transition from ambipolar to p-type characteristics. Further study, such as high spatial resolution measurements, is necessary to clarify the relationship between the Raman spectrum and the local electronic structure of an SWNT at the bending point. Tip-enhanced Raman spectroscopy, which can be used to obtain Raman spectra at only the bending point of an SWNT using an AFM[15] or scanning tunneling microscope[31], is a promising method of elucidating nanoscale bending effects.

References

1. Iijima, S. Helical microtubules of graphitic carbon. *Nature* **354,** 56–58 (1991).

2. Wildöer, J. W., Venema, L. C., Rinzler, A. G., Smalley, R. E. & Dekker, C. Electronic structure of atomically resolved carbon nanotubes. *Nature* **391,** 59–62 (1998).

3. Martel, R. *et al.* Ambipolar electrical transport in semiconducting single-wall carbon nanotubes. *Phys. Rev. Lett.* **87,** 256805 (2001).

4. Dürkop, T., Getty, S. A., Cobas, E. & Fuhrer, M. S. Extraordinary mobility in semiconducting carbon nanotubes. *Nano Lett.* **4,** 35–39 (2004).

5. Franklin, A. *et al.* Sub-10 nm carbon nanotube transistor. *Nano Lett.* **12,** 758–762 (2012).

6. Suzuki, S., Kanzaki, K., Homma, Y. & Fukuba, S.-y. Low-acceleration-voltage electron irradiation damage in single-walled carbon nanotubes. *Jpn. J. Appl. Phys.* **43,** L1118–L1120 (2004).

7. Sharf, T., Kevek, J. W., Deborde, T., Wardini, J. L. & Minot, E. D. Origins of charge noise in carbon nanotube field-effect transistor biosensors. *Nano lett.* **12,** 6380–6384 (2012).

8. Chen, Y.-F. & Fuhrer, M. S. Tuning from thermionic emission to ohmic tunnel contacts via doping in Schottky-barrier nanotube transistors. *Nano Letters* **6,** 2158–2162 (2006).

9. Setiadi, A., Akai-Kasaya, M., Saito, A. & Kuwahara, Y. Advantages of flattened electrode in bottom contact single-walled carbon nanotube field-effect transistor. *Appl. Phys. Lett.* **105,** 093506 (2014).

10. Avouris, P., Freitag, M. & Perebeinos, V. Carbon-nanotube photonics and optoelectronics. *Nat. Photon.* **2,** 341–350 (2008).

11. Dresselhaus, M., Dresselhaus, G., Jorio, A., Filho, A. & Saito, R. Raman spectroscopy on isolated single wall carbon nanotubes. *Carbon* **40,** 2043–2061 (2002).

12. Das, A. & Sood, A. Renormalization of the phonon spectrum in semiconducting single-walled carbon nanotubes studied by Raman spectroscopy. *Phys. Rev. B* **79,** 235429 (2009).

13. Park, J. *et al.* Fermi energy dependence of the G-band resonance Raman spectra of single-wall carbon nanotubes. *Phys. Rev. B* **80,** 081402(R) (2009).

14. Ren, Y. *et al.* Additional curvature-induced Raman splitting in carbon nanotube ring structures. *Phys. Rev. B* **80,** 113412 (2009).

15. Okuno, Y., Saito, Y., Kawata, S. & Verma, P. Tip-enhanced Raman investigation of extremely localized semiconductor-to-metal transition of a carbon nanotube. *Phys. Rev. Lett.* **111,** 216101 (2013).

16. Itkis, M. E., Perea, D. E., Jung, R., Niyogi, S. & Haddon, R. C. Comparison of analytical techniques for purity evaluation of single-walled carbon nanotubes. *J. Am. Chem. Soc.* **127,** 3439–3448 (2005).

17. Pimenta, M. A. *et al.* Studying disorder in graphite-based systems by Raman spectroscopy. *Phys. Chem. Chem. Phys.* **9,** 1276–1290 (2007).

18. Chen, G. *et al.* Absence of an ideal single-walled carbon nanotube forest structure for thermal and electrical conductivities. *ACS Nano* **7,** 10218–10224 (2013).

19. Setiadi, A., Akai-Kasaya, M. & Kuwahara, Y. Raman mapping investigation of single-walled carbon nanotube bending in bottom-contact field-effect-transistor devices. *J. Appl. Phys.* **120,** 094302 (2016).

20. Higuchi, Y. *et al.* Application of simple mechanical polishing to fabrication of nanogap flat electrodes. *Jpn. J. Appl. Phys.* **45,** L145–L147 (2006).

21. Krupke, R., Hennrich, F., Weber, H., Kappes, M. & Löhneysen, H. Simultaneous deposition of metallic bundles of single-walled carbon nanotubes using AC-dielectrophoresis. *Nano Lett.* **3,** 1019–1023 (2003).

22. Stokes, P. & Khondaker, S. Local-gated single-walled carbon nanotube field effect transistors assembled by AC dielectrophoresis. *Nanotechnology* **19,** 175202 (2008).

23. Lazzeri, M. & Mauri, F. Nonadiabatic Kohn anomaly in a doped graphene monolayer. *Phys. Rev. Lett.* **97,** 266407 (2006).

24. Shtogun, Y. V. & Woods, L. M. Electronic and magnetic properties of deformed and defective single wall carbon nanotubes. *Carbon* **47,** 3252–3262 (2009).

25. Iijima, S., Brabec, C., Maiti, A. & Bernholc, J. Structural flexibility of carbon nanotubes. *J. Chem. Phys.* **104,** 2089–2092 (1996).

26. Yang, M. H. *et al.* Advantages of top-gate, high-k dielectric carbon nanotube field-effect transistors. *Appl. Phys. Lett.* **88,** 113507 (2006).

27. Shiraishi, M. *et al.* Single-walled carbon nanotube aggregates for solution-processed field effect transistors. *Chem. Phys. Lett.* **394,** 110 –113 (2004).

28. Bisri, S. *et al.* High performance ambipolar field-effect transistor of random network carbon nanotubes. *Adv. Mater.* **24,** 6147–6152 (2012).

29. Minot, E. D. *et al.* Tuning Carbon Nanotube Band Gaps with Strain. *Phys. Rev. Lett.* **90,** 156401 (2003).

30. Shan, B, Lakatos, G., Peng, S & Cho, K. First-principles study of band-gap change in deformed nanotubes. *Appl. Phys. Lett.* **87,** 173109 (2005).

31. Chaunchaiyakul, S. *et al.* Nanoscale analysis of multiwalled carbon nanotube by tip-enhanced Raman spectroscopy. *Carbon* **99,** 642–648 (2016).

Chapter 5

Elucidation of Random Telegraph Signal in Carbon Nanotube Devices with Adsorbed Molecules

5.1 Introduction

Low-frequency noise arises in a wide variety of systems of both artificial and natural objects, such as electronics, radio signals, climates, and bio-creatures. Serious attempts are made to eliminate noise in electronics because noise hampers device operation and signal transmission. However, noise is cleverly used in natural stochastic systems, such as computation in the human brain[1–3] and signal detection in living creatures[4–6]. Numerous discussions and studies on noise in nano-material electronics have begun to elucidate the origin and mechanisms of noise at the atomic[7–14] and single-molecule level[15,16]. Recently, the use of noise in nano-electronics has been proposed for a chemical bonding prober[16], the Johnson noise thermometer[17], and bio-[18–20] and chemical-sensing[21–26] systems, as well as for theoretical prediction of molecular identification[27] because noise can provide information about the physical

and chemical properties of molecules that influence the nanomaterial medium.

Low-dimensional nanomaterials, such as semiconducting nanowires[28], carbon nanotubes (CNTs)[29], graphene[30], and atomically thin MoS_2[31], which have high surface-to-volume ratios, are very good candidates with high sensitivity for detecting noise signals based on surface perturbations. Similar to conventional semiconductor devices, such as Si complementary metal-oxide-semiconductor (CMOS) field-effect transistors (FETs)[32,33], low-dimensional nanomaterial electronic devices have various types of intrinsic noise. Low-frequency noise in electronics is generally composed of three components[34]: thermal noise, generation-recombination (GR) noise, and flicker noise ($1/f$ noise). Thermal noise has its origin in the random motion of charge carriers and is referred to as white noise because its spectral density does not depend on frequency. Generation-recombination noise is based on a single fluctuation event between two states, such as excitation and relaxation or charge trapping and detrapping events at a specific impurity site or defect. Finally, $1/f$ noise is commonly understood as the superposition of an individual GR noise event with a wide distribution over the lifetime of a GR event on a logarithmically wide timescale.

The power spectral density (PSD) of the current noise of the three components can be described as follows[34]:

$$S(f) = \frac{A}{f^\gamma} + \frac{B}{1 + (f/f_c)^2} + C \tag{5.1}$$

where A, B, f_c, and C are the amplitude of the flicker noise, the amplitude of the GR noise, the corner frequency of the GR noise, the thermal noise (which follows the relationship $C = 4k_B T R$), respectively. Moreover, γ (≈ 1 for most electronic devices) is flicker noise coefficient. In the logarithmic scale PSD, the $1/f$ noise appears as a negatively inclined straight line, and white noise appears as a horizontal base line, whereas GR noise appears as a Lorentzian shape, which is frequency independent for $f < f_c$ and decreases monotonically as frequency increases for $f >$

f_c. The corner frequency of the GR noise, f_c, is attributed to the shortest lifetime of a GR event associated with a specific site. Electronic devices, CMOSs, semiconducting nanowires, CNTs, and graphene devices are never free from flicker noise at low frequency and white noise at high frequency. Since all devices have passed through a device fabrication process, various contaminants, impurities, and defects around and/or inside the channel material are assumed to be the origin of the flicker noise. In CNTs, the presence of defects and impurities cause fluctuation of the total number of free carriers at the contacts and along the CNT channel, which is independent of carrier type and thus become the origin of $1/f$ noise. The amplitude of the $1/f$ noise is inversely proportional to the total number of carriers.[8–11]

Generation-recombination noise has attracted attention due to its characteristic, step-like fluctuation between two states, which is referred to as a random telegraph signal (RTS) in the time-domain current of electronic devices. Note that only a single site of a GR event can provide two-state RTS, and superposition of numerous GR events makes the RTS unobservable[22,23,35]. From the early stage of fine processing technology of solid-state semiconducting devices, RTSs have been observed in CMOS devices, where the origin of the GR event is the charge trap site inside a SiO_2 gate-oxide layer[32,33]. The RTS generated from a charge trap in/on the dielectric layer has also been observed for silicon nanowire[12,13] and CNT[36–39] FET devices. In CNT devices, the RTS can also originate from inorganic particle adsorption on the CNT surface[40], chemical reaction of linked-molecules on the CNT surface[18,20,21], adsorption-desorption of ionized gas molecules[26], and step motion of protein molecules linked to the CNT surface[19].

It is assumed that active molecular adsorption can create a unique and prominent charge trap state on the CNT surface, causing unique RTS and GR noise in CNT-FET devices, which has not yet been reported. The molecules should have higher redox activity and be sufficiently larger than the gas and liquid molecules in or-

der to act as a charge trap site. The RTS noise can provide new opportunities for determining the electronic information about a single molecule adsorbed on the nanotube surface. An elaborately introduced charge trap site will generate prominent and controllable GR noise surpassing the flicker base noise. Hence, molecular functional internal-noise generation in these CNT devices will be achieved. The controllability of large noise generation may contribute to the expansion of noise utilization in future bio-inspired devices, such as neuromorphic devices[41] and sub-threshold-signal detection systems using the stochastic resonance (SR) effect[42,43], in which the presence of optimized noise intensity enhances the signal detection ability of a system.

In this chapter, elucidation of the observations of noise generation in CNT devices due to the charge fluctuation dynamics of the adsorbed molecule under ambient conditions were carried out to clarify the physical mechanism behind this phenomena. Protoporphyrin IX (PP), Zn-protoporphyrin IX (ZnPP), and phosphomolybdic acid (PMo_{12}) adsorption on the CNT devices were explained in this chapter, in which these three molecules have high redox activities. The time- and frequency-domain signals of the current noise were measured t at constant drain and gate voltages. Random telegraph signal were clearly observed for some devices only after molecular adsorption, in which devices prominently generate a Lorentzian-shaped PSD. Quantitative evaluation of the RTS and PSD clearly indicated that each molecule provides unique RTS characteristics related to the electronic and chemical properties of the molecule. The energy level of the most active molecular orbital and the electronic coupling strength between the CNT and the adsorbed molecule were estimated from the RTS data.

5.2   Experimental and theoretical methods[44]

Device fabrication

The pair of catalyst islands for CNT growth was patterned on heavily n-doped silicon substrates capped by a 300-nm SiO_2 layer using photolithography with a bilayer resist (LOR 2A, MicroChem Corp. and AZ-5206-E, AZ Electronic Materials). Subsequently, 5 nm of Co was deposited using electron beam deposition (EBD), followed by lift off in N-methyl-2-pyrrolidone (Sigma Aldrich). The substrates were then introduced into a tube furnace and heated to 550°C for 10 minutes under oxygen flow (500 sccm) to oxidize the Co islands. The furnace was then adjusted to vacuum conditions under an argon flow (100 sccm), and the temperature was ramped to 820°C and held for 10 minutes. At this point, the oxidized-Co was reduced and Co nanoparticles were formed. Carbon nanotubes were then grown by chemical vapor deposition using ethanol as a carbon source for 15 minutes without controlling the flow of ethanol.[45] The gas flow direction was parallel to the catalyst islands in order to ensure the CNT's bridging between those catalyst islands. One or a few carbon nanotubes with an average diameter of 1.5 nm were obtained under this condition between the catalyst islands. The source and drain electrodes were then defined using a similar photolithography method to that used in the previous catalyst patterning process with channel lengths of 4 μm and 20 μm, respectively, followed by the deposition of 4 nm of Cr and 21 nm of Au by EBD and a subsequent lift-off process. After fabrication, the devices were annealed for 1 h at 300°C under vacuum conditions.

Molecular adsorption was performed by a drop casting method. Protoporphyrin IX (PP, Sigma Aldrich), Zn-protoporphyrin IX (ZnPP, Sigma Aldrich), and phosphomolybdic acid (PMo_{12}, Sigma Aldrich) were dissolved in N,N-dimethylformamide (DMF, Sigma Aldrich) at a concentration of 0.5 mg/ml. Then, 10 μl of each solution

was dropped onto substrates containing the CNT devices, which were subsequently annealed at 150°C for several minutes.

Electrical and current noise measurements

Electrical characterization and current noise measurements were performed using an ambient probe station (Apollowave). The probe station was shielded by a metallic box and was stabilized by an air compressor to avoid any unwanted external noise from the environment. The electrical characteristics, such as the IV and FET characteristics, were measured using a semiconductor characterization system (Keithley 4200). The FET characteristics changed slightly after molecular adsorption, and the ON current of the CNT device decreased after molecular adsorption. In the current noise measurements, drain and gate voltages were applied from a battery of 1 and 9 V, respectively. The currents flowing through the devices were converted into voltages using a current-input preamplifier (LI-76, NF Corporation) at a sensitivity of 1 μA/V and were then measured using a real-time spectrum analyzer (Tektronix RSA 3308B). The bandwidth of the real-time spectrum analyzer was set at 20 kHz. Time- and frequency-domain measurements of the current noise were obtained using the same device, before and after molecular adsorption. The time domain signal were sampled for 10 s long. The spectra of frequency domain signal were averaged from 10 spectra to obtain reliable and smooth results. During the current noise measurements, a gate voltage was applied in order to keep the devices in the ON state, so that the current was measurable while decreasing the flicker noise[8–10]. Low-temperature current noise measurements were performed using a low-temperature probe system (TTP3, Lake Shore Cryotronics, Inc.) without additional metal shielding.

Electrochemical measurements

Cyclic voltammetry (CV) and differential pulse voltammetry (DPV) for PP, ZnPP, and PMo_{12} molecules were performed using glassy carbon, platinum wire, and Ag/AgCl as working, counter, and reference electrodes, respectively. Ferrocene was used as an internal standard in all electrochemical experiments. DMF and 0.1 M tetrabutylammonium hexafluorophosphate were used as the solvent and supporting electrolyte, respectively. The scan rate during the CV measurement was 0.1 V/s. All experiments were performed at room temperature.

Theoretical calculations

Calculations were performed using density functional theory (DFT) implemented in the Gaussian 09 program package[46]. Geometry optimization and HOMO-LUMO estimation for PP, ZnPP, and PMo_{12} molecules were calculated using DFT with the B3LYP hybrid functional and LANL2DZ and 6-311G basis sets for metals and other lighter elements, respectively. (19,0) CNTs having a diameter of approximately 1.5 nm, which is similar to that of the CNTs fabricated using homemade CVD method, were used. The (19,0) CNTs consisted of 266 carbon atoms and were terminated by hydrogen atoms. Geometry optimization was performed using a semi-empirical method with the PM6 Hamiltonian implemented in Gaussian 09. HOMO-LUMO estimations were performed using DFT with the B3LYP hybrid functional and 6-311G basis set at fixed coordinates.

5.3 Results and discussion

Pristine CNT devices

CNTs were grown using chemical vapor deposition directly onto SiO_2 layers of silicon substrates. The details of the fabrication method are given in the Experimental Methods section. Semiconducting CNTs having good FET characteristics were chosen as pristine CNT devices. A schematic diagram and an atomic force microscope (AFM) image of the device are shown in Figs. 5.1a and 5.1b, respectively. The gap length between the source and drain electrodes is $\approx 4\mu$m. Figure 5.1a also shows the configuration of the current noise measurement. The time-domain signals of CNT devices were measured at constant drain and gate voltages of 1 and -9 V, respectively. Gate voltages were applied to all devices to keep the devices in the ON state and ensure that the current was measurable by the system. Figure 5.1c shows a time-domain signal of a pristine CNT device with its corresponding histogram showing only one peak. The PSD of the current noise was obtained using a spectrum analyzer with a bandwidth of 20 kHz. Figure 5.1d shows a typical PSD of a pristine CNT device having the $1/f$ characteristic that is common in electronic devices. It is confirmed that all of the pristine CNT devices used in this experiment exhibit a single histogram peak and have a $1/f$ characteristic in time- and frequency-domain measurement, respectively. It is known that $1/f$ noise in a CNT device is generated by both channel and contact resistance in the device.[8–10] The contact resistance generated by the Schottky barrier in a two terminal CNT device is a major component of the total resistance. Keeping the device in the ON state by applying a gate voltage can decrease the $1/f$ noise because the contact and channel resistance are reduced.[8–10]
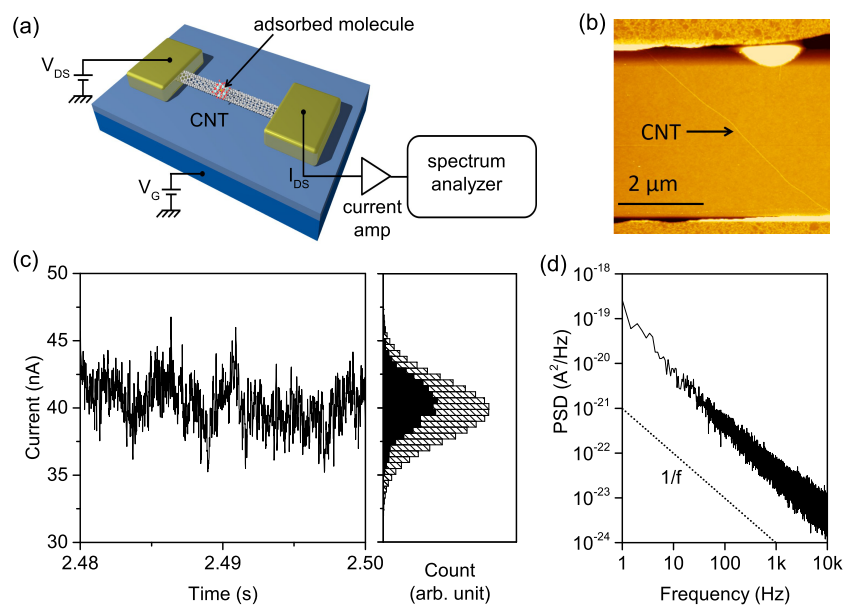
Figure 5.1: Current fluctuation measurement system for the CNT devices. (a) Schematic diagram of the CNT device and measurement configuration. (b) AFM image of the CNT device with one CNT between the S/D electrodes. (c) Time-domain signal of the pristine CNT device with its corresponding histogram (solid shaded). The light shaded histogram corresponds to the long-time-domain signal of 10 s. (d) Power spectral density of a pristine CNT device showing a typical $1/f$ characteristic. This image was taken from Ref. [44].

CNT devices with adsorbed-molecule

Three types of molecules, PP, ZnPP, and PMo_{12}, were adsorbed on CNT devices using a simple drop casting method. The current of CNT+adsorbed-molecule devices were measured using the same method as that used for the pristine CNT devices. Figure 5.2 shows AFM images of CNT before and after adsorption of PMo_{12}. Comparison of the PSD before and after molecular functionalization revealed that most of the devices exhibited an increase in amplitude of the $1/f$ noise of the current noise. There was no significant increase in current noise when solvent without any of the above-mentioned molecules was dropped onto the CNT devices. Another molecule, 6-(Ferrocenyl)hexanethiol, which is expected to have high redox activity were also investigated, as well as the other three molecules, although no noise increase was observed. It is considered that the molecular adsorption on to CNT surface was blocked by thiol ligands, which prefer to bind with Au electrodes. Some of the devices into which the PP, ZnPP, and PMo_{12} molecules were added have peculiar current noise exhibiting a step-like fluctuation referred to as the RTS. Figure 5.3 shows a typical time-domain signal with an RTS and their histograms of the three types of adsorbed molecules. The structure of the corresponding molecules is also shown in Fig. 5.3. Those two-level RTSs were clearly shown in the histogram of both short and long time-domain signals. The appearance of two clear peaks in the histogram is evidence of the RTS signal.

Adsorption of molecules onto the CNT surface increases the noise of a CNT device.[47] However, the appearance of an RTS signal in a CNT device due to the presence of physisorbed organic molecules without any linker molecule has not previously been observed. Previous observation of RTSs in CNT devices due to the adsorption of organic molecules incorporate large molecules, such as protein or DNA molecules and/or use linker molecules to bind the molecules onto the CNT. In these cases, the RTS originated from the dynamic movement of the molecule and chemical reaction

68
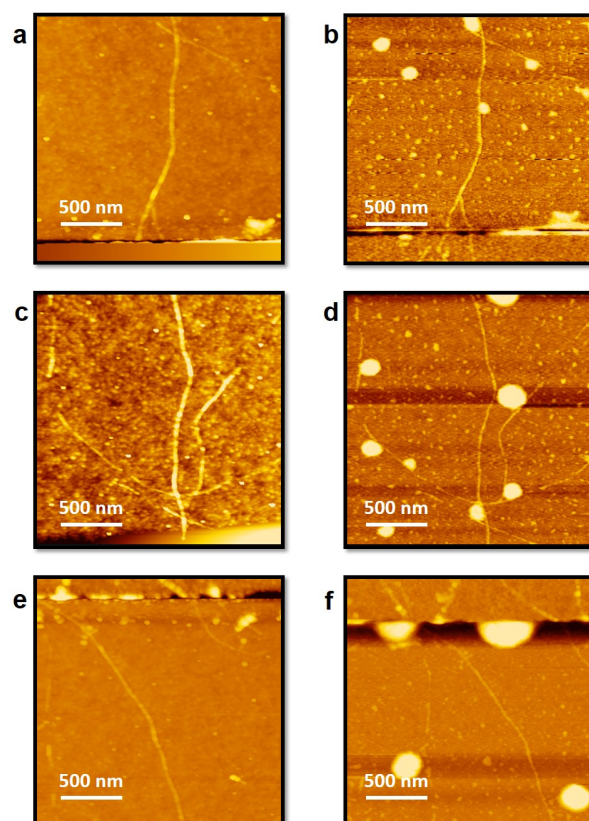
Figure 5.2: AFM images of the CNT device before ((a), (c), and (e)) and after ((b), (d), and (f)) adsorption of PMo_{12} showing the molecules in cluster form. This image was taken from Ref. [44].
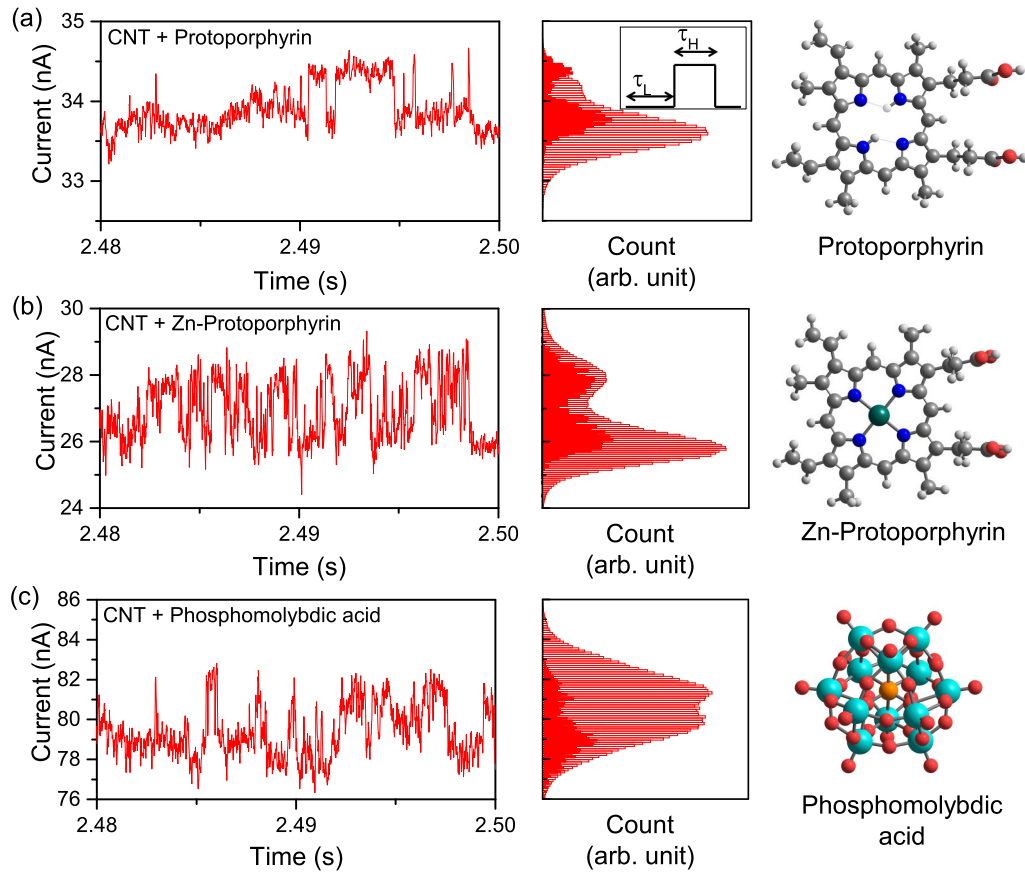
Figure 5.3: Time-domain measurements of current fluctuation in the CNT devices. (a), (b), and (c) are the time-domain signals from CNT+ protoporphyrin, CNT+Zn-protoporphyrin, and CNT+phosphomolybdic acid, respectively, with their corresponding histograms and the structure of the adsorbed molecules (solid shaded). The light shaded histogram corresponds to the long-time-domain signal of 10 s. The inset in the middle panel of (a) is the definition of the lifetime of the RT, where τ_L and τ_H correspond to the times spent in the low- and high-conduction states, respectively. This image was taken from Ref. [44].

on the CNT surface, which modulates the conductance of the CNT.

In this experimental case, the RTS is considered to originate from the charge trap generated by the adsorbed molecule. Fluctuation of the charge occupancy of a trap state near the CNT wall is sufficient to provide conductance modulation of the CNT, in which the trap state acts as a local gate to the CNT itself. The sensitivity of a CNT to this local gating effect was shown in a previous study describing the modulation of the CNT's conductance by the movement of a single protein molecule attached to the CNT.[19] Non-equilibrium Green's function calculations predict that the presence of a point charge within 3 nm of the CNT may have a significant effect on the conductance of the CNT.[39] In this experiment, a large number of molecules were considered to be adsorbed on the CNT. An AFM image of the CNT device after molecular adsorption is provided in the Supplementary Materials. However, note that the RTS originates from a single site. Considering the previous study, only molecules closer than 3 nm to the CNT can act as activated single charge traps and generate the point gate effect. The remaining molecules were considered to be quite far from the CNT and to provide a long-range effect similar to the doping effect, which can increase the $1/f$ noise. If there are numerous adsorbed molecules, which act as activated charge traps, an RTS signal might not be observed because of their superimposition. As such, the probability of the appearance of the RTS was as low as 8 to 10%. Three or more states of the RTS were also observed due to the presence of more than one adsorbed molecule, as shown in Fig. 5.4, which acts as an activated charge trap.

The RTS in the time-domain signal has a one-to-one correspondence with the Lorentzian-shaped PSD in the frequency-domain signal.[48] The devices that exhibited a clear RTS always exhibited a Lorentzian-shaped PSD. In addition, Lorentzian-shaped PSDs were also observed in some devices without a clear RTS. Figures 5.5(a), 5.5(b), and 5.5(c) show the PSDs of CNT+PP, CNT+ZnPP, and CNT+PMo$_{12}$, re-
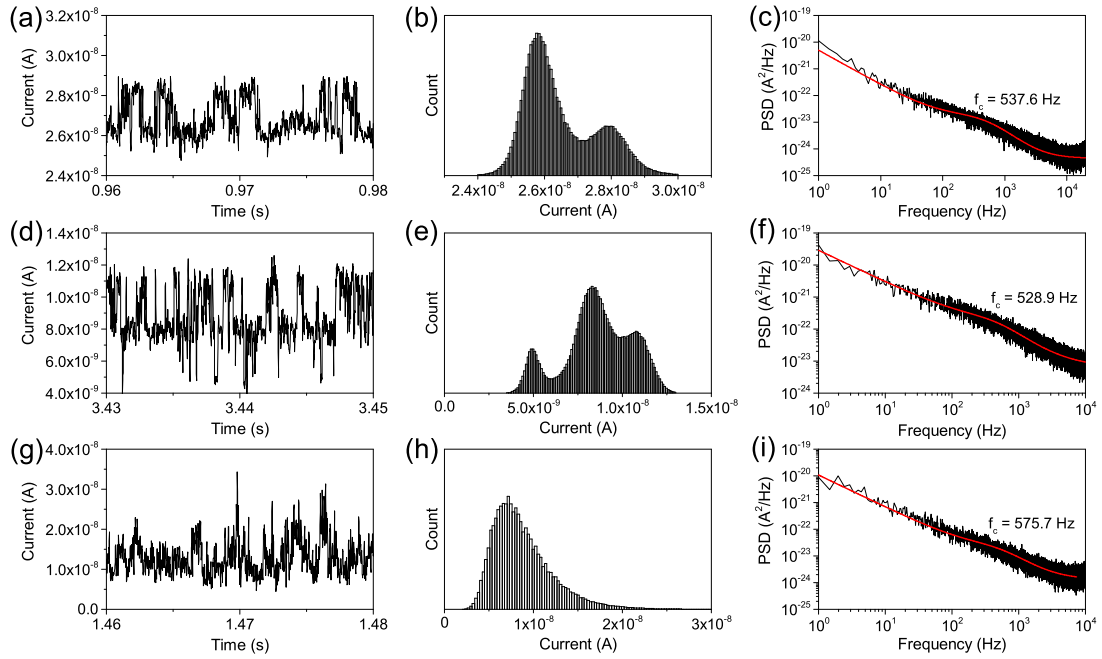
Figure 5.4: Identical PSD corner frequencies after ZnPP adsorption. (a), (b), and (c) show the time-domain signals, histograms of the time-domain signals, and the frequency-domain signals, respectively, from device-1, which exhibited two-state RTSs. (d), (e), and (f) show the time-domain signals, histograms of the time-domain signals, and frequency-domain signals, respectively, from device-2, having three-state RTSs. (g), (h), and (i) are the time-domain signals, histograms of the time-domain signals, and the frequency-domain signals, respectively, from device-3, without any observable RTS. This image was taken from Ref. [44].
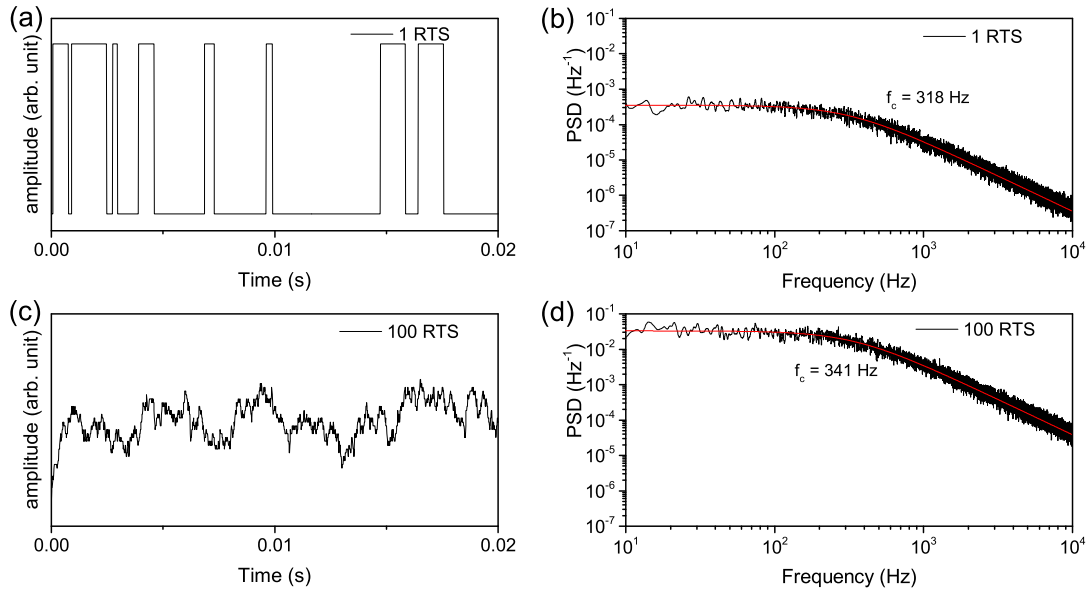
Figure 5.5: Frequency-domain measurements of current fluctuation in the CNT devices. (a), (b), and (c) are the power spectral densities (PSDs) of CNT+protoporphyrin, CNT+Zn- protoporphyrin, and CNT+phosphomolybdic acid, respectively. The spectra in (a), (b), and (c) were fitted using Eq. 5.1 (red lines). The corner frequency (f_c) of the Lorentzian shape is shown in each PSD. This image was taken from Ref. [44].

spectively. The appearance of a Lorentzian-shaped PSD without any RTS can be attributed to the accumulation of RTSs having the same frequency characteristic. This means that, in these devices, there are more than three adsorbed molecules that act as activated charge traps, each of which provides an RTS with the same or a similar frequency characteristic. The probability of the devices having a Lorentzian-shaped PSD without any RTS was two to three times higher than for devices with an RTS.

Numerical simulations were also performed to demonstrate the effect of the number of molecules that provide RTS to the PSD of the current noise. The RTS were created by generating random numbers having a uniform distribution at a given time scale. The random duration of each pulse of these RTSs were defined by generating a random number having an exponential distribution. Those steps were repeated for 100 times and summed all of the RTS data to simulate the RTS from
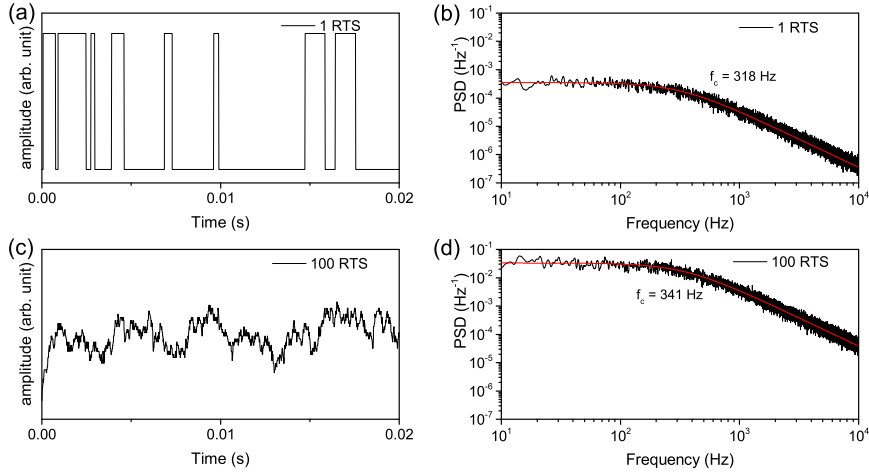
Figure 5.6: Numerical simulation of the RTS. (a) and (c) show the simulated RTS from 1 and 100 molecules, respectively. (b) and (d) show the power spectral density of the simulated RTS from 1 and 100 molecules, respectively. This image was taken from Ref. [44].

100 molecules. The PSDs were obtained by fast Fourier transform followed by the application of a Gaussian filter. The PSDs were fitted using only the second term of Eq. 5.1 in the main text, $S(f) = B/[1 + (f/f_c)^2]$. Figure 5.6 shows the results of numerical simulation. It is clear that the summation of 100 RTSs may obscure, but does not completely hide, the corner frequency of the Lorentzian-shaped PSD.

It is found that the Lorentzian-shaped PSD is unique for each molecular adsorption case. The corner frequency, f_c, were evaluated in order to make a quantitative comparison of all cases. The f_c of the Lorentzian-shaped PSD in Fig. 5.5 can be estimated by fitting the PSD using Eq. 5.1. The f_c values were averaged from more than three devices for each molecular adsorption case and tabulated the results in Table 5.1. The average f_c values for CNT+PP, CNT+ZnPP, and CNT+PMo$_{12}$ were 67.7±17.3, 533.7±11.9, and 755.9±29.4 Hz, respectively. These results clearly indicate that the corner frequency of the Lorentzian-shaped PSD is unique for each molecule. Here, f_c is related to the fastest transition rate between two states. In this experiment, f_c should correspond to the barrier height of the charge trapping-detrapping event. It is clear that PP has a low f_c, which can also be understood

74

Table 5.1: Comparison of the extracted RTS characteristics and the chemical properties of the adsorbed molecules. This data was taken from Ref. [44].

Adsorbate	$\bar{f}_c$ (Hz)	Lifetime			E_{ox}^1 (V)	E_{red}^1 (V)	E_{red}^2 (V)	$E_T - E_F$ (meV)	Charge state
		$\bar{\tau}_L$ (ms)	$\bar{\tau}_H$ (ms)	$\bar{\tau}_L/\bar{\tau}_H$					
PP	67.7±17.3	3.73	1.50	2.49	0.42	-1.72	-	-41.5	$N \leftrightarrow +1$
ZnPP	541.1±16.4	1.02	0.67	1.52	0.17	-1.98	-	-28.8	$N \leftrightarrow +1$
PMo$_{12}$	755.9±29.4	0.78	0.77	1.01	-	-0.27	-0.42	18.3	$N \leftrightarrow -1$ $-1 \leftrightarrow -2$ [a]

[a] based on DFT calculation results.

as a long RTS lifetime (see Fig. 5.3(a)), as compared to the other two molecules. Moreover, PP and ZnPP have similar molecular structures. However, both molecules have quite different barrier energies, represented by f_c, which might correlate to the electronic coupling strength between these two molecules (PP and ZnPP) and the CNT, as well as their electronic properties.

Pristine CNT devices also have charge traps that come from other sources, such as CNT defects, defects in the gate dielectric material, and the water layer. Generally, these charge traps have a wide range of energy levels and barrier energies, leading to the appearance of $1/f$ noise due to the superposition of multiple GR noise events having different f_c values. Although rare, some of these charge traps may provide an RTS or Lorentzian-shaped PSD to the pristine CNT devices. However, such devices were excluded from our experiments at the first screening. Charge trapping-detrapping events strongly depend on temperature, whereas we performed experiments focusing on the events at room temperature. In our case, the newly formed small number of charge traps that originated from the molecular adsorption have a certain energy level, and thus provide an RTS and a single f_c of the Lorentzian-shaped PSD, which can be observed at room temperature.

The unique f_c of the Lorentzian-shaped PSD due to the adsorption of various gas molecules has been observed in graphene devices. The origin of the Lorentzian-shaped PSD is considered to be the formation of charge traps as a result of vapor exposure, although the specific mechanism of the observed Lorentzian noise in graphene might be different from that in a semiconductor device including CNTs.

Other device based on 2-D material such as MoS_2 also show some change of noise characteristic due to adsorption of various gas molecule though only in the amplitude of $1/f$ noise without any Lorentzian-shaped PSD nor RTS signal.[25] The Lorentzian-shaped PSD observed in this experiment can also be used to characterize the adsorbed molecule, similar to the graphene case. On the other hand, the probability of having a single molecular adsorption in graphene is lower than that in CNT owing to the large surface area of the 2-D structure. Hence, no RTS has been observed in graphene devices. The RTS observed in CNT device in this originates from a single molecule and contains detailed information of the molecule that cannot be derived from a Lorentzian-shaped PSD.

Energy level estimation of the origin of RTS

Lifetime analysis of the RTS were performed using a similar approach to that used to model the RTS in silicon[32] and CNT[40] FET devices. The ratio of the lifetime of the two states in RTS correspond to the energy level difference between the Fermi level of the CNT and the charge trap level of the adsorbed molecules. Time-domain signals of 10 s with an RTS were fitted using a hidden Markov model implemented in vbFRET[49] software to extract the RTS characteristics. Figure 5.7 shows the fitting of RTS signal and the distribution of the lifetime of RTS which were fitted using double exponential function. The RTS characteristics, represented by τ_L and τ_H, were obtained corresponding to the lifetime of the RTS in low and high conduction states, respectively, as shown in the inset of Fig. 5.3(a). The average values of τ_L (τ_H) for CNT+PP, CNT+ZnPP, and CNT+PMo$_{12}$ were 3.73 (1.50), 1.02 (0.67), and 0.78 (0.77) ms, respectively. The average RTS lifetimes are tabulated in Table 5.1. Using the model of a charging-discharging event of the adsorbed molecule (as illustrated in Fig. 5.5(a)), the relative energy difference between the Fermi level (E_F) of the device channel, i.e., CNT E_F, and the trap level (E_T), which is the molecular

orbital energy, can be estimated by evaluating the ratio between τ_c and τ_e, which correspond to the charging and discharging times, respectively, of a molecule. Here, semiconducting CNT were treated as a metallic semiconductor due to applied gate voltage keeping the CNT in the on-state. This model is represented by the following equation:

$$\frac{\tau_c}{\tau_e} = g \exp\left(\frac{E_T - E_F}{k_B T}\right) \tag{5.2}$$

where g, k_B, and T are the degeneration factor, the Boltzmann constant, and the temperature, respectively. The absolute values of the energy level difference, $|E_T - E_F|$, are 41.5, 28.8, and 18.3 meV for PP, ZnPP, and PMo_{12}, respectively, and are tabulated in Table 5.1. Since the RTS is generated by the charging and discharging of the adsorbed molecule, information on the molecular states should be clarified to assign $\tau_L/\tau_H = \tau_c/\tau_e$ or $\tau_H/\tau_L = \tau_c/\tau_e$.

In order to identify the molecular orbital which acts as a charge trap responsible for the RTS, density functional theory (DFT) calculations were performed using Gaussian 09 software[46] to estimate the HOMO-LUMO level of the CNTs and molecules used in this experiment. The optimized structures of these molecules are shown in Fig. 5.3, and the HOMO-LUMO levels of these molecules are shown in Fig. 5.8(b). The HOMO (LUMO) levels of CNT (19,0), PP, ZnPP, PMo_{12}, and $[PMo_{12}]^{-1}$ were -4.12 (-3.88), -5.40 (-2.58), -5.33 (-2.50), -9.67 (-6.46), and -5.33 (-3.82) eV, respectively, where $[PMo_{12}]^{-1}$ represents the molecule reduced by one electron from neutral (anion). The redox properties of these molecules were also measured using differential pulse voltammetry (DPV). Figure 5.9 shows the voltammetry measurement results. Here, E_{ox}^1 denotes the first oxidation potential, and E_{red}^1 and E_{red}^2 denote the first and second reduction potentials, respectively. Then, E_{ox}^1 (E_{red}^1) for PP and ZnPP are 0.42 (-1.72) and 0.17 (-1.98) V, respectively, while only the reduction potentials, which were -0.27 and -0.42 V for E_{red}^1 and E_{red}^2, respectively, were observed in PMo_{12}. These redox potentials are tabulated in Table 5.1.
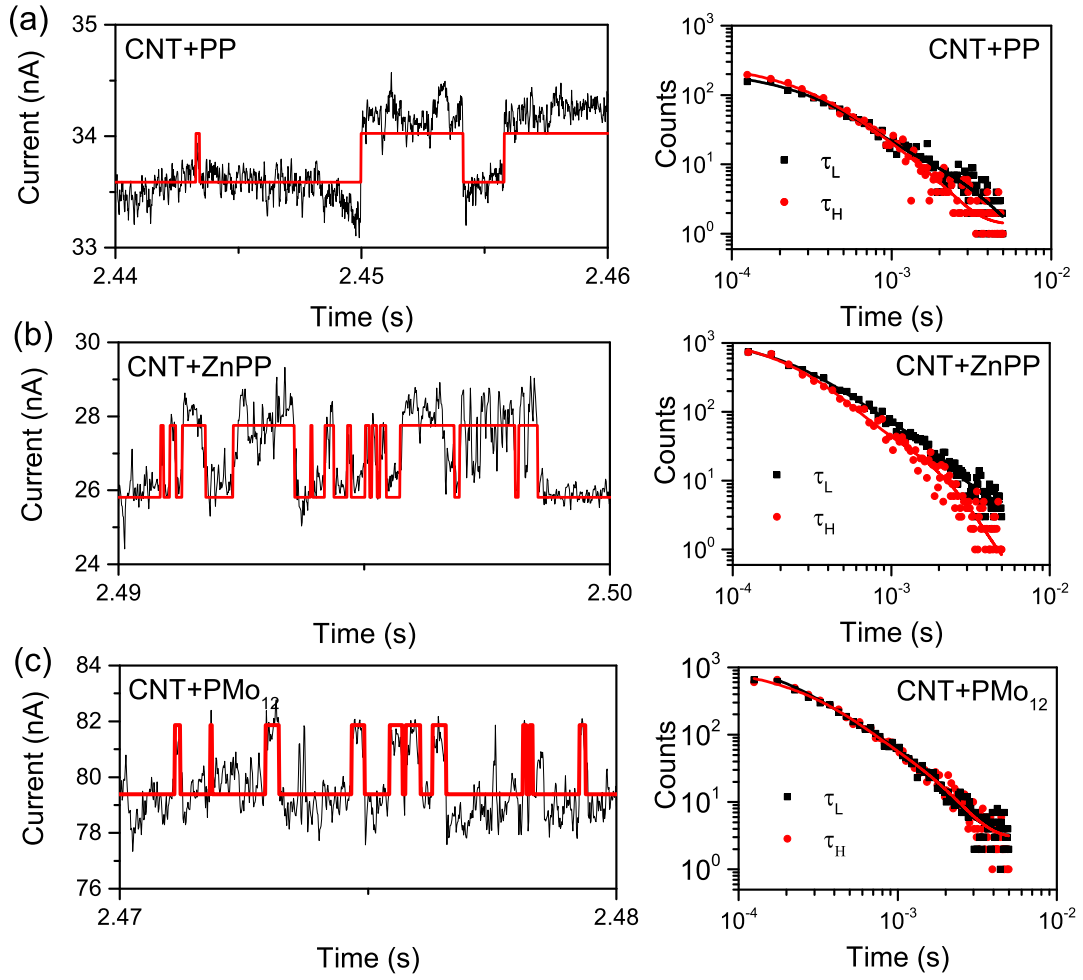
Figure 5.7: Fitting of the time-domain signal with the RTS using the hidden Markov model for the case of (a) CNT+PP, (b) CNT+ZnPP, and (c) CNT+PMo$_{12}$. The right-hand panel in each row show the lifetime distribution of the RTS signal, which was fitted using an exponential equation. This image was taken from Ref. [44].
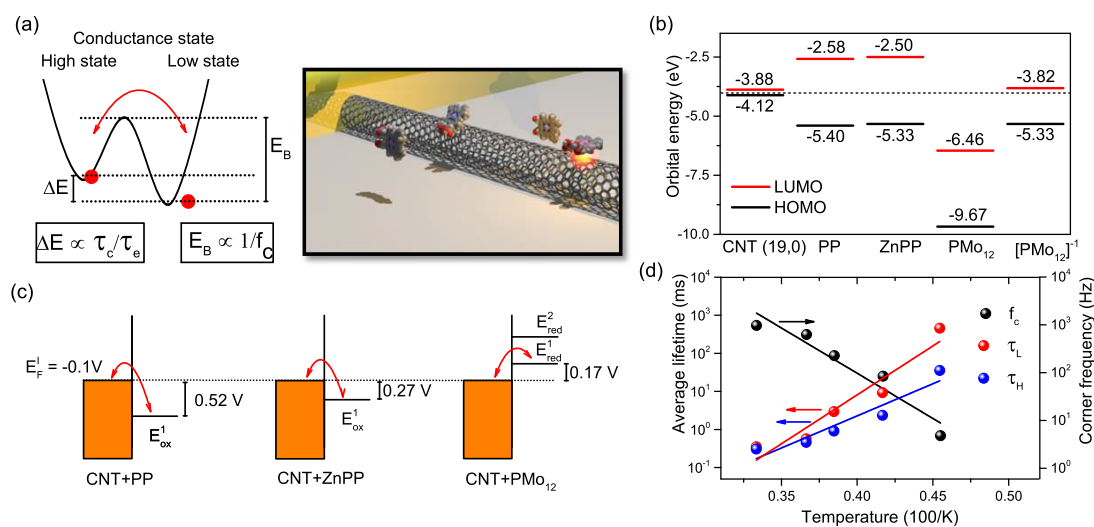
Figure 5.8: Mechanism of the RTS in the CNT devices. (a) Bistable conductance state of the CNT due to electron transfer from/to the CNT, which changes the molecular charge state, along with an illustration of the molecular-local-gate of the CNT devices. The ratio of the average lifetime of an RTS is proportional to the energy difference between the Fermi level of the CNT and the molecular state, while the barrier energy between these two states is inversely proportional to the corner frequency of the Lorentzian-shaped PSD. (b) HOMO-LUMO levels of CNT (20,0), PP, ZnPP, and PMo_{12}. $[PMo_{12}]^{-1}$ represents the neutral form reduced by one electron (anion). The horizontal dotted line represents the Fermi level of the CNT. (c) Energy band diagram of the CNT and the adsorbed molecule based on DPV measurements. (d) Temperature dependence of the average lifetime and corner frequency (f_c) of the RTS for CNT+PMo_{12}. This image was taken from Ref. [44].
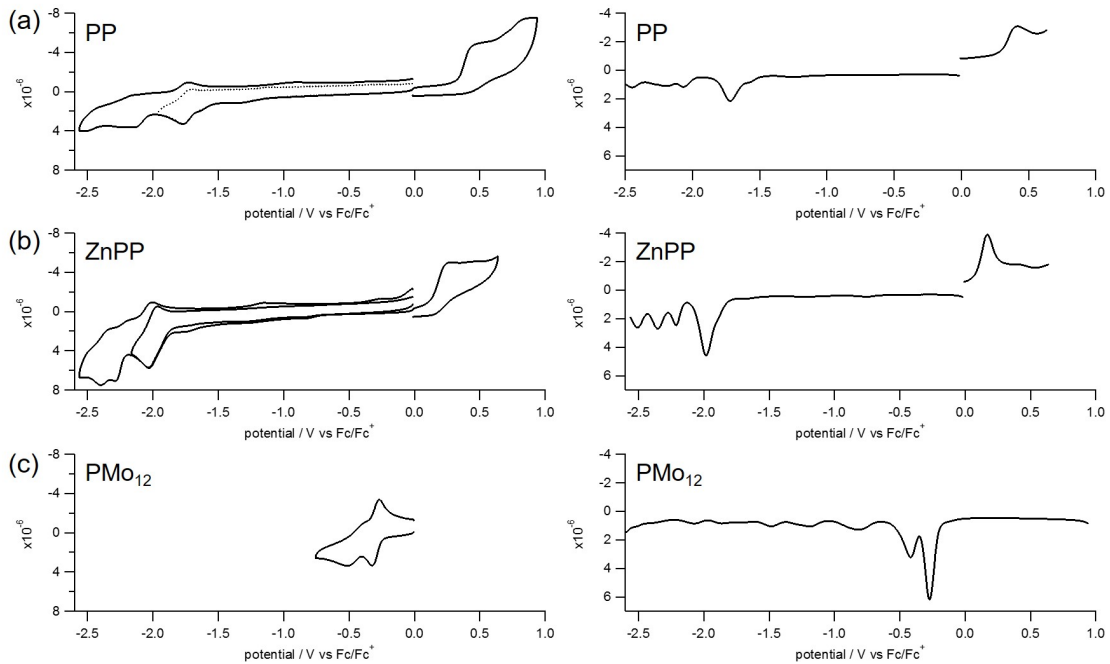
Figure 5.9: Results of electrochemical measurements. (a), (b), and (c) show the voltammetry measurement results for PP, ZnPP, and PMo$_{12}$ molecules, respectively. The left- and right-hand panels show the CV and DPV curves, respectively. This image was taken from Ref. [44].

Note that neither DFT calculation nor voltammetry measurement is ideal for describing the energy level alignment of this experiment. In the case of DFT, the HOMO-LUMO level were estimated from an isolated molecule. In the case of voltammetry, the redox properties were measured from a large number of molecules in solution against a platinum electrode. From the DFT calculation of PP and ZnPP, it is difficult to assign the molecular charge state responsible for the RTS because the Fermi level of the CNT is located almost at the center of the HOMO-LUMO gap between these molecules. On the other hand, for PP and ZnPP, E^1_{ox} is much lower than E^1_{red}, which strongly suggests that electron transfer from the molecule to the metal electrode is likely to occur, resulting in a transition of the molecular charge states of PP and ZnPP from neutral to a +1 charged state, which is responsible for the RTS. In the case of PMo$_{12}$, DFT calculation provides a much lower LUMO level as compared to the Fermi level of the CNT, which means that the adsorbed PMo$_{12}$ on the CNT should be negatively charged (reduced). The LUMO

80

of $[PMo_{12}]^{-1}$ is close to the Fermi level of the CNT, suggesting that there is a transition of molecular charge states from -1 to -2 that is responsible for the RTS. On the other hand, in voltammetry, there is no observable oxidation potential, although two reduction potentials were observed. It is known that PMo_{12} is a polyoxometalate that has multiple redox properties. The lack of an observable oxidation peak suggests that the first reduction peak corresponds to the transition from neutral to -1. The voltammetry results for PMo_{12} indicate that a transition of the molecular charge state from neutral to -1 is responsible for the RTS.

Based on a comparison of the $\bar{\tau}_L/\bar{\tau}_H$ ratios (see Table 5.1), it is assumed that the Fermi level of the CNT (E_F^I) is located at -0.1 V (vs. F_C/F_C^+). Under this assumption, the absolute energy difference between the Fermi level of the CNT and the redox potentials $|E_F^I - E_{redox}|$ of PP, ZnPP, and PMo_{12} are 0.52, 0.27, and 0.17 V, respectively, which provide ratios similar to the $\bar{\tau}_L/\bar{\tau}_H$ ratios of 2.49, 1.52, and 1.01, respectively. Figure 5.8(c) shows a simple energy diagram describing the charge transfer between the CNT and the adsorbed molecules based on the DPV measurement and the RTS lifetime ($\bar{\tau}_L/\bar{\tau}_H$ ratio). This model strongly suggests that the fluctuation of the molecular charge state of PMo_{12} which is responsible for the RTS, is from neutral to -1.

Figure 5.10 shows simple band diagram of CNT device after molecular adsorption. In the case of PP and ZnPP, HOMO level of the molecules act as a charge trap. The positively charged PP or ZnPP molecule slightly decrease the valence band of the CNT, and thus decreases the conductance of the CNT as shown in Fig. 5.10(a). On the other hand, in the case of PMo_{12}, LUMO level of the molecule act as a charge trap. The positively charged PMo_{12} molecule slightly increase the valence band of the CNT, and thus increases the conductance of the CNT as shown in Fig. 5.10(b). Therefore, the active molecular orbital which act as a charge trap play an important role in providing step-like fluctuation of CNT device.
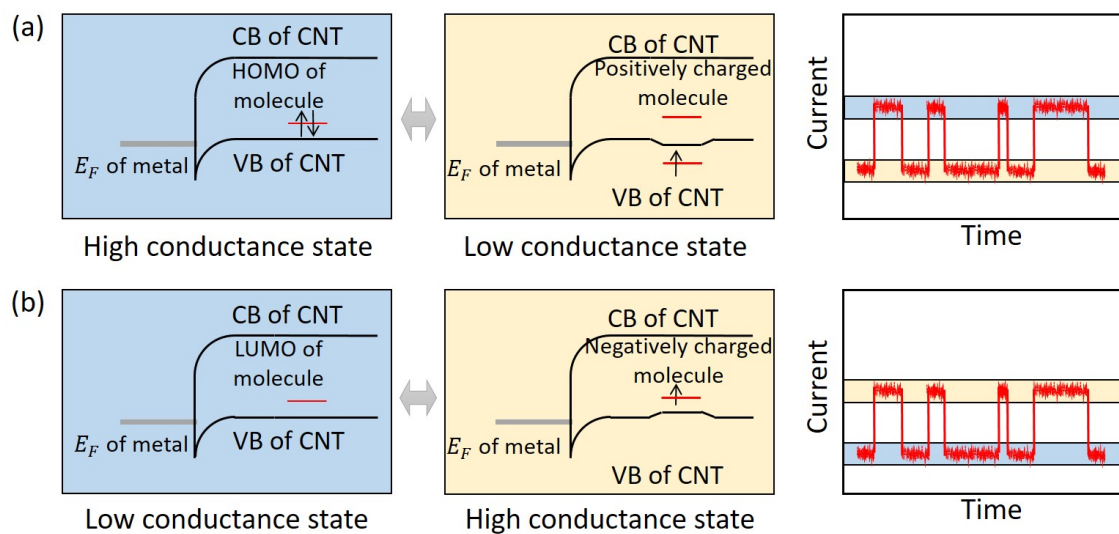
Figure 5.10: Simple band diagram of the CNT device after adsorption of PP and ZnPP (a), and PMo$_{12}$ (b).

From the DFT and DPV results, it can be deduced that, for PP and ZnPP, τ_c (the charging time) and τ_e (the discharging time) correspond to τ_H and τ_L, respectively, and the opposite is true for PMo$_{12}$. Thus, the energy differences between the Fermi level and the molecular trap state, as estimated using Eq. 5.2, are -41.5, -28.8, and +18.3 meV for PP, ZnPP, and PMo$_{12}$, respectively, as tabulated in Table 5.1. The plus and minus signs correspond to molecules acting as electron acceptors and electron donors, respectively. It is clear that the RTS characteristics depend on the chemical properties of the adsorbed molecules because $|E_T - E_F|$ exhibits a similar trend to the results obtained from DFT calculation and voltammetry measurement for three kinds of molecules examined in this experiment.

Temperature-dependence measurements were performed in order to investigate the charge transfer mechanism between the CNT and the PMo$_{12}$ molecule. The barrier energy was assumed to be inversely proportional to the corner frequency ($E_B \propto 1/f_c$), as illustrated in Fig. 5.8(a). It is believed that the barrier energy depends on the coupling strength between the CNT and the adsorbed molecule. A lower barrier energy will shorten the time spent in both the high and low conduction states, resulting in a higher frequency. A clear RTS can be observed from room temperature

to 220 K, but the RTS starts to vanish at 200 K as shown in Fig. 5.11. Figure 5.8(d) shows the temperature dependence of $\bar{\tau}_L$, $\bar{\tau}_H$, and f_c from room temperature to 220 K. Unfortunately, a clear Lorentzian-shaped PSD could not observed due to the additional noise from the unshielded variable-temperature vacuum probe system, although this noise did not affect the appearance of the RTS. The f_c were evaluated based on the average RTS lifetime using the relationship $2\pi f_c = \left(\bar{\tau}_L + \bar{\tau}_H\right) / \left(\bar{\tau}_L \bar{\tau}_H\right)$. Measurement results clearly indicate a thermally activated RTS, with an activation energy of f_c of 0.376 eV for the CNT+PMo$_{12}$ case. The activation energy of $\bar{\tau}_L$ and $\bar{\tau}_H$ are 0.5097 and 0.3346 eV, respectively. The difference between these two values is 0.1751 eV, corresponding to the difference between the Fermi level of the CNT and the active molecular orbital of the PMo$_{12}$, which is in good agreement with the energy-level evaluation based on the DPV measurement. Considering the relationship between the barrier energy and the corner frequency, PP and ZnPP will have higher barrier energies, corresponding to lower corner frequencies, as compared to PMo$_{12}$.

Random telegraph signals in CNT devices that originated from charge trapping-detrapping events have been reported in only two cases: charge traps in/on a dielectric layer[36–39] and an inorganic nanocrystal adsorbed on CNT[40]. In these cases, the energy level of the charge trap is not unique because it is associated with impurity or defect sites. In this research, the charge traps originated from the electronic structure of the adsorbed organic molecules, which have a unique molecular orbital. Therefore, the observed f_c was unique for each molecular adsorption case, even though there is no observable RTS due to the existence of multiple charge traps. It is expected that a large number of identical adsorbed-molecules on a CNT will provide additional prominent noise consisting of accumulated RTSs with identical frequencies.
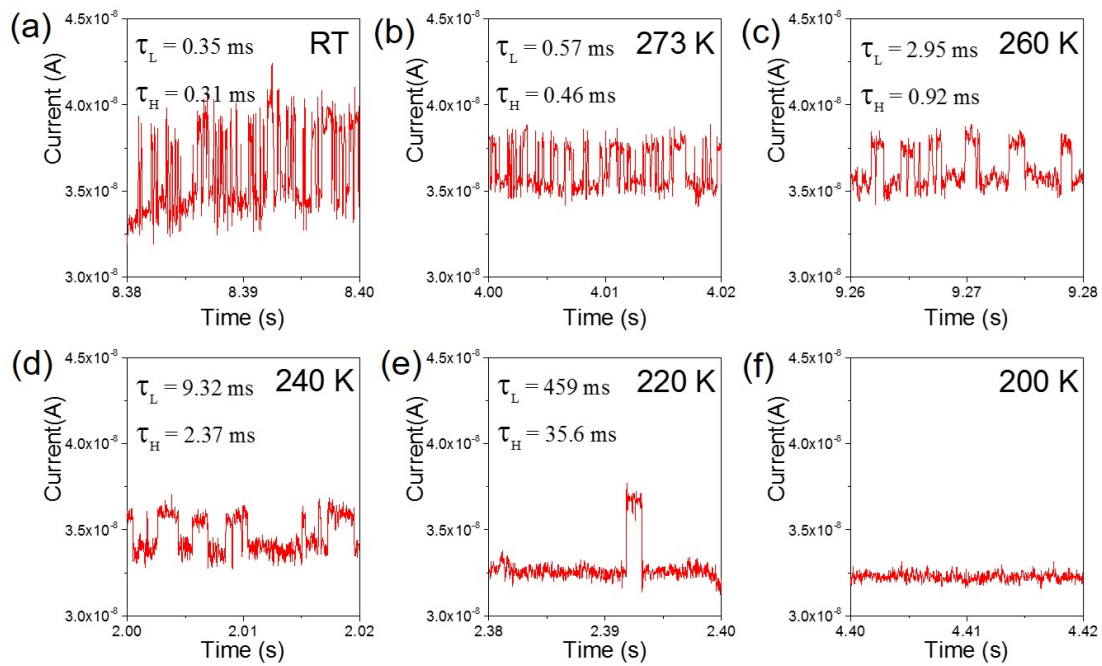
Figure 5.11: Temperature dependence of the RTS for CNT+PMo$_{12}$. (a), (b), (c), (d), (e), and (f) show the time-domain signals of the device at room temperature and at 273, 260, 240, 220, and 200 K, respectively, and $\bar{\tau}_L$ and $\bar{\tau}_H$ are the average RTS lifetimes. The RTS completely vanishes at 200 K. This image was taken from Ref. [44].

5.4 Conclusion

In conclusion, unique RTS and GR noise behaviors were clearly observed in CNT devices due to the adsorption of molecules. The results show that the GR noise originates from the fluctuation dynamics of the molecular charged states, revealing two important pieces of information. First, the corner frequency of the Lorentzian-shaped PSD of the GR noise is unique to the type of molecule. It is proposed that the corner frequency is inversely proportional to the barrier energy between the channel and the adsorbed molecule, which describes the electronic coupling strength between the channel and the adsorbed molecule. Second, the ratio between the average lifetimes at high and low conductances of RTS contains information on the chemical properties regarding the most active single molecule, which can be extracted only from the RTS. It is likely that the detection of single-molecular RTS is limited to one-dimensional materials like CNTs. The active GR noise generated by adding homogeneous chemical species would not be limited to CNTs, but would occur in other two-dimensional systems, such as graphene. Hence, the molecular GR noise detection method using low-dimensional nanomaterials can be used to characterize a single molecule, and this system can also generate frequency-controllable internal noise, which will be useful in developing future bio-inspired devices, such as neuromorphic[41] and stochastic resonance devices[1–6,42,43]. A better understanding of the noise characteristics will provide a new paradigm whereby the presence of noise can be advantageous in electronics.

References

1. Mori, T. & Kai, S. Noise-induced entrainment and stochastic resonance in human brain waves. *Phys. Rev. Lett.* **88,** 218101 (2002).

2. Kitajo, K., Nozaki, D., Ward, L. M. & Yamamoto, Y. Behavioral stochastic resonance within the human brain. *Phys. Rev. lett.* **90,** 218103 (2003).

3. Destexhe, A. & Contreras, D. Neuronal computations with stochastic network states. *Science* **314,** 85–90 (2006).

4. Douglass, J., Wilkens, L., Pantazelou, E. & Moss, F. Noise enhancement of information transfer in crayfish mechanoreceptors by stochastic resonance. *Nature* **365,** 337–340 (1993).

5. Collins, J, Chow, C & Imhoff, T. Stochastic resonance without tuning. *Nature* **376,** 236–238 (1995).

6. Russell, D. F., Wilkens, L. A. & Moss, F. Use of behavioural stochastic resonance by paddle fish for feeding. *Nature* **402,** 291–294 (1999).

7. Collins, P. G., Fuhrer, M. & Zettl, A. 1/f noise in carbon nanotubes. *Appl. Phys. Lett.* **76,** 894–896 (2000).

8. Snow, E. S., Novak, J. P., Lay, M. D. & Perkins, F. K. 1f noise in single-walled carbon nanotube devices. *Appl. Phys. Lett.* **85,** 4172–4174 (2004).

9. Lin, Y.-M., Appenzeller, J., Knoch, J., Chen, Z. & Avouris, P. Low-frequency current fluctuations in individual semiconducting single-wall carbon nanotubes. *Nano Lett.* **6,** 930–936 (2006).

10. Tersoff, J. Low-frequency noise in nanoscale ballistic transistors. *Nano Lett.* **7,** 194–198 (2007).

11. Tobias, D. *et al.* Origins of $1f$ noise in individual semiconducting carbon nanotube field-effect transistors. *Phys. Rev. B* **77,** 033407 (2008).

12. Zhuge, J, Zhang, L, Wang, R & Huang, R. Random telegraph signal noise in gate-all-around silicon nanowire transistors featuring Coulomb-blockade characteristics. *Appl. Phys. Lett.* **94,** 083503 (2009).

13. Clément, N, Nishiguchi, K, Fujiwara, A & Vuillaume, D. One-by-one trap activation in silicon nanowire transistors. *Nat. Commun.* **1,** 92 (2010).

14. Balandin, A. A. Low-frequency 1/f noise in graphene devices. *Nat. Nanotech.* **8,** 549–555 (2013).

15. Brunner, J, González, M., Schönenberger, C & Calame, M. Random telegraph signals in molecular junctions. *J. Phys.: Condens. Matter* **26,** 474202 (2014).

16. Adak, O. *et al.* Flicker noise as a probe of electronic interaction at metal-single molecule interfaces. *Nano Lett.* **15,** 4143–4149 (2015).

17. Crossno, J, Liu, X, Ohki, T., Kim, P & Fong, K. C. Development of high frequency and wide bandwidth Johnson noise thermometry. *Appl. Phys. Lett.* **106,** 023121 (2015).

18. Sorgenfrei, S. *et al.* Label-free single-molecule detection of DNA-hybridization kinetics with a carbon nanotube field-effect transistor. *Nat. Nanotech.* **6,** 126–132 (2011).

19. Choi, Y. *et al.* Single-molecule lysozyme dynamics monitored by an electronic circuit. *Science* **335,** 319–324 (2012).

20. Bouilly, D. *et al.* Single-molecule reaction chemistry in patterned nanowells. *Nano Lett.* **16,** 4679–4685 (2016).

21. Goldsmith, B., Coroneus, J., Kane, A., Weiss, G. & Collins, P. Monitoring single-molecule reactivity on a carbon nanotube. *Nano Lett.* **8,** 189–194 (2008).

22. Zheng, G., Gao, X. & Lieber, C. Frequency domain detection of biomolecules using silicon nanowire biosensors. *Nano Lett.* **10,** 3179–3183 (2010).

23. Rumyantsev, S., Liu, G., Shur, M. S., Potyrailo, R. A. & Balandin, A. A. Selective gas sensing with a single pristine graphene transistor. *Nano Lett.* **12,** 2294–2298 (2012).

24. Rumyantsev, S., Liu, G., Potyrailo, R. A., Balandin, A. A. & Shur, M. S. Selective sensing of individual gases using graphene devices. *IEEE Sensors J.* **13,** 2818–2822 (2013).

25. Samnakay, R., Jiang, C., Rumyantsev, S., Shur, M. S. & Balandin, A. A. Selective chemical vapor sensing with few-layer MoS_2 thin-film transistors: Comparison with graphene devices. *Appl. Phys. Lett.* **106,** 023115 (2015).

26. Bushmaker, A. *et al.* Single-ion adsorption and switching in carbon nanotubes. *Nat. Commun.* **7,** 10475 (2016).

27. Vasudevan, S & Ghosh, A. Using room temperature current noise to characterize single molecular spectra. *ACS Nano* **8,** 2111–2117 (2014).

28. Holmes, J., Johnston, K., Doty, C. & Korgel, B. Control of thickness and orientation of solution-grown silicon nanowires. *Science* **287,** 1471–1473 (2000).

29. Iijima, S. Helical microtubules of graphitic carbon. *Nature* **354,** 56–58 (1991).

30. Novoselov, K. S. *et al.* Electric field effect in atomically thin carbon films. *Science* **306,** 666–669 (2004).

31. Mak, K. F., Lee, C., Hone, J., Shan, J. & Heinz, T. F. Atomically thin MoS_2: A new direct-gap semiconductor. *Phys. Rev. Lett.* **105,** 136805 (2010).

32. Ralls, K. *et al.* Discrete resistance switching in submicrometer silicon inversion layers: Individual Interface Traps and Low-Frequency (1/f) Noise. *Phys. Rev. Lett.* **52,** 228 (1984).

33. Uren, M., Kirton, M. & Collins, S. Anomalous telegraph noise in small-area silicon metal-oxide-semiconductor field-effect transistors. *Phys. Rev. B* **7,** 8346 (1988).

34. Vitusevich, S. & Gasparyan, F. in *Carbon nanotubes applications on electron devices* (ed Arulanda, J. M.) chap. 11 (InTech, 2011).

35. Inoue, S, Kuroda, R, Yin, X, Sato, M & Kasai, S. Detection of molecular charge dynamics through current noise in a GaAs-based nanowire FET. *Jpn. J. Appl. Phys* **54,** 04DN07 (2015).

36. Peng, Hughes & Golovchenko. Room-temperature single charge sensitivity in carbon nanotube field-effect transistors. *Appl. Phys. Lett.* **104,** 243502 (2006).

37. Liu, F. & Wang, K. L. Correlated random telegraph signal and low-frequency noise in carbon nanotube transistors. *Nano Lett.* **8,** 147–151 (2008).

38. Chan, J. *et al.* Reversal of current blockade in nanotube-based field effect transistors through multiple trap correlations. *Phys. Rev. B* **80,** 033402 (2009).

39. Sharf, T. *et al.* Single electron charge sensitivity of liquid-gated carbon nanotube transistors. *Nano Lett.* **14,** 4925–4930 (2014).

40. Zbydniewska, E. *et al.* Charge blinking statistics of semiconductor nanocrystals revealed by carbon nanotube single charge sensors. *Nano Lett.* **15,** 6349–6356 (2015).

41. Rieke, F., Warland, D., de Ruyter van Steveninck, R. & William, B. *Spikes: Exploring the neural code* (MIT Press, Cambridge MA, 1997).

42. Kasai, S. & Asai, T. Stochastic Resonance in Schottky Wrap Gate-controlled GaAs Nanowire Field-Effect Transistors and Their Networks. *Appl. Phys. Express* **1,** 083001 (2008).

43. Hakamata, Y. *et al.* Enhancement of weak-signal response based on stochastic resonance in carbon nanotube field-effect transistors. *J. Appl. Phys.* **108,** 104313 (2010).

44. Setiadi, A. *et al.* Room-temperature discrete-charge-fluctuation dynamics of a single molecule adsorbed on a carbon nanotube. *Nanoscale* **9,** 10674–10683 (2017).

45. Kawahara, T *et al.* Diameter dependence of 1/f noise in carbon nanotube field effect transistors using noise spectroscopy. *Appl. Surf. Sci.* **267,** 101–105 (2013).

46. Frisch, M. J. *et al. Gaussian 09, Revision E.01* Gaussian Inc., Wallingford CT 2009.

47. Sharf, T., Kevek, J. W., Deborde, T., Wardini, J. L. & Minot, E. D. Origins of charge noise in carbon nanotube field-effect transistor biosensors. *Nano lett.* **12,** 6380–6384 (2012).

48. Simoen, E., Kaczer, B., Toledano-Luque, M. & Claeys, C. (Invited) Random telegraph noise: From a device physicist's dream to a designer's nightmare. *ECS Transactions* **39,** 3–15 (2011).

49. Bronson, J. E., Fei, J., Hofman, J. M., Gonzalez, R. L. & Wiggins, C. H. Learning rates and states from biophysical time series: a Bayesian approach to model selection and single-molecule FRET data. *Biophys. J.* **97,** 3196–3205 (2009).

Chapter 6

Development of Carbon Nanotube-based Stochastic Resonance Device with Molecular Noise Source

6.1 Introduction

Current noise is viewed as a harmful factor in electronic devices, in which many attempts are made to eliminate noise to increase device performance. On the other hand, biological[1–6] and physical[7–9] systems exploit noise to enhance signal transmission, including neural circuits in the human brain.[10–12] One useful phenomenon, called stochastic resonance (SR), enables biological systems to utilize noise to enhance the transmission or detection of signals below the threshold level.[13–15] For example, paddlefish living in muddy rivers can feed on the nearest plankton only when there is background electrical noise coming from another plankton mass.[2,3] Crayfish can detect subtle water movement of predators in the presence of mechanical noise

in water.[1,4] SR in the human brain's visual processing, whereby undetectable light signal to the right eye becomes detectable through the addition of noise to the left eye, has also been investigated.[10,11]

Modern electronics has yet to exploit SR, however, it is considered that a SR-based technique can potentially be used to develop novel bio-inspired electronic devices with low power consumption. Much effort has already been devoted to developing artificial SR electronic systems.[16–24] There are two basic requirements for developing an SR-based electronic device: a signal detection threshold and the presence of additional noise. The SR effect has been investigated in a Si nanowire device utilizing a threshold in field-effect transistor (FET) transfer characteristics by applying external electronic noise.[16] Generally, attempts at developing SR-based electronic devices involve a multiple junction structure to ensure significant enhancement of the signal response. The multiple SR effect has been demonstrated by using GaAs nanowire devices with a FET threshold,[17–19] carbon nanotube (CNT)-FETs,[20–22] DNA networks with a molecular redox circuit,[23] and VO_2 thin films having a phase transition threshold[24].

It is easy to understand how summing of noisy supra-threshold signals from multiple SR junctions increase the efficiency of signal transmittance. Collins et al. demonstrated theoretically that the summing signals of multiple SR units dramatically improve the correlation between a range of weak (subthreshold) input and detected output signals, irrespectively of the nature of the input signal.[14] They also showed that the sum of a large number of parallel SR signals is independent of the noise magnitude. Single SR systems need optimized noise intensity to obtain significant enhancement of that correlation, whereas increasing the number of parallel summing networks enhances the correlation over a wide range of noise intensities, in which each SR junction needs independent noise. There are two possible sources of the noise; internal noise which come from the intrinsic properties of the device's materi-

als and external noise which come from additional external equipment. In previous studies, independent noise was applied from external equipment to each SR unit caused bloating in those experimental systems and limited the number of SR units.

Spontaneous noise generation at each multiple junction will free the system from a large number of external noise generators. Single-walled carbon nanotubes (SWNTs)[25] are widely used in the development electronic devices owing to their extraordinary electrical properties and high controllability. It is considered that SWNTs have the potential to fulfill the three fundamental requirements for realizing SR electronic devices, viz., multiple junction structure, nonlinear response with threshold, and spontaneous independent noise for each junction. A multiple junction structure of SWNTs can be easily obtained by various deposition techniques.[26,27] A nonlinear response can be obtained from FET transfer characteristics or nonlinear current-voltage characteristics through appropriate device fabrication. Furthermore, SWNTs can be generators of spontaneous noise owing to their high sensitivity to external surface perturbation resulting from their quasi-one-dimensional structure having high surface-to-volume ratio. It is found that the introduction of an extra disruptor to the SWNT conductance, i.e., molecular adsorption, generated a large and tunable type of electrical noise in addition to common environmental noise.[28,29] Each SWNT junction will have different noise characteristics owing to the randomness of molecular adsorption and its fluctuation. SWNTs offer a promising route to realizing a small-size summing network SR device that utilizes molecular thermal fluctuation as a noise source.

In this chapter, an SR device based on a parallel network of SWNTs were fabricated, which had an independent self-noise source, to detect weak signals below the threshold of the conducting regime. The present SWNT device with Cr electrodes exhibited highly reproducible nonlinear current-voltage (I-V) characteristics with a threshold voltage (V_{th}) under ambient conditions. Molecular functionaliza-

tion generated large random electrical noise in the current through SWNT channels. Enhancement in weak signal detection were observed in a parallel summing network SWNT-based SR device with molecular functionalization. The enhancement in the correlation coefficient between the input and output signals was achieved as a result of the molecular noise. The efficiency of the signal detection, which depended on the number of adsorbed molecules and might be proportional to the noise intensity, was investigated.

6.2   Experimental[30]

SWNT devices were fabricated on a Si substrate with a 300-nm-thick SiO_2 layer. Electrodes were patterned using electron beam lithography. A 50-nm-thick Cr layer was deposited onto the substrate by electron beam deposition. The channel lengths was 1 μm, while the channel width was 20 μm. The substrates were cleaned by using a piranha solution and modified by using 1% 3-aminopropyltriethoxysilane (APTES, Sigma-Aldrich) in toluene for 1 h under N_2 conditions. 99% semiconducting SWNTs (NanoIntegris, Inc.) having an average diameter of 1.4 nm and an average length of 1 μm were dispersed in N,N-dimethylformamide (DMF, Sigma Aldrich) with a concentration of 500 ng/ml. A semiconducting SWNT parallel network was deposited using the AC-dielectrophoresis method.[26] To align the SWNTs between electrodes, an AC voltage of 8 V_{p-p} at 1 MHz was applied for 15-20 s. The device was blown dry, rinsed with isopropyl alcohol (Sigma Aldrich), and then blown dry again. After SWNT deposition, the substrate was annealed at 150°C inside a vacuum oven for 1 h to remove residual solvent. An atomic force microscopy (AFM, SPA 400, DFM mode, SII Inc.) image of a typical SWNT parallel network is shown in Fig. 6.1(a). On the basis of the present AFM images, the number of SWNT junctions of the device in this experiment can be roughly estimated to be between 100 and 300.
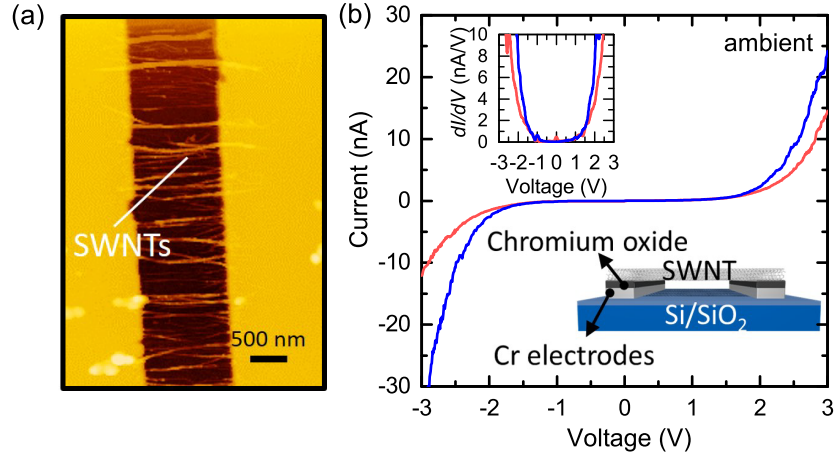
Figure 6.1: AFM image (a) and I-V characteristics (b) of a multiple-SWNT device fabricated on Cr electrodes. Inset in (b) is the dI/dV vs voltage curve, showing a clear threshold voltage and the side view of the schematic of the device. Blue and red lines are the I-V characteristic of multiple-SWNT device before and after adsorption of PMo_{12}, respectively. This image was taken from Ref. [30].

I-V measurements on the SWNT device were performed using a Keithley 4200-SCS semiconductor parameter analyzer. All measurements in this study were carried out at room temperature under atmospheric pressure. The blue solid line in Fig. 6.1(b) shows the typical nonlinear I-V characteristics with threshold, obtained by measuring a multiple SWNT device using Cr electrodes. The dI/dV versus voltage curve was steep at the threshold voltage, V_{th}, as seen in the inset of Fig. 6.1(b). The red line represents the I-V characteristic after molecular adsorption, which will be explained later. It is confirmed that piranha solution cleaning forms a thin Cr oxide layer on the Cr electrodes and thus provide nonlinear I-V characteristic, while linear I-V characteristics were obtained for devices without piranha cleaning. The cause of the steep nonlinearity with threshold must be the tunneling current at the interface between Cr and SWNT. The V_{th} value for our multiple-SWNT devices fabricated on Cr electrodes, 1.24±0.06 V, showed high reproducibility. In the present study, V_{th} was defined as the voltage that reached 0.5 nA/V in the dI/dV curve.

SWNTs were functionalized with phosphomolybdic acid ($H_3PMo_{12}O_{40}$) (hereafter PMo_{12}) molecules, which can firmly adsorb on graphite materials,[31,32] using a simple

drop casting method. The structure of PMo_{12} molecule is shown in Fig. 6.2(a). 20 μl of PMo_{12} (Sigma Aldrich), dissolved in DMF to a concentration of 1 mg/ml, was dropped between the electrodes. The amount of deposited molecules was roughly controlled by repeating the drop casting process. Each device was then dried on a hotplate at 150°C under atmospheric pressure. No significant change was observed in I-V characteristic after molecular functionalization, as shown in Fig. 6.1(b). The V_{th} value after molecular adsorption was 1.34±0.26 V. The current above V_{th} generally decreases after molecular adsorption. The I-V measurement voltage were limited within ±3 V in the case of multiple-SWNT devices with Cr electrodes to prevent damage because these devices are much more fragile during electrical measurements than SWNT devices with Au electrodes.

6.3   Results and discussion

It has been reported that the adsorption of molecules onto the CNT surface increases the noise of CNT devices.[28,29] Previous study demonstrated that the marked noise generation in SWNT device current, due to charge trapping and detrapping event on the SWNT surface by the adsorbed molecules, exhibits unique properties related to the noise frequency, depending on the molecular redox activity.[29] Among the examined molecules, PMo_{12} was the most active in terms of the generation of noise in SWNT device current. Figure 6.2(b) shows the DC current noise obtained with and without molecular adsorption in multiple-SWNT devices incorporating Au electrodes, which are fabricated through the same process as the one incorporating Cr electrodes. The DC voltage was applied by using a battery, and the current was amplified using a current amplifier (LI-76, NF Corporation). In order to measure the current noise, high DC voltage, > 5 V, must be applied to the SWNT device fabricated on Cr electrodes so that the current is measurable by the equipment. Long exposure to such high bias voltage will burn the SWNT junctions or

break the tunneling junctions and thus broke the device. Hence, the SWNT device were fabricated on Au electrodes which has linear I-V characteristic, and thus need lower DC voltage, ≤ 1 V, during current noise measurement. Figure 6.2(c) and 6.2(d) show the power spectral density (PSD) of the current noise before and after adsorption of PMo_{12} molecules, respectively. Clearly, the current noise increased dramatically upon molecular adsorption. Lorentzian-shaped PSD which were shown in Fig. 6.2(d) is a signature of the presence of generation-recombination (GR) noise which come from charge trapping-detrapping events. In this case, the origin of GR noise is charge trapping-detrapping event from/to the adsorbed molecules. The spectral density as a function of frequency, $S(f)$, of GR noise is represented by $S(f) = \sum_i B_i/(1 + (f/f_{c_i})^2)$, where B_i and f_{c_i} are the amplitude and corner frequency of the i-component of GR noise, respectively, and thus accumulation of the multiple GR event having identical f_c will increase the noise magnitude. Hence, the noise magnitude of our SWNT device can be increased by increasing the number of the adsorbed molecules. The number of the adsorbed molecules can also be increased by increasing the number of SWNT junctions. It is found that the cause of the noise is the fluctuation of SWNT conductance governed by the physical and chemical fluctuation of the external disrupter in or around the SWNT. It has been established that the fluctuation dynamics of the charge associated with adsorbed PMo_{12} leads to noisy fluctuation in the current through a SWNT in the device. Thus, it is believed that the noise increase induced by PMo_{12} adsorbed on SWNTs on Cr electrodes is comparable to that induced on SWNTs on Au electrodes.

SR measurement were performed on multiple-SWNT devices with Cr electrodes, as shown in Fig. 6.3(a). A voltage pulse train was applied to an electrode as an input signal with an offset voltage, V_{offset}, by using a function generator (NF wave factory WF 1945). The output current at the opposite electrode was amplified by a current amplifier (Keithley 428) and recorded using a digital oscilloscope (LeCroy Waverunner LT344). Figure 6.3(b) shows the typical input and output signal waveforms for
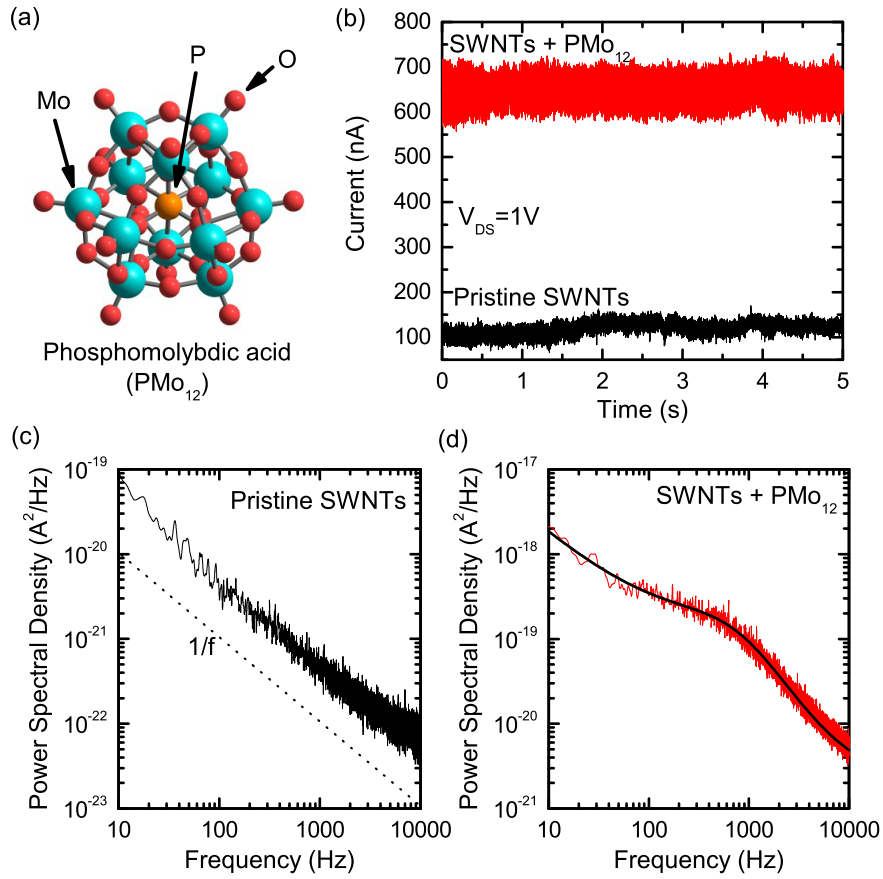
Figure 6.2: (a) Molecular structure of phosphomolybdic acid (PMo_{12}). (b) DC current noise of a multiple-SWNT device with Au electrodes before and after adsorption of PMo_{12}. (c) and (d) are the power spectral density (PSD) of DC current noise in (b). Black dotted-line in (c) is a typical $1/f$ characteristic of DC current noise. Solid black line in (d) is a fitting of PSD showing Lorentzian-shaped PSD. This image was taken from Ref. [30].
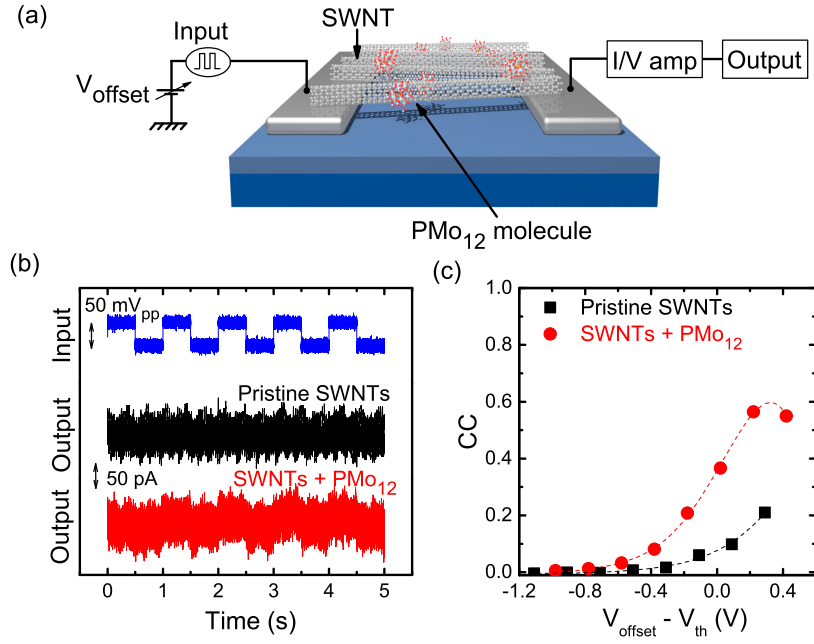
Figure 6.3: (a) Schematic of the multiple-SWNT device with PMo_{12} molecules and measurement configuration. (b) Typical input and output signal waveforms before and after PMo_{12} adsorption at a V_{offset}-V_{th} of -50 mV. (c) Correlation coefficient (CC) of the input-output signal of a multiple-SWNT device before and after PMo_{12} adsorption at various V_{offset}-V_{th}. This image was taken from Ref. [30].

a device measured before and after PMo_{12} adsorption, where the modulation amplitude (V_{pp}), frequency, and V_{offset} - V_{th} of the input signal were 50 mV, 1 Hz, and -50 mV, respectively. V_{offset} is the center of the input signal modulation. The most important SR measurement criterion was that the head of the input signal never exceed V_{th}. A pulse train pattern that is similar to the input signal and thus difficult to identify in the measured output signal for a pristine multiple-SWNT device can be seen in the measured output signal for the multiple-SWNT+PMo_{12} device.

The mutual signal correlation between the input and output signal waveforms were evaluated using the correlation coefficient (CC) defined by

$$CC = \frac{\langle S_{in}S_{out}\rangle - \langle S_{in}\rangle\langle S_{out}\rangle}{\sqrt{\left(\langle S_{in}^2\rangle - \langle S_{in}\rangle^2\right)\left(\langle S_{out}^2\rangle - \langle S_{out}\rangle^2\right)}} \tag{6.1}$$

where S_{in} and S_{out} are the input and output signal, respectively. A higher CC

indicates a higher similarity between S_{in} and S_{out}. In Fig. 6.3(b), the CC values of the pristine multiple-SWNT device and the multiple-SWNT+PMo$_{12}$ device were 0.06 and 0.30, respectively. In all other devices, the pristine multiple-SWNT device showed a lower response than the multiple-SWNT+PMo$_{12}$ device in their S_{out} vs. S_{in} curves. CC clearly depends on the difference between the V_{offset} of the input signal and the V_{th} of the I-V characteristics. Figure 6.3(c) plots the input-output CC data measured by changing V_{offset} as a function of V_{offset} - V_{th} for a multiple-SWNT device before and after PMo$_{12}$ adsorption. CC gradually increased by tracing a parabola-like curve as V_{offset} - V_{th} increased, where all CC values for multiple-SWNTs+PMo$_{12}$ were larger than that of pristine SWNTs over the entire voltage range. Above V_{th}, V_{offset} - V_{th} was greater than 0 V, and CC tended to saturate. Similar trends have been observed for all devices investigated in the present study.

Generally, the noise magnitude dependence of the mutual signal correlation is used to demonstrate SR phenomena. The internal noise of pristine multiple-SWNT device which come from the intrinsic properties of the SWNT is shown in Fig. 6.2(b). The average noise intensity of pristine multiple-SWNTs device is 7.375 mV$_{rms}$, while addition of a single-drop of PMo$_{12}$ solution increase the noise intensity to 19.925 mV$_{rms}$ though it was measured on Au devices. SR measurement were performed on multiple-SWNT device with multiple drop-casting step of PMo$_{12}$ solution to investigate the effect of noise intensity of SR system using multiple-SWNTs junctions as shown in Fig. 6.4(a). It is assumed that the noise in multiple-SWNT device increase proportional to the number of the adsorbed molecules because the noise which come from the molecule have narrow bandwidth as shown in Fig. 6.2(d), and thus accumulation of those molecular noise will increase the total noise intensity. The x-axis of Fig. 6.4(a) was converted into the noise intensity according to the assumption that each subsequent drop-casting of PMo$_{12}$ solution increase the same noise intensity of 12.55 mV$_{rms}$. It is known that in a single SR unit, the mutual signal correlation shows a single maximum, remarkable in terms of its dependence on

99

the noise magnitude, as demonstrated elsewhere.[13–15] This means that an excessively high noise magnitude significantly degrades the mutual signal correlation. On the other hand, the multiple summing network SR system proposed by Collins, et al. provides a higher signal transmission efficiency, which has a weaker dependence on noise magnitude, depending on the number of SR units.[14] There is no pronounce peak in this experimental results as seen in Fig. 6.4(a). The experimental result were fitted to the model which was developed by Collins, et al. represented by the following equation[14]:

$$C_M = \sqrt{\frac{N}{N + \sigma^2 \left[\frac{1 - \left(3\sqrt{3}\epsilon B^2/D\right)^2 \langle S^2(t) \rangle}{\left(3\sqrt{3}\epsilon B^2/D\right)^2 \langle S^2(t) \rangle} \right] \exp\left(\frac{2\sqrt{2}\epsilon B^3}{D}\right)}} \qquad (6.2)$$

where N, D, σ, ϵ, B, and $S(t)$ are the number of SR units, noise intensity, empirical function of D, FitzHugh-Nagumo model parameter, signal-to-noise distance, and input signal, respectively. $S(t)$ is the input signal of SR measurement of 50 mV$_{pp}$, while D is the x-axis of Fig. 6.4(a). σ is a quadratic polynomial function of D as used in previous reports.[33] The N, ϵ, and B were varied to find the minimum error between experimental results and the fitted line. Figure 6.4(b) shows the error mapping of the data fitting. It is found that $N = 97$, $\epsilon = 0.004$, and $B = 2.5$ are the best fitting parameter. The fitting results is shown by the solid line in Fig. 6.4(a). Hence, it can be concluded that multiple-SWNTs+PMo$_{12}$ device has 97 SR units. Based on AFM image of multiple-SWNTs device which was shown in Fig. 6.1(a), it is likely that the device consist of more than 100 individual SWNT junctions aligned parallel to each other and prevent the correlation between SWNT junctions, which is expected to provide SR effect for more than 100 SR units. However, fitting results suggest that this SR system consist of less than 100 units. It is considered that some of the SWNTs junctions might be connected to each other and thus decrease the number of SR units.
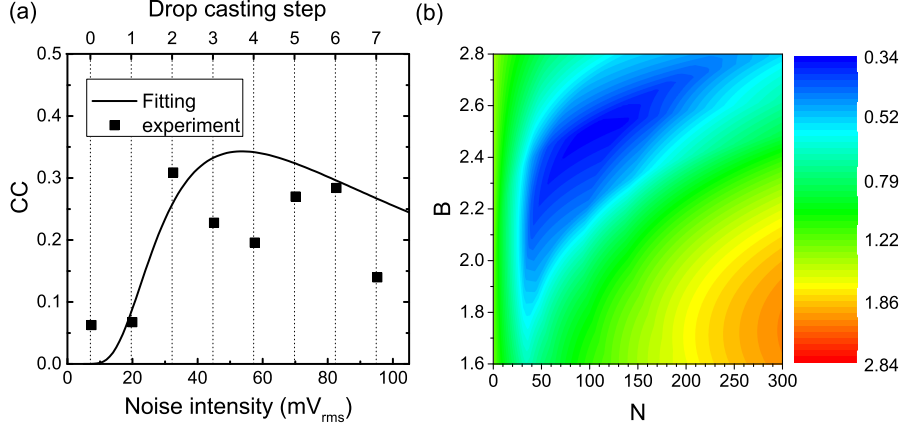
Figure 6.4: (a) CC at various drop casting step of molecular solution at V_{offset}-V_{th} of 50 mV. The x-axis was converted into noise intensity. The detail of the conversion is explained in the main text. The solid line is the data fitting with eq. 6.2. The V_{offset}-V_{th} of the experimental data is -50 mV. (b) Error mapping of the data fitting with eq. 6.2. The best fitting parameter are found to be $N = 97$, $\epsilon = 0.004$, and $B = 2.5$. This image was taken from Ref. [30].

The CC which were shown in Fig. 6.4(a) can also be regarded as having double maximum points. According to the previous study, the presence of double maximum is come from the interaction between two noise sources, internal and external noise.[34] It has been shown previously that internal noise also play an important role to provide constructive enhancement of SR effect.[6,35,36] In our case, there is no applied external noise but there are two internal noise sources coming from intrinsic SWNT noise and molecular noise with different characteristic. There is a possibility that the intrinsic noise of SWNT can be modulated by the molecular noise leading to the appearance of double maximum in CC curve. However, the specific interaction between those two internal noise is unknown. In addition, the results from another device shows double maximum at different position and magnitude. Therefore, it is difficult to make detail elucidation of the double maximum in CC curve.

In this experiments, the magnitude of CC depends directly on the magnitude of the input signal, V_{pp}, whereas the real mutual signal correlation, CC, as defined by eq. (1), never depends on the signal magnitude, but rather, only on the cor-

respondence between their shapes. The CC obtained from multiple-SWNT device with adsorbed molecules was not so high, because of low input signal amplitude, V_{pp}, of 50 mV. The aimed is to develop a device to detect small signal modulations below the thermal energy at room temperature, about 25 meV, utilizing spontaneous molecular fluctuations at room temperature. However, while multiple-SWNT device could detect signal modulations in the supra-threshold region, it could not detect signal modulations at a V_{pp} of 25 mV. Various improvements, such as precise control of noise generation and a steep threshold, are necessary to enable it to detect smaller signal modulations. Fundamentally, however, signal detection systems utilizing spontaneous fluctuations in multiple network systems promise to lead to various new applications.

6.4   Conclusion

In conclusion, the summing network SR effect was investigated using a multiple-SWNT device with a molecular self-noise source. Multiple-SWNT+PMo_{12} device with Cr electrodes satisfies three requirements that are necessary to develop a multiple SR device: a nonlinear response with threshold, independent noise, and a multiple junction structure. The mutual signal correlation was found to increase in the multiple-SWNT+PMo_{12} device relative to the pristine SWNT device. It has been demonstrated that a small size summing network device consisting of only dense nanomaterials actively utilizing intrinsic spontaneous noise at room temperature can detect a small subthreshold signal through the multiple SR effect.

References

1. Douglass, J., Wilkens, L., Pantazelou, E. & Moss, F. Noise enhancement of information transfer in crayfish mechanoreceptors by stochastic resonance. *Nature* **365,** 337–340 (1993).

2. Russell, D. F., Wilkens, L. A. & Moss, F. Use of behavioural stochastic resonance by paddle fish for feeding. *Nature* **402,** 291–294 (1999).

3. Greenwood, P., Ward, L., Russell, D., Neiman, A. & Moss, F. Stochastic resonance enhances the electrosensory information available to paddlefish for prey capture. *Phys. Rev. Lett.* **84,** 4773–4776 (2000).

4. Bahar, S. & Moss, F. Stochastic resonance and synchronization in the crayfish caudal photoreceptor. *Math. Biosci.* **188,** 81–97 (2004).

5. Spezia, S. *et al.* Evidence of stochastic resonance in the mating behavior of Nezara viridula (L.) *Eur. Phys. J. B* **65,** 453–458 (2008).

6. Manjarrez, E. *et al.* Internal stochastic resonance in the coherence between spinal and cortical neuronal ensembles in the cat. *Neuroscience Letters* **326,** 93–96 (2002).

7. Mantegna, R. N. & Spagnolo, B. Stochastic resonance in a tunnel diode in the presence of white or coloured noise. *Il Nuovo Cimento D* **17,** 873–881 (1995).

8. Mantegna, R. N., Spagnolo, B., Testa, L. & Trapanese, M. Stochastic resonance in magnetic systems described by Preisach hysteresis model. *J. Appl. Phys.* **97,** 10E519 (2005).

9. La Cognata, A., Valenti, D., Dubkov, A. A. & Spagnolo, B. Dynamics of two competing species in the presence of Lévy noise sources. *Phys. Rev. E* **82,** 011121 (2010).

10. Mori, T. & Kai, S. Noise-induced entrainment and stochastic resonance in human brain waves. *Phys. Rev. Lett.* **88,** 218101 (2002).

11. Kitajo, K., Nozaki, D., Ward, L. M. & Yamamoto, Y. Behavioral stochastic resonance within the human brain. *Phys. Rev. lett.* **90,** 218103 (2003).

12. Soma, R., Nozaki, D., Kwak, S. & Yamamoto, Y. 1/f noise outperforms white noise in sensitizing baroreflex function in the human brain. *Phys. Rev. Lett.* **91,** 078101 (2003).

13. McNamara, B. & Wiesenfeld, K. Theory of stochastic resonance. *Phys. Rev. A* **39,** 4854–4869 (1989).

14. Collins, J, Chow, C & Imhoff, T. Stochastic resonance without tuning. *Nature* **376,** 236–238 (1995).

15. Gammaitoni, L., Hänggi, P., Jung, P. & Marchesoni, F. Stochastic resonance. *Rev. Mod. Phys.* **70,** 223–287 (1998).

16. Nishiguchi, K. & Fujiwara, A. Detecting signals buried in noise via nanowire transistors using stochastic resonance. *Appl. Phys. Lett.* **101,** 193108 (2012).

17. Samardak, A. *et al.* Noise-controlled signal transmission in a multithread semiconductor neuron. *Phys. Rev. Lett.* **102,** 226802 (2009).

18. Kasai, S. & Asai, T. Stochastic Resonance in Schottky Wrap Gate-controlled GaAs Nanowire Field-Effect Transistors and Their Networks. *Appl. Phys. Express* **1,** 083001 (2008).

19. Kasai, S., Miura, K. & Shiratori, Y. Threshold-variation-enhanced adaptability of response in a nanowire field-effect transistor network. *Appl. Phys. Lett.* **96,** 194102 (2010).

20. Lee, I., Liu, X., Kosko, B. & Zhou, C. Nanosignal processing: Stochastic resonance in carbon nanotubes that detect subthreshold signals. *Nano Lett.* **3,** 1683–1686 (2003).

21. Hakamata, Y. *et al.* Enhancement of weak-signal response based on stochastic resonance in carbon nanotube field-effect transistors. *J. Appl. Phys.* **108,** 104313 (2010).

22. Hakamata, Y., Ohno, Y., Maehashi, K., Inoue, K. & Matsumoto, K. Robust noise characteristics in carbon nanotube transistors based on stochastic resonance and their summing networks. *Jpn. J. Appl. Phys.* **50,** 06GE03 (2011).

23. Hirano, Y., Segawa, Y., Kawai, T. & Matsumoto, T. Stochastic resonance in a molecular redox circuit. *J. Phys. Chem. C* **117,** 140–145 (2013).

24. Kanki, T., Hotta, Y., Asakawa, N., Kawai, T. & Tanaka, H. Noise-driven signal transmission using nonlinearity of VO2 thin films. *Appl. Phys. Lett.* **96,** 242108 (2010).

25. Iijima, S. & Ichihashi, T. Single-shell carbon nanotubes of 1-nm diameter. *Nature* **363,** 603–605 (1993).

26. Shekhar, S., Stokes, P. & Khondaker, S. Ultrahigh density alignment of carbon nanotube arrays by dielectrophoresis. *ACS Nano* **5,** 1739–1746 (2011).

27. Setiadi, A., Akai-Kasaya, M., Saito, A. & Kuwahara, Y. Advantages of flattened electrode in bottom contact single-walled carbon nanotube field-effect transistor. *Appl. Phys. Lett.* **105,** 093506 (2014).

28. Sharf, T., Kevek, J. W., Deborde, T., Wardini, J. L. & Minot, E. D. Origins of charge noise in carbon nanotube field-effect transistor biosensors. *Nano lett.* **12,** 6380–6384 (2012).

29. Setiadi, A. *et al.* Room-temperature discrete-charge-fluctuation dynamics of a single molecule adsorbed on a carbon nanotube. *Nanoscale* **9,** 10674–10683 (2017).

30. Fujii, H., Setiadi, A., Kuwahara, Y. & Akai-Kasaya, M. *Single walled carbon nanotube-based stochastic resonance device with molecular self-noise source* submitted to Appl. Phys. Lett.

31. Song, Y.-F. & Tsunashima, R. Recent advances on polyoxometalate-based molecular and composite materials. *Chem. Soc. Rev.* **41,** 7384–7402 (2012).

32. Hong, L., Tanaka, H. & Ogawa, T. Rectification direction inversion in a phosphododecamolybdic acid/single-walled carbon nanotube junction. *J. Mater. Chem. C* **1,** 1137–1143 (2013).

33. Collins, J. J., Chow, C. C. & Imhoff, T. T. Aperiodic stochastic resonance in excitable systems. *Phys. Rev. E* **52,** R3321–R3324 (1995).

34. Gailey, P. C., Neiman, A., Collins, J. J. & Moss, F. Stochastic Resonance in Ensembles of Nondynamical Elements: The Role of Internal Noise. *Phys. Rev. Lett.* **79,** 4701–4704 (1997).

35. Wang, W. & Wang, Z. D. Internal-noise-enhanced signal transduction in neuronal systems. *Phys. Rev. E* **55,** 7379–7384 (1997).

36. Ishimura, K., Schmid, A., Asai, T. & Motomura, M. Stochastic resonance induced by internal noise in a unidirectional network of excitable FitzHugh-Nagumo neurons. *NOLTA* **7,** 164–175 (2016).

Chapter 7

Summary and Future Outlook

7.1 Summary

The work in this dissertation show an experimental approach towards the elucidation and utilization of current noise in carbon nanotube (CNT) device. The study covers investigation of the basic characteristic of pristine CNT as electronic device, elucidation of the current noise of CNT device in the presence of adsorbed molecule, and utilization of the current noise in CNT device to develop stochastic resonance (SR) device with self noise source.

Chapter 3 and 4 describe the investigation of basic properties of CNT in the electronic device. It was found that bending of CNT at the interface with the metal electrodes mainly govern the transport properties of the CNT in bottom contact CNT field-effect-transistor (FET) devices. Bending of the CNT due to the height difference between metal electrodes and insulating substrates alter the electronic properties only at the interface. Comparison of two type of CNT, with and without bending, were made by fabricating CNT device on non-flattened and flattened bottom-contact electrodes. The change of the electronic properties of the CNT

106

were shown by the FET characteristic which show p-type dominant and ambipolar characteristic in the presence and absence of the CNT bending at the interface, respectively. Raman mapping investigation show that bending of the CNT downshifted the position of G^+ and G^- band position of the CNT. Both results, FET characteristic and Raman spectroscopy, suggest that bending of the CNT shifted the Fermi level of the CNT towards the valence band and thus change the Schottky barrier for both hole and electron.

Chapter 5 describes the elucidation of current fluctuation in CNT device that additionally generated by the molecular adsorption. It is concluded that each molecules in this research provides unique current fluctuation in the form of random telegraph signal (RTS) and Lorentzian-shaped power spectral density (PSD) in time- and frequency-domain signal, respectively. There are two important information that can be extracted from the results; first, the corner frequency of Lorentzian-shaped PSD is inversely proportional to the barrier energy and the adsorbed molecules, which indirectly describes the electronic coupling strength between CNT and the adsorbed molecules, second, the ratio of the lifetime of RTS contains information on the most active molecular orbital of the adsorbed molecule with respect to the Fermi level of CNT. This new knowledge can lead to the development of various novel devices, for example, ultra sensitive sensing device at single molecular limit.

Chapter 6 presents the development of SR device based on multiple-CNT junctions with self-noise source. It was found that the amplitude of the current fluctuation increased in proportion to the number of adsorbed molecules because the fluctuation induced by the molecule have narrow bandwidth, and thus accumulation of those molecular fluctuation increases the total fluctuation in the CNT device. Based on this results, a new type of SR device has been fabricated. Previous development of SR devices always utilize external equipment as noise generator which need high power consumption, and thus obstruct further development towards practical appli-

cation. This newly-developed SR device utilize current fluctuation by the adsorbed molecules as self-noise source, and thus provides significant advance in the development of SR device.

The results which were presented in chapter 5 and 6 also lead to a better understanding of the current fluctuation that provide a new paradigm whereby the presence of fluctuation can be advantageous in electronics. Moreover, these results also offer a new insight to pave the road toward the development of future information processing device beyond CMOS technology.

7.2 Future outlook: Development of pulse generator device for neuromorphic device

Neuromorphic device is a device which mimics human brain.[1] Human brain is a sophisticated system that can handle complicated task with lower power consumption than conventional computer. Hence, many effort were done to fabricate neuromorphic device. There are two main building blocks of neuromorphic device: neuron-like and synapse-like devices, that is, minimum set of neuromorphic device consist of two neurons and one synaptic gap. A synaptic gap connects one neuron to the neighboring one, which govern coupling strength between those two neurons. An information can be transmitted between the neurons via synaptic gap in the form of nerve impulse signal as shown in Fig. 7.1. Synapse-like device has been widely explored and mainly based on memristor device, in which the resistance of a memristor can be adjusted in analog way.[2] Conventional transistors and capacitors can be configured to generate nerve impulse-like signal. However, they will face the scaling limitation due to complicated structure and high power consumption.[3] CNTs are a good candidate for the development of neuron-like devices, as it has been shown in chapter 5 and 6 that molecular adsorption onto the CNT provides additional current fluc-
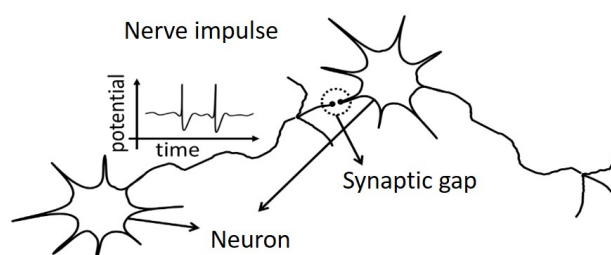
Figure 7.1: Two neurons are connected each other via synaptic gap. The inset is nerve impulse signal.

tuation of the CNT device. One of the best candidate for the adsorbed molecule is phosphomolybdic acid (PMo_{12}), which is polyoxometalates (POMs) derivatives exhibiting reversible multi-electron redox properties.[4]

Preliminary results

The pulse generator device based-on CNTs were fabricated on heavily doped silicon substrates with a 300-nm-thick SiO_2 layer using bottom contact electrodes. The CNTs were deposited using AC-dielectrophoresis[5] method to achieve multiple CNT junctions. Molecular adsorption were done by soaking the the device inside molecular solution of PMo_{12} with the concentration of 1 mg/ml for 1 hour. Pulse measurement were performed using digital oscilloscope at constant drain voltage. The schematic of the measurement configuration of the pulse generator device is shown in Fig. 7.2(a). Measurement results are shown in Fig. 7.2(b).

It is clear that the CNT+PMo_{12} devices show a kind of pulse-like signal. However, evaluation method of the pulse-like signalhas not been defined yet. Hence, it is still difficult to confirm the reproducibility of the data even though, so far, the pulse-like signal were observed several times on different devices. Moreover, the underlying physical mechanism of this phenomena is still debatable. Nevertheless, this preliminary result shows the potential of CNT+PMo_{12} hybrid device as pulse generator for the development of neuromorphic device. It is also considered that
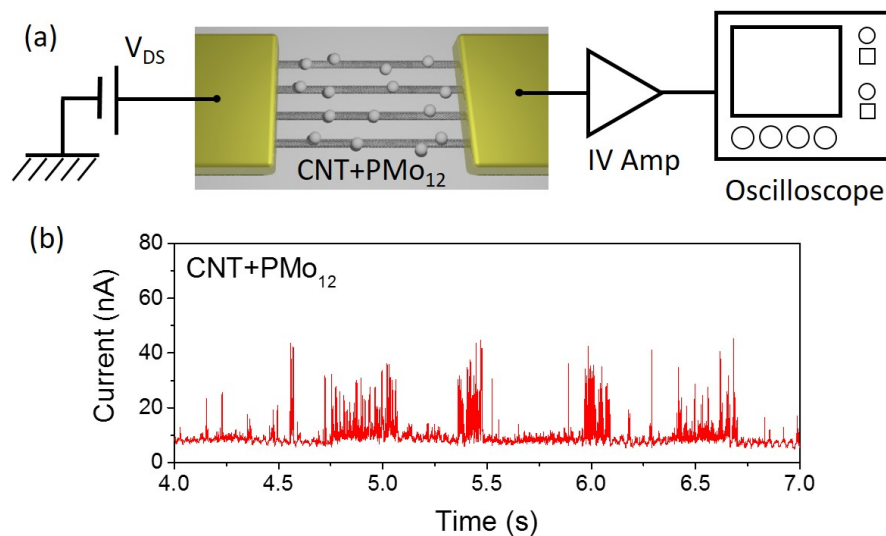
Figure 7.2: (a) Measurement configuration for pulse generator device including the schematic of the device. (b) The results of pulse measurement.

other POMs molecule may posses similar potential to that of PMo_{12}.

References

1. Mead, C. *Analog VLSI and neural systems* (Adison-Wesley, Massachusetts, USA, 1989).

2. Jo, S. H. *et al.* Nanoscale memristor device as synapse in neuromorphic systems. *Nano Lett.* **10,** 1297–1301 (2010).

3. Morie, T., Matsuura, T., Nagata, M. & Iwata, A. A multinanodot floating-gate MOSFET circuit for spiking neuron models. *IEEE Trans. Nanotechnol.* **2,** 158–164 (2003).

4. Hong, L., Tanaka, H. & Ogawa, T. Rectification direction inversion in a phosphododecamolybdic acid/single-walled carbon nanotube junction. *J. Mater. Chem. C* **1,** 1137–1143 (2013).

5. Shekhar, S., Stokes, P. & Khondaker, S. Ultrahigh density alignment of carbon nanotube arrays by dielectrophoresis. *ACS Nano* **5,** 1739–1746 (2011).

List of Publication

1. H. Fujii, **A. Setiadi**, Y. Kuwahara, M. Akai-Kasaya, Single walled carbon nanotube-based stochastic resonance device with molecular self-noise source, accepted for publication in *Appl. Phys. Lett.*

2. **A. Setiadi**, H. Fujii, S. Kasai, K. Yamashita, T. Ogawa, T. Ikuta, Y. Kanai, K. Matsumoto, Y. Kuwahara, M. Akai-Kasaya, Room-temperature discrete-charge-fluctuation dynamics of a single molecule adsorbed on a carbon nanotube, *Nanoscale* **9**, 10674-10683 (2017).

3. **A. Setiadi**, M. Akai-Kasaya, Y. Kuwahara, Raman mapping investigation of single-walled carbon nanotube bending in bottom-contact field-effect-transistor devices, *J. Appl. Phys.* **120**, 094302 (2016).

4. **A. Setiadi**, M. Akai-Kasaya, A. Saito, Y. Kuwahara, Advantages of flattened electrode in bottom contact single walled carbon nanotube field effect transistor, *Appl. Phys. Lett.* **105**, 093506 (2014).

5. S. Chaunchaiyakul, **A. Setiadi**, P. Krukowski, M. Akai-Kasaya, A. Saito, H. Osuga, Y. Kuwahara, Nanoscale dehydrogenation observed by tip-enhanced Raman spectroscopy, *J. Phys. Chem. C* (2017), doi:10.1021/acs.jpcc.7b03352.

List of Presentations

1. **A. Setiadi**, H. Fujii, Y. Kuwahara, M. Akai-Kasaya, Single walled carbon nanotube-based stochastic resonance device with molecular self-noise source (poster), Molecular Architectonics Workshop – Toward Realization of Neuromorphic Computing by Nanomaterials, Toyonaka, Japan, June 29-30, 2017.

2. **A. Setiadi**, H. Fujii, S. Kasai, K. Yamashita, T. Ogawa, T. Ikuta, Y. Kanai, K. Matsumoto, Y. Kuwahara, M. Akai-Kasaya, Room-temperature Discrete-charge-fluctuation Dynamics of a Single Molecule Adsorbed on a Carbon Nanotube (poster), Molecular Architectonics Workshop – Toward Realization of Neuromorphic Computing by Nanomaterials, Toyonaka, Japan, June 29-30, 2017.

3. **A. Setiadi**, H. Fujii, M. Akai-Kasaya, S. Kasai, K. Yamashita, T. Ogawa, T. Ikuta, Y. Kanai, K. Matsumoto, Y. Kuwahara, Random telegraph signal in molecule-functionalized carbon nanotube electronic devices (poster), 9th International Conference on Molecular Electronics and Bioelectronics, Kanazawa, Japan, June 26-28, 2017.

4. **A. Setiadi**, H. Fujii, M. Akai-Kasaya, Y. Kuwahara, Molecule-functionalized carbon nanotube for the development of novel electronic devices (oral), Kansai Thin Film and Surface Physics Seminar 2016, Kobe, Japan, November 18, 2016.

5. **A. Setiadi**, H. Fujii, M. Akai-Kasaya, S. Kasai, K. Yamashita, T. Ogawa, Y. Kanai, K. Matsumoto, Y. Kuwahara, Room-temperature discrete-charge-fluctuation dynamics of a single molecule adsorbed on a carbon nanotube (poster), The 7th Molecular Architectonics Meeting, Fukuoka, Japan, October 20-21, 2016.

6. **A. Setiadi**, H. Fujii, M. Akai-Kasaya, S. Kasai, Y. Kanai, K. Matsumoto, Y. Kuwahara, Molecular characterization using current noise measurement of carbon nanotubes device (oral), The International Chemical Congress of Pacific Basin Societies 2015, Honolulu, USA, December 15-20, 2015.

7. **A. Setiadi**, H. Fujii, M. Akai-Kasaya, S. Kasai, Y. Kanai, K. Matsumoto, Y. Kuwahara, Molecular characterization using current noise measurement of carbon nanotubes device at room temperature (poster), International Workshop on Molecular Architectonics, Shiretoko, Japan, August 3-6, 2015.

8. **A. Setiadi**, H. Fujii, M. Akai-Kasaya, A. Saito, Y. Kuwahara, Molecular characterization using current noise measurement of carbon nanotubes device (poster), The 5th Molecular Architectonics Meeting, Chiba, Japan, April 23-24, 2015.

9. **A. Setiadi**, M. Akai-Kasaya, A. Saito, Y. Kuwahara, Advantages of flattened electrode in bottom contact SWNT field effect transistor (poster), Molecular and Material Synthesizes Platform Symposium, Nagoya, Japan, March 5-6, 2015.

10. **A. Setiadi**, M. Akai-Kasaya, A. Saito, Y. Kuwahara, Advantages of flattened electrode in bottom contact SWNT field effect transistor (poster), the 2nd International Symposium on the Functionality of Organized Nanostructures 2014, Tokyo, Japan, November 26-28, 2014.

11. **A. Setiadi**, H. Fujii, M. Akai-Kasaya, A. Saito, Y. Kuwahara, Carbon nanotube-

based stochastic resonance device with self-noise source (poster), The 4th Molecular Architectonics Meeting, Toyonaka, Japan, November 24-26, 2014.

12. **A. Setiadi**, M. Akai-Kasaya, A. Saito, Y. Kuwahara, Advantages of flattened electrode in SWNT-based stochastic resonance device (oral and poster), The 3rd Molecular Architectonics Meeting, Tendo, Japan, June 12-14, 2014.

13. **A. Setiadi**, M. Akai-Kasaya, A. Saito, Y. Kuwahara, Bottom contact ambipolar SWNT-FET devices using flattened electrodes (oral), JSPE Spring Meeting 2014, Tokyo, Japan, March 18-20, 2014.

14. **A. Setiadi**, M. Akai-Kasaya, A. Saito, Y. Kuwahara, Advantages of flattened electrode in bottom contact single walled carbon nanotube field effect transistor (oral), The 61st JSAP Spring Meeting, Sagamihara, Japan, March 17-20, 2014.

15. **A. Setiadi**, M. Akai-Kasaya, A. Saito, Y. Kuwahara, Thin film single walled carbon nanotube transistor for stochastic resonance device (poster), 12th International Conference on Atomically Controlled Surfaces, Interfaces and Nanostructures (ACSIN-12) & 21st International Colloquium on Scanning Probe Microscopy (ICSPM21), Tsukuba, Japan, November 4-8, 2013.

16. **A. Setiadi**, T. Nakanishi, M. Akai-Kasaya, A. Saito, Y. Kuwahara, Multiple carbon nanotubes junctions for stochastic resonance devices (poster), International vacuum congress 19 (IVC-19) - International Conference on Nanoscience and Technology 2013 (ICNT 2013), Paris, France, September 9-13, 2013.

Acknowledgements